Simulations of Star Formation in Ophiuchus

Oliver David Lomax

School of Physics and Astronomy

Cardiff University

A thesis submitted for the degree of

Doctor of Philosophy

August 2013

Declaration

This work has not been submitted in substance for any other degree or award at this or any other university or place of learning, nor is being submitted concurrently in candidature for any degree or other award.

Signed ..... Date .....

Statement 1

This thesis is being submitted in partial fulfillment of the requirements for the degree of PhD.

Signed ..... Date .....

Statement 2

This thesis is the result of my own independent work/investigation, except where otherwise stated. Other sources are acknowledged by explicit references. The views expressed are my own.

Signed ..... Date .....

Statement 3

I hereby give consent for my thesis, if accepted, to be available for photocopying and for inter-library loan, and for the title and summary to be made available to outside organisations.

Signed ..... Date .....

Acknowledgements

Well, here we are. Three and a half years of my life and this to show for it. This is my small contribution to the ever expanding sphere that is the sum total of human knowledge. Of course, there are many I must thank for getting me here.

First and foremost I would like to thank my supervisor Professor Anthony Whitworth. As a mentor and role model, he has guided me through these formative years of my academic life. I'd like to think that I inspired him to grow a beard. Secondly, I'd like to thank my two examiners: Dr Nicholas Peretto and Dr Simon Goodwin. I have little doubt that their feedback on this thesis has made me a better (if less emotionally stable) scientist.

Kudos also goes to my office colleagues, past and present: Scott Balfour, Katy Holman, Dr Dimitris Stamatellos, Dr Andrew McLeod, Dr Steffi Walch, Dr Annabel Cartwright and, last but not least, Dr David "The Numerical Muscle" Hubber.

I would be remiss not to also thank my long-suffering better half, Dr Carrie-anne Sharma. She has demonstrated the patience of a saint by putting up with my endless neuroses. Carrie-anne, I love you.

I would like to thank my family, without whom I wouldn't have made it this far. Cheers to Mum, Sam, Mike, Ed, Will and my late grandparents, Roy, Vera, Stan and Kay.

Finally, I would like to thank my fiends: Sam Rowe, Sara Carver, Ciara Quinn, George Ford, Matt Smith, Chris Clarke, Ezzie Pearson, Chris Fuller, Ian Harrison, Laura Nuttall, Duncan MacLeod, Andrew Williamson, Thomas Adams, Russell Milton Sensei, Peter Gillard Sensei, Adrian Jenkins, Ian Breen, Karen Child (and Nugget) Kris Jenkins, Brian Court, Julian Stewart and Chris Duffy (please forgive me, I've almost certainly forgotten to list a few of you). It's been emotional.

Abstract

The way in which stars form from the interstellar medium is poorly understood. In this thesis we investiage the process star formation in molecular clouds via core fragmentation using Smoothed Particle Hydrodynamics (SPH). The initial conditions of the simulations are informed as closely as possible by observations of Ophiuchus. We run large ensebles of individual core simulations and compare the collective results with observations of stars and brown dwarfs.

We use observations of Ophiuchus by Motte et al. (1998) and André et al. (2007) to calibrate a lognormal distribution from which we draw correlated masses, sizes and velocity dispersions. We assume that the cores are intrinsically triaxial. The distribution of core shapes is then inferred by fitting a single parameter family of ellipsoidal shapes to the observed core aspect ratios. Each core is given the density profile of a critical Bonnor-Ebert sphere and a turbulent velocity field which is modified to include ordered rotation and radial excursions. We evolve one hundred of the model prestellar cores using the Seren SPH code (Hubber et al., 2011). The simulations are repeated with continuous accretion heating, no accretion heating and episodic accretion heating (Stamatellos et al., 2012).

We find that simulations with episodic accretion heating can reproduce the general features of the Chabrier (2005) initial mass function. This includs the ratio of stars to brown dwarfs and the turn-over at $0.2\,\mathrm{M}_\odot$. We demonstrate that the mass of a star is not related to the mass of the prestellar core in which it formed. Low mass cores with $M_{\rm CORE} \sim 0.1\,\mathrm{M}_\odot$ tend to collapse into single objects whereas higher mass cores with $M_{\rm CORE} \gtrsim 1\,\mathrm{M}_\odot$ can fragment into tens of objects. We finally show that the multiplicy statistics of the protostars formed in these simulations are well matched by observations. Multiplicity frequencies are higher than those of field stars and we note the presence of long-lived quadruple, quintuple and sextuple systems.

Contents

List of Figures

List of Tables

Chapter 1

Introduction

1.1 Star Formation

Stars are interesting. Without them, the Universe would not possess any heavy chemical elements or environments favourable to life. This alone makes their formation worthy of study. In addition to this, we cannot understand the evolution of galaxies without a robust model of star formation.

Observationally, the Main Sequence and post-Main Sequence phases of stellar evolution have been studied for over a century, however the study of star formation has only become practical in the last few decades. Infrared telescopes (e.g. Spitzer, IRAS) have been used to observe young stellar objects (YSOs). However, the molecular hydrogen from which stars form is difficult to detect as the molecules are not polar. Fortunately, the molecular gas is also mixed with dust and CO which can be detected. Submillimetre telescopes (e.g. Herschel, JCMT) are able to trace the continuum emission from dust and this is used to estimate the distribution of molecular gas.

Star formation is a dynamical process which acts over twenty orders of magnitude in density and ten orders of magnitude in length. The physics involved (for example hydrodynamics and self-gravity) is non-linear and can only be analytically solved for naïvely simple configurations of matter. Modelling the process of star formation therefore requires the use of numerical simulations performed on supercomputers.

The aim of this thesis is to perform numerical simulations of star formation in order to gain insights into the physics involved. The initial conditions of these simulations are informed as closely as possible by observations of star forming regions.

1.1.1 Molecular clouds

Molecular clouds (MCs) are large condensations of gas, usually found near the spiral arms of the Galaxy. They tend to have masses in the range $10^2\,\mathrm{M}_\odot \lesssim M \lesssim 10^6\,\mathrm{M}_\odot$ and diameters in the range $10^{-1}\,\mathrm{pc} \lesssim D \lesssim 10^2\,\mathrm{pc}$. They are optically thick to UV-dissociative photons which means that most of the gas is molecular, rather than atomic, hydrogen. The gas density typically varies between $10^{-22}\,\mathrm{g\,cm^{-3}} \lesssim \rho \lesssim 10^{-20}\,\mathrm{g\,cm^{-3}}$ with temperatures below 100 K. MCs with masses greater than $10^4\,\mathrm{M}_\odot$ are called *Giant Molecular Clouds* (GMCs).

The main constituent of an MC, molecular hydrogen, is a non-polar molecule which is almost invisible at typical MC temperatures. The column density of an MC therefore needs to be inferred by observing other visible tracers. Continuum emission from dust is often used as a tracer for column denisty (e.g. Motte et al., 1998; Simpson et al., 2008). Dust is optically thin at submillimetre wavelengths, so the flux density is proportional to the product of the column density and temperature. The temperatures can be estimated using radiative transfer models (e.g. Stamatellos et al., 2007b) or by fitting a spectral energy distribution (e.g. Kirk et al., 2013). Column densities can also be estimated from molecules such as carbon monoxide (e.g. Wilking and Lada, 1983). However, these are often optically thick and at high column densities the flux density is only proportional to the temperature.

The radial velocity dispersion of gas in an MC can be estimated from the width of emission lines such as N_2H^+ and HCO^+ (e.g. André et al., 2007). If temperature estimates are available, the velocity dispersion can be separated into its thermal and non-themal components. Velocity dispersions in MCs appear to be supersonic, with a velocity-size relation that roughly follows a Kolmogorov spectrum (e.g. Larson, 1981), suggesting the presence of turbulence. This turbulence is likely to have been generated by the uneven assembly of gas and feedback from neighbouring and embedded stars. Examples of feedback mechanisms include ionizing radiation, winds, and magneto-hydrodynamical waves (e.g. Ballesteros-Paredes et al., 2007). As a consequence of turbulence, the configuration of matter in MCs is not spherical. Instead, gas is distributed in clumps and filaments. Figure 1.1 shows an example of this in the Taurus molecular cloud.

Particularly dense, gravitationally bound and starless regions of MCs which have densities greater than $10^{-20}\,\mathrm{g\,cm^{-3}}$ are called prestellar cores (Andre et al., 2000). These are believed to be the main sites of star formation. It it thought that MCs are not quasi-static objects with long life-times. Instead, the clouds rapidly produce stars and then disperse over a few crossing times (Elmegreen, 2000). The remaining clusters of stars are usually super-virial and disperse to become field stars.

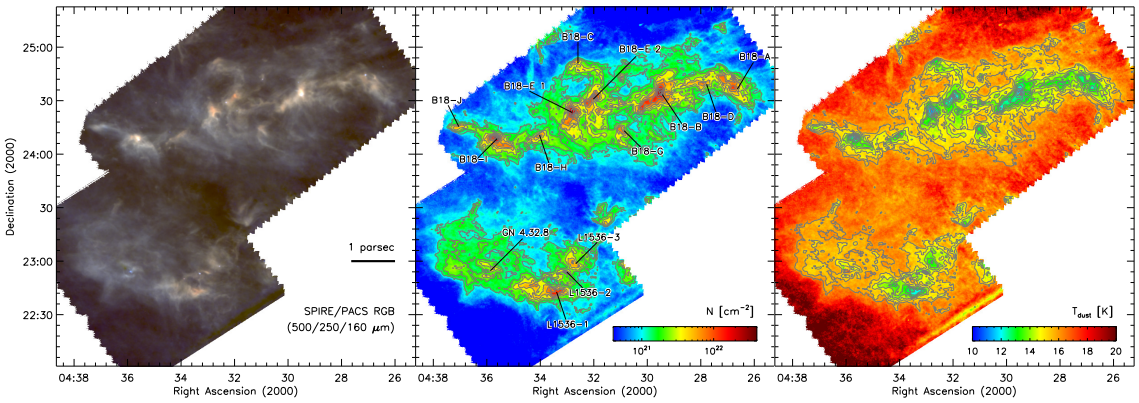

Figure 1.1: Herschel maps of the S1 and S2 regions of the Taurus molecular cloud observed using Herschel, taken from Kirk et al. (2013). The left panel shows a false colour image with red, green and blue showing 500 μm, 250 μm and 160 μm dust emission respectively. The middle panel shows the derived gas column density and the right panel shows the derived dust temperature.

Two well known GMCs are the Orion and Taurus molecular clouds. Orion is a high mass star forming region with a total mass of $10^5\,\mathrm{M}_\odot$ in a region of size $\sim 50\,\mathrm{pc}$. Here stars form in clusters, such as the Trapezium cluster. By contrast, Taurus is a low mass star forming region with total mass $10^4\,\mathrm{M}_\odot$ in a region of size $\sim 10\,\mathrm{pc}$. Here stars form in relatively isolated small N groups.

1.1.2 Prestellar cores

Prestellar cores (PCs) are dense, gravitationally bound clumps of gas within MCs (Andre et al., 2000). They have masses in the range $10^{-1}\,\mathrm{M}_\odot \lesssim M \lesssim 10\,\mathrm{M}_\odot$ and sizes in the range $10^{-2}\,\mathrm{pc} \lesssim D \lesssim 10^{-1}\,\mathrm{pc}$. As they are much more dense than the parent MC, they are shielded from external radiation and have temperatures around 10 K. Double peaked molecular emission lines with a stronger blue-shifted peak are often present as they are indicative of graviational infall (e.g. André et al., 2007; Simpson et al., 2011).

Prestellar cores are distinguished from unbound cores in molecular clouds by virtue of being Jeans unstable. The Jeans length is calculated by balancing the graviational potential energy of a core with twice its thermal energy (i.e. it is in virial equilibrium) and solving for the core radius. If we consider a non-rotating, spherical PC with mean density $\bar{\rho}$, temperature T and mean molecular mass $\bar{m}$, it

will collapse if its radius is smaller than the Jeans length[1]

$$R_{\rm JEANS} \approx 0.763 \frac{a_{\rm O}}{(G\bar{\rho})^{1/2}} \,, \tag{1.1}$$

where $a_{\rm O}$ is the isothermal sound speed

$$a_{\rm O} = \left(\frac{k_{\rm B} T}{\bar{m}} \right)^{1/2} \,. \tag{1.2}$$

It is often more useful to express this as the minimum mass required for gravitational collapse

$$M_{\rm JEANS} \approx 1.86 \frac{a_{\rm O}^3}{G^{3/2} \bar{\rho}^{1/2}} \,. \tag{1.3}$$

If we assume that a typical molecular core has $T = 10\,{\rm K}$ and $\bar{\rho} = 10^{-19}\,{\rm g\,cm^{-3}}$ (Motte et al., 1998; Simpson et al., 2008), it will be prestellar if it has a mass greater than $0.3\,{\rm M}_{\odot}$. Note that this assumes that the thermal energy of the core is significantly greater than its internal kinetic energy (e.g. turbulence and rotation).

During the initial stages of PC collapse, the gas is nearly isothermal with $T \approx 10\,{\rm K}$. This means that gravitational potential energy is quickly radiated away and the core will collapse in a few free fall times, $t_{\rm FF}$, where

$$t_{\rm FF} = \sqrt{\frac{3\pi}{32 G \bar{\rho}}} \,. \tag{1.4}$$

When the density increases above $10^{-13}\,{\rm g\,cm^{-3}}$, the gas starts to become optically thick (e.g. Larson, 1969; Masunaga and Inutsuka, 2000). This reduces the rate at which gravitational potential energy can be radiated away and the temperature increases. The consequent increase in thermal pressure causes the collapse to decelerate. Once the density reaches $10^{-12}\,{\rm g\,cm^{-3}}$, the gas is almost completely adiabatic and the core contracts quasi-statically. When the density reaches $10^{-8}\,{\rm g\,cm^{-3}}$, the temperature will have risen to $2000\,{\rm K}$. This is hot enough for molecular hydrogen to dissociate. The latent heat of dissociation allows the gas to become isothermal again and the core rapidly collapses to form a central protostar.

1.1.3 Accretion discs

As a PC collapses, material is not directly deposited onto the central protostar. Due to conservation of angular momentum, any initial angular velocity increases in mag-

[1] This is the Jeans length for calculated for a critical Bonnor-Ebert sphere. The properties of these objects are discussed in Chapter 4.

nitude as the core contracts. The resultant centrifugal forces produce an accretion disc. Angular momentum can be transported out of the disc by viscous dissipation due to gravitational or magnetic instabilities (e.g. Stamatellos and Whitworth, 2008; Zhu et al., 2007). This allows material to flow inwards and accrete onto the protostar.

Accretion discs have been observed both directly and indirectly. In Taurus, for example, over half of all pre-Main Sequence stars have an infrared excesses in their spectral energy distribution (SED) (Kenyon and Hartmann, 1995). This is indicative of the presence of heated dust in an accretion disc. The dust is heated by compression, viscous dissipation and protostellar radiation, causing it to re-emit radiation at infrared wavelengths. More recently, observations made using the Hubble Space Telescope and ground-based instruments with adaptive optics have been able to directly resolve these discs (e.g. Padgett et al., 1999; Zinnecker et al., 1999). These discs have radii roughly in the range 10 – 1000 AU with masses in the range 0.001 – 0.1 $M_{\odot}$.

Density perturbations in discs can become gravitationally unstable if two criteria are fulfilled. First, gravity must be able to overcome thermal and centrifugal support, i.e.

$$Q \equiv \frac{c\kappa}{\pi G \Sigma} \lesssim 1 \,, \tag{1.5}$$

where Q is the Toomre parameter (Toomre, 1964), c is the sound speed, κ is the epicyclic frequency and Σ is the surface density. Second, the gas within the disc must cool fast enough so that is not sheared apart (e.g. Stamatellos and Whitworth, 2008), i.e.

$$t_{\rm COOL} < \mathcal{C}(\gamma) t_{\rm ORB} \,, \quad 0.2 \lesssim \mathcal{C}(\gamma) \lesssim 0.5 \,, \tag{1.6}$$

where $t_{\rm COOL}$ is the gas cooling time, $t_{\rm ORB}$ is the orbital period and γ is the adiabatic exponent.

Gravitational instabilities in discs can be very efficient and producing low mass protostars (e.g. Stamatellos and Whitworth, 2008). These instabilities cause discs to fragment rapidly in time periods of $t_{\rm FRAG} \sim 10^3$ yrs. This effect is significantly lessened when simple models of accretion luminosity are included in the simulations (e.g. Bate, 2009c). However, semi-empirical models of episodic accretion can provide long periods of low luminosity, during which disc fragmentation can still occur (Stamatellos et al., 2011, 2012).

1.1.4 Solar-type protostars

In the classical view of core evolution, a core collapses and forms a YSO. YSOs are categorised into four different classes which are sequential in age (Andre et al., 1993; Lada, 1987). We note that this model is incomplete, as it does not account for the formation of high mass or multiple YSOs.

Class 0 is the earliest stage of protostellar evolution (Andre et al., 1993). Here the YSO has just formed and is less massive than the envelope in which it is embedded. The SED resembles a black body spectrum which peaks at submillimetre or far infrared wavelengths. This suggests that surrounding dust and gas is still cool with a temperature of $T \sim 10\,\mathrm{K}$. These objects are usually associated with bipolar outflows of gas. This phase lasts for $t_{\mathrm{CLS\ 0}} \sim 10^4 - 10^5\,\mathrm{yrs}$, during which the YSO accretes roughly half of its final mass at a rate of $\dot{M}_{\mathrm{CLS\ 0}} \gtrsim 10^{-5}\,\mathrm{M}_\odot\,\mathrm{yr}^{-1}$ (Andre et al., 2000; Evans et al., 2009; Lada, 1999).

Class I is the second stage of protostellar evolution. Here the mass of the YSO and the mass of the envelope are roughly equal. The SED still peaks in the submillimetre, but now there is an infrared excess from heated dust in an accretion disc. While the source is now quite luminous from accretion feedback, it is too heavily embedded in its envelope to be observed at optical wavelengths. This phase lasts for $t_{\mathrm{CLS\ I}} \sim 10^5 - 10^6\,\mathrm{yrs}$ with an accretion rate of $\dot{M}_{\mathrm{CLS\ I}} \sim 10^{-6}\,\mathrm{M}_\odot\,\mathrm{yr}^{-1}$ (Evans et al., 2009; Lada, 1999).

Class II is the third stage of protostellar evolution. The mass of the YSO is now much greater than the mass of the envelope. YSOs in this stage are often known as classical T-Tauri stars as they were first observed in Taurus. These objects are now starting to enter the pre-Main Sequence phase of stellar evolution. The SED is dominated by optical or near-infrared radiation from the central star. The infrared excess is still present, although it is not as strong as it was during the Class I phase. This phase lasts for $t_{\mathrm{CLS\ II}} \sim 10^6\,\mathrm{yrs}$ with an accretion rate of $\dot{M}_{\mathrm{CLS\ II}} \sim 10^{-8}\,\mathrm{M}_\odot\,\mathrm{yr}^{-1}$ (Lada, 1999).

Class III is the final stage of protostellar evolution. YSOs in the stage are often known as weak-line T-Tauri stars. The YSO now has almost no envelope. The SED is now very similar to that of a Main Sequence star with the addition of weak Hα emission from atomic hydrogen. This stage lasts for $t_{\mathrm{CLS\ III}} \sim 10^7\,\mathrm{yrs}$ (Lada, 1999), after which the YSO evolves onto the Main Sequence.

1.1.5 Main Sequence stars and the IMF

Objects with $M \gtrsim 0.08\,\mathrm{M}_\odot$ become Main Sequence stars. In these stars, the core becomes hot enough to begin hydrogen burning before it becomes dense enough to be supported by electron degeneracy pressure.

Objects with $M \lesssim 0.08\,\mathrm{M}_\odot$, become Brown Dwarfs (BDs). BDs do not have sufficient mass to begin hydrogen burning; instead they radiate mainly via cooling.

BDs account for roughly 14% – 26% of stellar objects (Andersen et al., 2008), yet it is not well understood how they form. Molecular cores with masses equivalent to BDs are generally not Jeans unstable, so BD formation from core collapse is thought to be rare. A BD mass PC has been observed by André et al. (2012). However, as it is difficult to find efficient mechanisms for producing a high density core with such a low mass, we expect that these objects are rare. Protostellar ejection and disc fragmentation are possible mechanisms for producing BDs. Reipurth and Clarke (2001) propose that if a core produces multiple protostars, then the smallest objects are preferentially ejected from the system. These objects cease to accrete and often have BD masses. Stamatellos and Whitworth (2008) show that accretion discs can also produces BDs. However, we must note that these mechanisms operate over very short time scales, which makes them very difficult to directly verify or reject through observations.

The initial mass function (IMF) is the distribution of masses of newly formed stars. The IMF appears to be roughly universal across most star forming regions in the Galaxy (Kroupa, 2001). The first parametrisation of the IMF was performed by Salpeter (1955) who noted that the distribution of intermediate to high mass stars follows a power law:

$$\frac{\mathrm{d}N_\star}{\mathrm{d}\log(M_\star)} \propto M_\star^{-1.35}\,, \quad 0.4\,\mathrm{M}_\odot < M_\star < 10\,\mathrm{M}_\odot\,, \tag{1.7}$$

where $N_\star$ is the number of stars with mass $M_\star$. This was expanded upon by Kroupa (2001) who parametrised the IMF as a four-part power law:

$$\frac{\mathrm{d}N_\star}{\mathrm{d}\log(M_\star)} \propto M_\star^{-\alpha} \tag{1.8}$$

where

$$\alpha = \begin{cases} -0.7 \pm 0.7\,, & 0.01\,\mathrm{M}_\odot \leq M_\star < 0.08\,\mathrm{M}_\odot\,, \\ 0.3 \pm 0.5\,, & 0.08\,\mathrm{M}_\odot \leq M_\star < 0.5\,\mathrm{M}_\odot\,, \\ 1.3 \pm 0.3\,, & 0.5\,\mathrm{M}_\odot \leq M_\star < 1\,\mathrm{M}_\odot\,, \\ 1.3 \pm 0.7\,, & 1\,\mathrm{M}_\odot \leq M_\star\,. \end{cases} \tag{1.9}$$

Unlike the Salpeter (1955) IMF, this version turns over at masses less than $0.08\,\mathrm{M}_\odot$.

As an alternative to spliced power laws, Chabrier (2003) introduced a lognormal variant of the IMF where

$$\begin{aligned}\frac{\mathrm{d}N_\star}{\mathrm{d}\log(M_\star)} &\propto \exp\left(-\frac{(\log(M_\star/\mathrm{M}_\odot)-\log(\mu))^2}{2\sigma^2}\right), \quad M_\star \leq 1\,\mathrm{M}_\odot \\ &\propto M_\star^{-1.35}, \quad M_\star > 1\,\mathrm{M}_\odot\,.\end{aligned} \tag{1.10}$$

Here $\mu = 0.08$, $\sigma = 0.67$ and $\alpha = -1.35$. These parameters were later changed to $\mu = 0.2$ and $\sigma = 0.55$ (Chabrier, 2005). A comparison of these IMFs is given in figure 1.2.

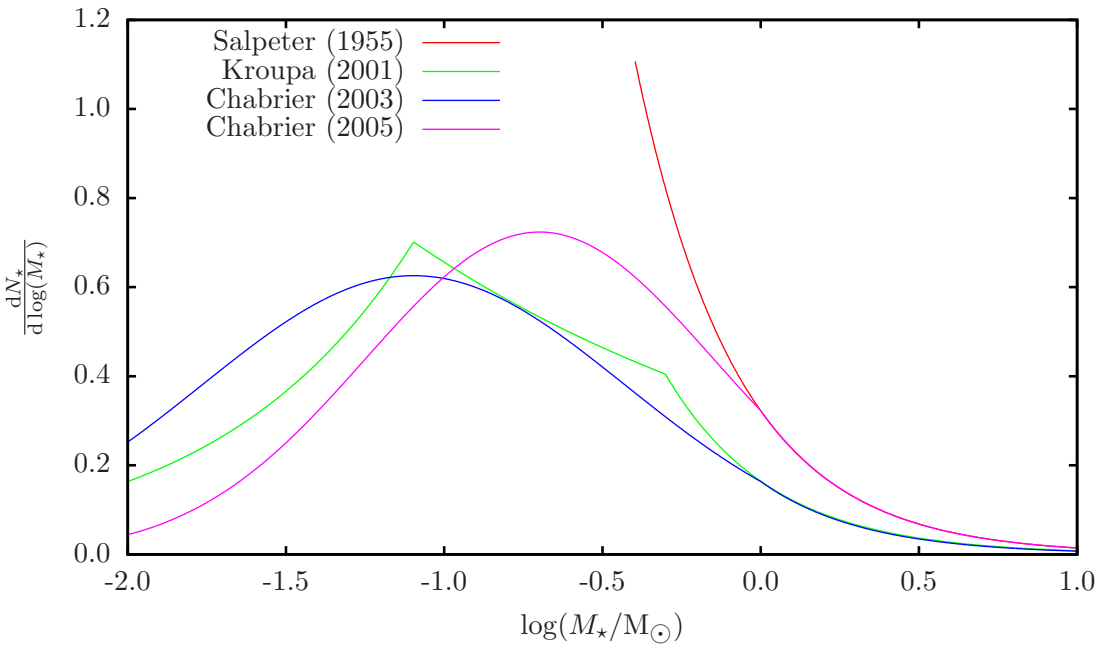

Figure 1.2: Stellar IMFs parametrised by Salpeter (1955), Kroupa (2001) and Chabrier (2003, 2005). The area under each IMF is normalised to 1, with the exception of the Salpeter (1955) IMF which is scaled to match the power-law component of the Chabrier (2005) IMF.

The origin of the IMF is unclear. Some speculate that the IMF is directly inherited from the from the observed distribution of PC masses (CMF) (e.g. Motte et al., 1998; Simpson et al., 2008). These two mass distributions are very similar, except that the CMF is shifted upwards in mass from the IMF by a factor of three or four. Those in favour of this model assume that each PC then collapses into a fixed number of protostars with a fixed star formation efficiency. Possible complications for this model are that there is no physical explaination for why the number of protostars and star formation efficiency should be fixed for all core masses.

Another explaination is the competative accretion hypothesis (e.g. Bonnell and

Bate, 2006; Bonnell et al., 2003). Here, higher mass protostars accrete more gas than lower mass protostars. At the same time, lower mass protostars are likely to be ejected from the system due to N-body interactions. Bonnell et al. (2003) show that this can reproduce a distribution similar to the IMF, but it is difficult for this mechanism to form stellar binary systems.

1.2 Previous numerical work

Previous numerical work has been undertaken to attempt to explain how clouds of molecular gas collapse to form stars. As well as the IMF, a model of star formation needs to reproduce the statistical properties of observerd multiple systems (a useful review of these are provided by Duchêne and Kraus (2013)).

Kroupa (1995a,b) shows that N-body cluster simulations of initially single stars cannot reproduce observed multiplicities, whereas stars initially in binary systems can. This leads to the conclusion that at some point, cores of gas must often fragment into two or more objects.

Early numerical simulations of star formation often involved spherical clouds of gas in solid body rotation (e.g. Hachisu et al., 1987). It has been shown that these systems will often fragment if $\alpha\beta \lesssim 0.15$, where α is the ratio of thermal to gravitational energy and β is the ratio of rotational to graviational energy. Boss and Bodenheimer (1979) also demonstrate that a rotating cloud with an $m = 2$ azimuthal density perturbation can form a binary system.

The more modern picture of star formation involves turbulent flows of gas, as opposed to simple solid-body rotation. In the context of numerical star formation, the term 'turbulence' usually refers to random Gaussian field with a power-law power spectrum $P(k) \propto k^{-\alpha}$ (these terms are explained in Chapter 4). Simulations involving turbulence often come in two flavours: MCs with high levels of turbulence and PCs with low levels of turbulence. Simulations of PCs (e.g. Goodwin and Whitworth, 2004; Goodwin et al., 2004, 2006; Walch et al., 2009, 2012) have shown that star formation is sensitive to the core's initial state. For example, Goodwin et al. (2004) show that the number of YSOs produced in PCs increases with greater levels of turbulent energy. Simulations of MCs (e.g. Bate, 2009b; Bate and Bonnell, 2005; Bonnell et al., 2004; Clark et al., 2008; Girichidis et al., 2012a) have also shown that star formation is dependent on the initial state of the MC. For example, Bate and Bonnell (2005) show that the peak of the mass distribution of YSOs scales with the initial Jeans mass of the MC.

The inclusion of magnetic fields is a relatively new addition to hydrodynamical

simulations, mainly due to computational difficulty. Magnetic fields are very efficient at supressing fragmentation (e.g. Joos et al., 2012; Machida et al., 2005). Given that binaries exist, it is probable that magnetic fields in cores are not dominant over turbulence and self-gravity (Goodwin et al., 2007), however this remains an open topic in star formation.

1.3 Aim of this thesis

We adopt a semi-empirical approach to modelling cores, similar to that of Attwood (2008). We characterise PC properties from observations of cores within the Ophiuchus molecular cloud. We then use this information to set the initial conditions for hundreds of core simulations. This has several advantages over large-scale cloud simulations. The main advantage is that it is faster to run multiple small simulations than individual large simulations. This means we can i) simulate more cores to improve the number statistics of the results and ii) increase the resolution of the simulations to resolve more detailed structure. The trade-off to this approach is that we cannot model core-core interactions or the accretion of material onto cores as they collapse.

In this thesis we address two questions in numerical star formation:

- How do we use the results from observations of star forming regions to generate initial conditions for numerical simulations?

- How do different models of accretion feedback and velocity field structure affect the results of these numerical simulations?

1.3.1 Thesis plan

In Chapter 2 we list and characterise observations of PCs in Ophiuchus. These are used to assign masses, sizes and velocity dispersions to the model PCs.

In Chapter 3 we present a shape fitting analysis which we use to *statistically* deproject the intrinsic shapes of PCs from their projected aspect ratios.

In Chapter 4 we state and justify our assumptions on the density profile and velocity field of the model PCs. We give each core a critical Bonner Ebert density profile and a turbulent velocity field modified to include ordered motions.

In Chapter 5 we provide an overview of Smoothed Particle Hydrodynamics (SPH). This is used to simulate the hydrodynamics and self-gravity of gas in PCs.

In Chapter 6 we describe the additional physics included in the simulations. This includes the transport of radiative energy (Stamatellos et al., 2007a) and semi-empirical models of accretion luminosity (Stamatellos et al., 2011, 2012).

In Chapter 7 we list the initial conditions of the simulations. We also specifically explain how we set up these initial conditions.

In Chapter 8 we present the results from the simulations. We examine the mass distributions and binary statistics of protostars formed in PCs and compare them with observations. We also discuss the effects of different feedback mechanisms and velocity fields on the results.

In the final chapter we summarise the main conclusions from this thesis and discuss plans for future work.

Chapter 2

Ophiuchus

In this chapter we comment on the the prestellar core mass function, noting its similarity to the IMF. We also introduce the Ophiuchus molecular cloud as a well observed region of star formation which contains spatially distinct prestellar cores. Multiple isolated cores can be simulated in greater detail than an entire star forming region, given finite computational resources. Therefore, the cores in Ophiuchus provide useful initial conditions for SPH simulations.

We tabulate the core masses and sizes from three surveys of Ophiuchus by Motte et al. (1998) (MAN98), Stanke et al. (2006) (SSGK06) and Simpson et al. (2008) (SNW08), and internal velocity dispersions by André et al. (2007) (ABMP07). The observed mass distributions are not in good agreement between surveys, but as the core measurements by MAN98 have the largest number of ABMP07 velocity dispersions, we base SPH initial conditions on these data.

Combining observations by MAN98 and ABMP07, we have measurements of core masses, sizes and velocity dispersions in Ophiuchus. However, as there are only 20 cores with all three of these measurements, we use the data to calibrate a multivariate lognormal distribution, from which we can draw an arbitrary number of masses, sizes and velocity dispersions.

2.1 Introduction

Prestellar cores are dense clumps of interstellar matter which are gravitationally bound and expected to collapse to form stars. Observations suggest that the distribution of prestellar core masses, or core mass function (CMF), is roughly lognormal with a power-law tail at the high mass end (e.g. Alves et al., 2007; Enoch et al., 2008, 2006; Johnstone and Bally, 2006; Johnstone et al., 2001, 2000; Könyves et al., 2010; Motte et al., 1998, 2001; Nutter and Ward-Thompson, 2007; Rathborne et al.,

2009; Simpson et al., 2008; Stanke et al., 2006; Testi and Sargent, 1998). Chabrier (2005) shows that the distribution of observed stellar masses, or initial mass function (IMF), is also roughly lognormal with a power-law tail.

Both the CMF and the IMF have similar shapes, where the IMF is shifted downwards in mass by a factor of $F \sim 4 \pm 1$. This has lead to speculation that the shape of the IMF is inherited directly from the shape of the CMF. There are two assumptions implied by this statement: i) stars form predominantly in prestellar cores instead of, for example, colliding filaments or in the swept up shell of material around HII regions; ii) star formation in prestellar cores is a statistically self-similar process. By this we mean that each core converts a fraction η of its total gas into $N_\star$ stars, with the constraints that η and $N_\star$ are independent of core mass and $N_\star/\eta \sim F$.

In this thesis, we follow the assumption that most stars form in isolated cores (we address this assumption in Section 2.3). We trace the transformation of the CMF to the IMF through large ensembles of SPH simulations. In Section 2.2 of this chapter we describe and compare the observations of Ophiuchus; in Section 2.3 we give an analysis of the cores which suggests they form in isolation; in Section 2.4 we explain how we use the observations to calibrate a multivariate lognormal distribution from which we can draw core parameters.

2.2 Observations

The L1688 cloud within the Ophiuchus molecular cloud complex (hereafter L1688 is referred to as Ophiuchus) has been observed by (Motte et al., 1998) (MAN98), (Stanke et al., 2006) (SSGK06) and (Simpson et al., 2008) (SNW08). They map millimetre and sub-millimetre dust emission from the region to estimate the masses and sizes of prestellar cores. Lada (1999) estimates that Ophiuchus has total mass $M_{\rm OPH} \sim 1 - 2 \times 10^3\,{\rm M}_\odot$ and diameter $D_{\rm OPH} \sim 1\,{\rm pc}$. The distribution of cores in Ophiuchus is sub-clustered into regions Oph-A, Oph-B1, Oph-B2, Oph-C, Oph-D, Oph-E, Oph-F and Oph-J. The relative positions and sizes of these regions are shown in Figures 2.1 and 2.3. MAN98 and SNW08 note that their observations are good sensitivity level and that their derivations of the Ophiuchus CMF should be almost complete down to masses of approximately $0.1\,{\rm M}_\odot$.

These masses are complemented by observations of core velocity dispersions in Ophiuchus by André et al. (2007) (ABMP07). They note that the large-scale flow of material within these cores is mostly subsonic or transonic. They also measure the relative velocity between prestellar cores and conclude that most of the cores in

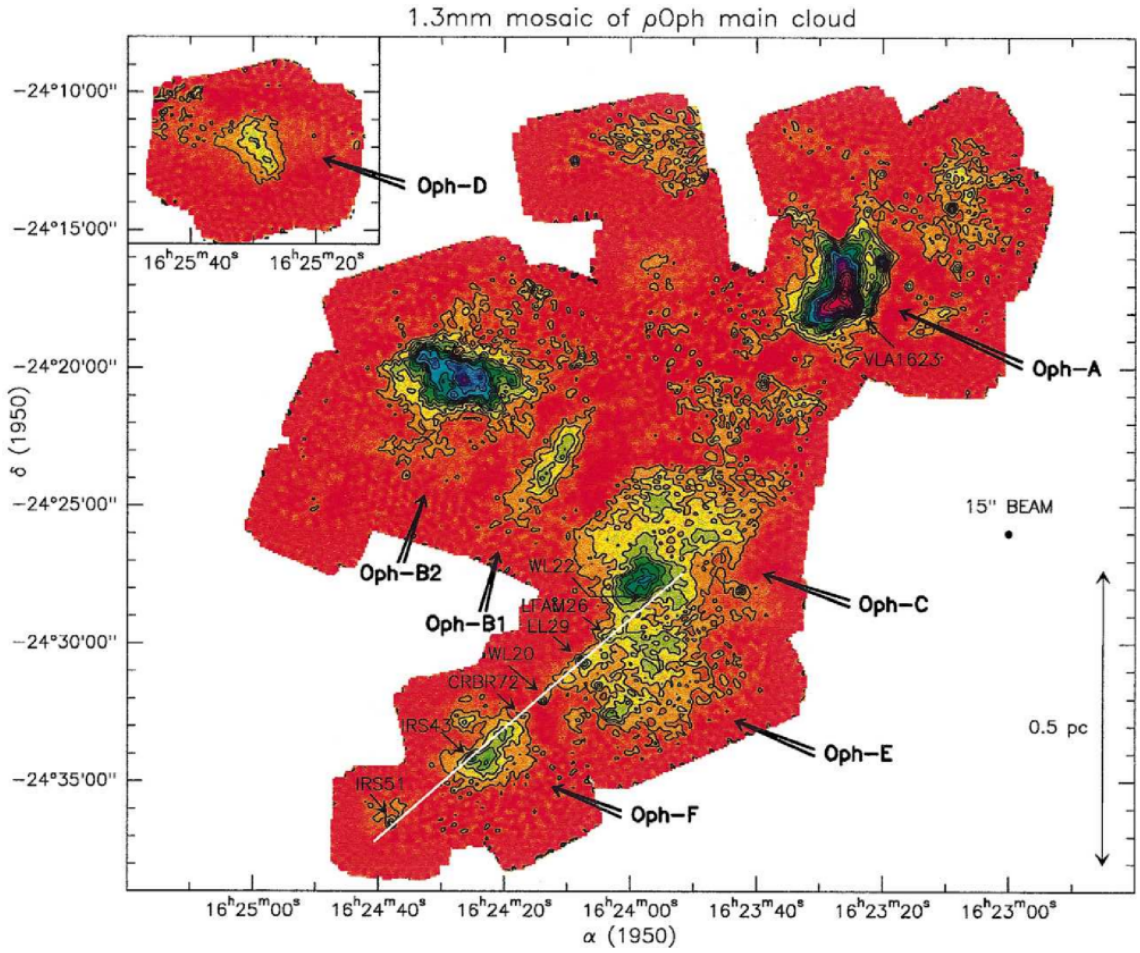

Figure 2.1: 1.3 mm dust emission intensity map of the Ophiuchus main cloud, taken from Motte et al. (1998). Contour levels range from 5 MJy/sr to 280 MJy/sr in roughly equal logarithmic intervals.

Ophiuchus are likely to collapse before they interact with one another.

In this section we discuss and compare the observations by MAN98, SSGK06, SNW08 and ABMP07. Core masses, sizes and velocity dispersions are given in Table 2.1 .

2.2.1 MAN98

MAN98 map dust emission at 1.3 mm within Ophiuchus using the MPIfR bolometer array on the IRAM 30 m telescope. Their map covers an area of ~ 480 arcmin^2 and includes the Oph-A, Oph-B1, Oph-B2, Oph-C, Oph-D, Oph-E and Oph-F sub-regions. They use *Gaussclumps* (Stutzki and Guesten, 1990) to extract 61 cores, 36 of which have resolved sizes. MAN98 define the size of a core as the full-width at half-maximum (FWHM) of the core's surface brightness. The masses and sizes are given in Table 2.1 and the intensity map is shown in Figure 2.1 .

Table 2.1: Observations of prestellar cores in Ophiuchus. Column 1 gives the region in Ophiuchus; Column 2 gives the core ID as defined by MAN98; column 3 gives the core ID as defined by SSGK06; column 4 gives SNW08 core mass; column 5 gives the SSGK06 core mass; column 6 gives the MAN98 core mass; columns 7 and 8 give the major and minor size components of the SNW08 cores; columns 9 and 10 give the major and minor FWHM of the SSGK06 cores; columns 11 and 12 give the major and minor FWHM of the MAN98 cores; column 13 gives the core radial velocity dispersion; column 14 gives the thermal component of the radial velocity dispersion; column 15 gives the non thermal component of the radial velocity disperion.

Region	ID_{MAN98}	ID_{SSGK06}	M_{SNW08}	M_{SSGK08}	M_{MAN98}	$Size_{SNW08}$		$FWHM_{SSGK06}$		$FWHM_{MAN98}$		σ_{1D}	σ_T	σ_{NT}
						maj	min	maj	min	maj	min			
			($M_\odot$)			(AU)						($km\,s^{-1}$)		
Oph-A	A-MM1		0.170		0.089								0.056	
Oph-A	A-MM1/2/3	MMS014		1.305				9313	4448				0.056	
Oph-A	A-MM2				0.142								0.056	
Oph-A	A-MM2/3		0.295			2800	1900						0.056	
Oph-A	A-MM3				0.089								0.056	
Oph-A	A-MM4	MMS026	0.416	0.813	0.248	2100	2100	10008	3892	3475	1216	0.161	0.056	0.150
Oph-A	A-MM5	MMS050	0.711	0.960	0.407	2800	2500	10842	5421	3214	2519	0.078	0.056	0.054
Oph-A	A-MM6		1.812		0.709	3600	2500			2780	2346		0.056	
Oph-A	A-MM6/7	MMS007		4.246				10703	7089				0.056	
Oph-A	A-MM7		0.792		0.230	3300	2200			1216	1216		0.056	
Oph-A	A-MM8		2.733		0.230	2200	1900			2519	1824	0.141	0.056	0.129
Oph-A	A-MM11		0.555			5600	1900						0.056	
Oph-A	A-MM12		0.389										0.056	
Oph-A	A-MM16		0.027										0.056	
Oph-A	A-MM17		0.027			1900	1900						0.056	
Oph-A	A-MM18		0.751			4200	2800						0.056	

Observations of prestellar cores in Ophiuchus.

Region	ID_{MAN98}	ID_{SSGK06}	M_{SNW08}	M_{SSGK08}	M_{MAN98}	$Size_{SNW08}$		$FWHM_{SSGK06}$		$FWHM_{MAN98}$		σ_{1D}	σ_T	σ_{NT}
						maj	min	maj	min	maj	min			
				($M_\odot$)		(AU)						($km\,s^{-1}$)		
Oph-A	A-MM20		0.107										0.056	
Oph-A	A-MM21		0.183										0.056	
Oph-A	A-MM22		0.094			2800	2200						0.056	
Oph-A	A-MM23		1.060			4900	2100						0.056	
Oph-A	A-MM26		0.367			3100	1900						0.056	
Oph-A	A-MM27		0.291			4200	1900						0.056	
Oph-A	A-MM28		0.183			2500	1900						0.056	
Oph-A	A-MM29		0.157										0.056	
Oph-A	A-MM30		1.100			4400	1900						0.056	
Oph-A	A-N	MMS074	0.183	0.612	0.106			24047	5143				0.056	
Oph-A	A-S	MMS053	0.004	0.284	0.142	2100	1900	8896	5977				0.056	
Oph-A	A2	MMS063		0.376				8062	6811				0.056	
Oph-A	A2	MMS069		0.173				7645	4309				0.056	
Oph-A	A2-MM1	MMS057	0.286	0.533	0.177	3300	1900	9313	7923	3909	834		0.056	
Oph-A	A3-MM1	MMS046	0.286	0.141	0.177	2500	2200	7367	3892				0.056	
Oph-A	SM1		6.325		5.669	6100	1900					0.272	0.056	0.266
Oph-A	SM1/SM1N	MMS001		10.523				9035	4587				0.056	
Oph-A	SM1N		2.505		2.303	2500	1900			2606	1564	0.185	0.056	0.176
Oph-A	SM2	MMS004	5.140	13.880	2.303	5100	3600	13205	7923	5386	2954	0.164	0.056	0.154
Oph-A	VLA1623		2.518			4200	2500					0.532	0.056	0.529
Oph-B	B1	MMS027		2.622				10147	10008				0.054	
Oph-B	B1	MMS086		0.187				7645	4031				0.054	

Observations of prestellar cores in Ophiuchus.

Region	ID_{MAN98}	ID_{SSGK06}	M_{SNW08}	M_{SSGK08}	M_{MAN98}	$Size_{SNW08}$		$FWHM_{SSGK06}$		$FWHM_{MAN98}$		σ_{1D}	σ_T	σ_{NT}
						maj	min	maj	min	maj	min			
				($M_\odot$)		(AU)						($km\,s^{-1}$)		
Oph-B	B1-MM1	MMS066	0.027	0.710	0.101			11815	5977				0.054	
Oph-B	B1-MM2	MMS028	1.160	1.388	0.171	3100	1900	9313	6950	2606	1824	0.064	0.054	0.035
Oph-B	B1-MM3	MMS020	2.244	1.827	0.161	2800	2500	12788	9174	1564	1129	0.106	0.054	0.092
Oph-B	B1-MM4	MMS023	1.805	0.295	0.212	5000	3200	5699	4309	3996	2780	0.157	0.054	0.148
Oph-B	B1-MM6		0.190			2500	1900						0.054	
Oph-B	B1-MM7		0.098			1900	1900						0.054	
Oph-B	B1B2-MM1	MMS049	0.190	0.812	0.101	5600	2200	11954	7367	2346	1564	0.092	0.054	0.075
Oph-B	B1B2-MM2	MMS061		0.596	0.333								0.054	
Oph-B	B2-MM1	MMS056		1.029	0.141			11259	9730			0.078	0.054	0.057
Oph-B	B2-MM2	MMS033	0.753	0.991	0.474	3300	2200	10564	5282	3909	2085		0.054	
Oph-B	B2-MM3				0.121								0.054	
Oph-B	B2-MM3/4/5	MMS031		2.093				12232	6811				0.054	
Oph-B	B2-MM4		0.824		0.272					1824	834	0.111	0.054	0.098
Oph-B	B2-MM5		0.981		0.262	3600	2500			1911	834	0.130	0.054	0.118
Oph-B	B2-MM6	MMS037	1.393	2.733	0.787	5000	4200	10703	7645	3736	2346	0.180	0.054	0.172
Oph-B	B2-MM7		0.537		0.232	4200	2800						0.054	
Oph-B	B2-MM8		1.702		1.513	2800	2500			3475	3475	0.178	0.054	0.170
Oph-B	B2-MM9		1.176		0.313	3900	1900			1390	834		0.054	
Oph-B	B2-MM9/12	MMS029		0.969				6811	4170				0.054	
Oph-B	B2-MM11				0.151							0.269	0.054	0.263
Oph-B	B2-MM12				0.393					1824	1129	0.101	0.054	0.086
Oph-B	B2-MM13		0.423		0.192	3100	2800						0.054	

Observations of prestellar cores in Ophiuchus.

Region	ID_{MAN98}	ID_{SSGK06}	M_{SNW08}	M_{SSGK08}	M_{MAN98}	$Size_{SNW08}$		$FWHM_{SSGK06}$		$FWHM_{MAN98}$		σ_{1D}	σ_T	σ_{NT}
						maj	min	maj	min	maj	min			
				($M_\odot$)		(AU)						($km\,s^{-1}$)		
Oph-B	B2-MM14		1.079		0.434	4400	2100			1824	1564		0.054	
Oph-B	B2-MM15	MMS021	0.537	1.140	0.171			13622	6116			0.094	0.054	0.077
Oph-B	B2-MM16		1.133		0.353	2500	2200			2346	1129	0.181	0.054	0.173
Oph-B	B2-MM16/17	MMS018		4.606				10842	9174				0.054	
Oph-B	B2-MM17				0.232							0.136	0.054	0.125
Oph-B	B3	MMS108		0.828				17097	8896				0.054	
Oph-B	B3	MMS118		0.281				10703	7506				0.054	
Oph-B	B3	MMS143		0.543				13900	7089				0.054	
Oph-C	C-MM1	MMS059		0.958	0.353			10008	8618	5126	2606		0.054	
Oph-C	C-MM2		0.954		0.121								0.054	
Oph-C	C-MM3		1.225		0.232	4200	3300			4691	556		0.054	
Oph-C	C-MM4				0.161					2085	1216		0.054	
Oph-C	C-MM5		1.068		0.101							0.101	0.054	0.086
Oph-C	C-MM6		0.905		0.333	6700	3300			3475	3214	0.106	0.054	0.091
Oph-C	C-MM7				0.131								0.054	
Oph-C	C-MM8		0.130										0.054	
Oph-C	C-MM9		0.049			2200	2100						0.054	
Oph-C	C-MM10		0.314			2400	1900						0.054	
Oph-C	C-MM12		0.081			4400	2400						0.054	
Oph-C	C-N	MMS044	1.377	3.513	1.714	4700	3800	16958	12649	8688	7645		0.054	
Oph-C	C-S	MMS022		6.641				15568	11259				0.054	
Oph-C	C-S	MMS039		1.771				10425	8201				0.054	

Observations of prestellar cores in Ophiuchus.

Region	ID_{MAN98}	ID_{SSGK06}	M_{SNW08}	M_{SSGK08}	M_{MAN98}	$Size_{SNW08}$		$FWHM_{SSGK06}$		$FWHM_{MAN98}$		σ_{1D}	σ_T	σ_{NT}
						maj	min	maj	min	maj	min			
				($M_\odot$)		(AU)						($km\,s^{-1}$)		
Oph-C	C-W	MMS055		7.190	1.412			25020	19460	14769	6950		0.054	
Oph-D	D-MM1				0.151					2346	1477		0.054	
Oph-D	D-MM1/2	MMS047		1.217				10425	7784				0.054	
Oph-D	D-MM2				0.161					3475	2259		0.054	
Oph-D	D-MM3				0.081								0.054	
Oph-D	D-MM3/4/5	MMS052		2.516				16402	11537				0.054	
Oph-D	D-MM4				0.171					3301	2259		0.054	
Oph-D	D-MM5				0.071								0.054	
Oph-E	E-MM1				3.080					19981	16506		0.054	
Oph-E	E-MM2	MMS036		2.765				15290	9730				0.054	
Oph-E	E-MM2a		0.108		0.098	1900	1900						0.054	
Oph-E	E-MM2b		0.136		0.112	3100	2500						0.054	
Oph-E	E-MM2c				0.112								0.054	
Oph-E	E-MM2d		0.358		0.630					3649	2346	0.107	0.054	0.093
Oph-E	E-MM3				0.112								0.054	
Oph-E	E-MM4	MMS067	0.266	0.361	0.616	3600	3100	7089	5838	5994	4604	0.108	0.054	0.094
Oph-E	E-MM5		0.239		0.588	2800	2100			6689	3996		0.054	
Oph-E	E-MM8		0.163			3100	1900						0.054	
Oph-F	F-MM1		0.900		0.350	4200	2400			4170	2259	0.140	0.054	0.129
Oph-F	F-MM2				0.168					2346	1390	0.132	0.054	0.120
Oph-F	F-MM2a		0.954			4400	3800						0.054	
Oph-F	F-MM6		0.081										0.054	

Observations of prestellar cores in Ophiuchus.

Region	ID_{MAN98}	ID_{SSGK06}	M_{SNW08}	M_{SSGK08}	M_{MAN98}	$Size_{SNW08}$ maj	$Size_{SNW08}$ min	$FWHM_{SSGK06}$ maj	$FWHM_{SSGK06}$ min	$FWHM_{MAN98}$ maj	$FWHM_{MAN98}$ min	σ_{1D}	σ_T	σ_{NT}
			($M_\odot$)			(AU)						($km\,s^{-1}$)		
Oph-F	F-MM8		0.179										0.054	
Oph-F	F-MM9		0.081										0.054	
Oph-J	J-MM2		0.363			4700	3200						0.054	
Oph-J	J-MM3		0.298			3900	2500						0.054	
Oph-J	J-MM4		0.152										0.054	
Oph-J	J-MM5		0.136										0.054	
Oph-J	J-MM6		0.065										0.054	
Oph-J	J-MM7		0.054										0.054	
		MMS012		1.761				10147	7645				0.054	
		MMS017		1.819				14039	5977				0.054	
		MMS030		4.152				19738	12788				0.054	
		MMS038		0.945				8896	5699				0.054	
		MMS041		4.490				20850	11954				0.054	
		MMS048		1.371				11954	9730				0.054	
		MMS051		0.870				10286	6394				0.054	
		MMS054		2.349				15151	10286				0.054	
		MMS065		0.191				5838	4726				0.054	
		MMS068		1.101				20155	9869				0.054	
		MMS072		0.535				8896	6811				0.054	
		MMS073		2.020				23908	9313				0.054	
		MMS075		0.059				5838	2502				0.054	
		MMS077		0.265				10703	5699				0.054	

Observations of prestellar cores in Ophiuchus.

Region	ID_{MAN98}	ID_{SSGK06}	M_{SNW08}	M_{SSGK08}	M_{MAN98}	$Size_{SNW08}$ maj	$Size_{SNW08}$ min	$FWHM_{SSGK06}$ maj	$FWHM_{SSGK06}$ min	$FWHM_{MAN98}$ maj	$FWHM_{MAN98}$ min	σ_{1D}	σ_T	σ_{NT}
			($M_\odot$)			(AU)						($km\,s^{-1}$)		
		MMS078		0.067				3753	3614				0.054	
		MMS079		0.564				12927	5977				0.054	
		MMS080		1.237				13344	11120				0.054	
		MMS081		0.934				17792	9035				0.054	
		MMS082		0.537				23213	4587				0.054	
		MMS083		0.286				12927	4726				0.054	
		MMS084		1.420				27800	11815				0.054	
		MMS085		0.645				10425	7228				0.054	
		MMS087		1.979				17375	9869				0.054	
		MMS088		2.837				36001	12510				0.054	
		MMS089		1.017				12510	10147				0.054	
		MMS090		1.144				18904	10008				0.054	
		MMS091		2.211				24742	20294				0.054	
		MMS092		0.801				11815	9313				0.054	
		MMS093		2.794				24464	15429				0.054	
		MMS094		2.516				30858	13066				0.054	
		MMS095		1.576				24603	15985				0.054	
		MMS096		0.866				20294	12510				0.054	
		MMS097		0.936				19182	9591				0.054	
		MMS098		0.910				27939	11815				0.054	
		MMS099		4.222				39336	17375				0.054	
		MMS100		1.012				29468	8896				0.054	

Observations of prestellar cores in Ophiuchus.

Region	ID_{MAN98}	ID_{SSGK06}	M_{SNW08}	M_{SSGK08}	M_{MAN98}	$Size_{SNW08}$ maj	$Size_{SNW08}$ min	$FWHM_{SSGK06}$ maj	$FWHM_{SSGK06}$ min	$FWHM_{MAN98}$ maj	$FWHM_{MAN98}$ min	σ_{1D}	σ_T	σ_{NT}
			($M_\odot$)			(AU)						($km\,s^{-1}$)		
		MMS101		1.029				17653	13344				0.054	
		MMS102		0.515				18765	6672				0.054	
		MMS103		0.513				11954	7089				0.054	
		MMS104		1.852				19599	16541				0.054	
		MMS105		1.696				26549	18209				0.054	
		MMS106		0.268				8896	6950				0.054	
		MMS107		2.363				38502	14456				0.054	
		MMS109		0.937				21823	13622				0.054	
		MMS110		0.405				24464	8896				0.054	
		MMS111		0.286				15429	7367				0.054	
		MMS112		0.434				13205	6950				0.054	
		MMS113		0.542				15985	9452				0.054	
		MMS114		0.354				12232	8062				0.054	
		MMS115		1.202				21962	15151				0.054	
		MMS116		1.928				25159	18348				0.054	
		MMS117		0.500				9869	7506				0.054	
		MMS119		0.394				11120	10147				0.054	
		MMS120		0.149				10842	5004				0.054	
		MMS121		0.294				12232	9035				0.054	
		MMS122		0.388				12649	10425				0.054	
		MMS123		0.434				19182	13761				0.054	
		MMS124		0.179				13205	6672				0.054	

Observations of prestellar cores in Ophiuchus.

Region	ID_{MAN98}	ID_{SSGK06}	M_{SNW08}	M_{SSGK08}	M_{MAN98}	$Size_{SNW08}$ maj	$Size_{SNW08}$ min	$FWHM_{SSGK06}$ maj	$FWHM_{SSGK06}$ min	$FWHM_{MAN98}$ maj	$FWHM_{MAN98}$ min	σ_{1D}	σ_T	σ_{NT}
			($M_\odot$)			(AU)						($km\,s^{-1}$)		
		MMS125		0.332				13344	7228				0.054	
		MMS127		0.712				17375	12371				0.054	
		MMS128		1.552				20572	17375				0.054	
		MMS129		1.850				26688	22657				0.054	
		MMS130		1.307				32387	13622				0.054	
		MMS131		1.522				33082	19738				0.054	
		MMS132		1.512				42533	17097				0.054	
		MMS133		1.396				42672	22101				0.054	
		MMS134		0.677				22379	17236				0.054	
		MMS135		0.372				20572	11954				0.054	
		MMS136		0.843				23352	14317				0.054	
		MMS137		0.540				21962	12510				0.054	
		MMS138		0.632				21267	16402				0.054	
		MMS139		1.223				23352	16958				0.054	
		MMS142		1.680				18487	9174				0.054	

The core masses and sizes stated here are different from those given in the original publication. The mass of a prestellar core is estimated to be

$$M_{\rm C} = \frac{S(\lambda)D^2}{\kappa(\lambda)B(\lambda,T)} \tag{2.1}$$

where $S(\lambda)$ is the total dust continuum flux density from the core measured at wavelength λ, D is the distance to the source, $\kappa(\lambda)$ is dust opacity at wavelength λ and $B(\lambda,T)$ is the Planck function at wavelength λ and temperature T. For $\lambda = 1.3\,\mathrm{mm}$, MAN98 adopt $\kappa(1.3\,\mathrm{mm}) = 0.005\,\mathrm{cm^2\,g^{-1}}$.

At the time of publication, MAN98 used dust temperature estimates which have since been revised by Stamatellos et al. (2007b). These temperatures, $T_{\rm MAN98}$ and $T_{\rm SWW07}$ are given in Table 2.2. The distance to Ophiuchus given by MAN98, $D_{\rm MAN98} = 160\,\mathrm{pc}$, has also been revised by Mamajek (2008) to $D_{\rm M08} = 139 \pm 6\,\mathrm{pc}$. To account for this, each mass given by MAN98 receives the transformation

$$M_{\rm MAN98} \rightarrow \frac{B(1.3\,\mathrm{mm}, T_{\rm MAN98})D^2_{\rm M08}}{B(1.3\,\mathrm{mm}, T_{\rm SWW07})D^2_{\rm MAN98}} M_{\rm MAN98}\,, \tag{2.2}$$

and each size receives the transformation

$$\mathrm{FWHM}_{\rm MAN98} \rightarrow \frac{D_{\rm M08}}{D_{\rm MAN98}} \mathrm{FWHM}_{\rm MAN98}\,. \tag{2.3}$$

The dust temperatures $T_{\rm SWW07}$ are cooler than $T_{\rm MAN98}$, which increases the estimated core mass. However, the revised distance $D_{\rm M08}$ is less than $D_{\rm MAN98}$, which decreases the core mass. The combined effect modestly increases the mass of cores within Oph A, Oph E and Oph F, whilst leaving the masses of cores in Oph B, Oph C and Oph D unchanged.

2.2.2 SSGK06

SSGK06 map dust emission at 1.2 mm over a large area of the sky (almost a square degree) around Ophiuchus. They use the SIMBA bolometer array on the SEST telescope and extract 111 prestellar cores using *Clumpfind* (Williams et al., 1994). They give flux densities and, when resolved, the beam-convolved FWHM for each source. Whilst SSGK06 have a greater number of observed cores than MAN98 and SNW08, they have fewer cores in the Ophiuchus main cloud. The intensity map is shown in Figure 2.2 .

We use Equation (2.1) to estimate masses from these flux densities, assuming $T = T_{\rm SWW07}$[2] and $D = 139\,\mathrm{pc}$. The value of $\kappa(\lambda)$ is assumed to scale as $\kappa \propto \lambda^{-\beta}$

[2]We assume $T = T_{\rm SWW07}$ for cores within L1688. For cores outside L1688, we assume $T = 10\,\mathrm{K}$.

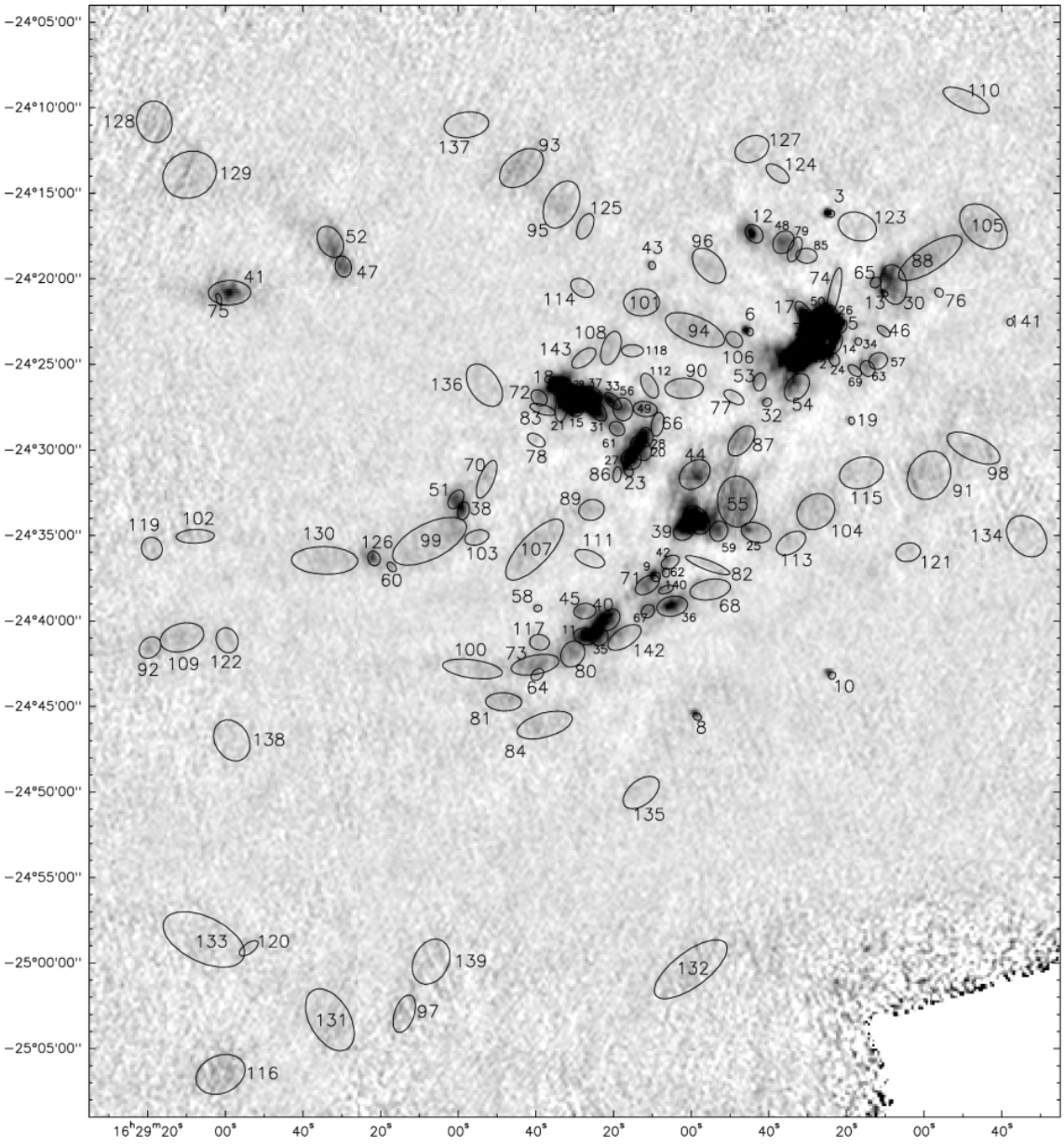

Figure 2.2: 1.2 mm dust emission intensity map of the Ophiuchus main cloud and surrounding region, taken from Stanke et al. (2006). The ellipses show the size and position of extracted cores.

Region	$T_{\rm MAN98}$ (K)	$T_{\rm SWW07}$ (K)	$\times M_{1.3}$
Oph A	20	11	1.77
Oph B	12	10	1.01
Oph C	12	10	1.01
Oph D	12	10	1.01
Oph E	15	10	1.40
Oph F	15	10	1.40
Oph J	-	10	-

Table 2.2: Dust temperatures given by MAN98 and SWW07. The fourth column gives the multiplication factor applied to the original MAN98 core masses when we assume $T = T_{\rm SWW07}$ and $D = 139\,{\rm pc}$.

where $\beta \approx 2$ at millimetre wavelengths (Hildebrand, 1983). Extrapolating from $\kappa(1.3\,{\rm mm}) = 0.005\,{\rm cm^2\,g^{-1}}$, we assume that $\kappa(1.2\,{\rm mm}) = 0.006\,{\rm cm^2\,g^{-1}}$. The masses and sizes are given in Table 2.1 .

2.2.3 SNW08

SNW08 analyse observations of dust emission at 850 μm in Ophiuchus acquired from the Canadian Astronomy Data Centre's JCMT data archive (Tilanus et al., 1997). The data cover an area of $\sim 700\,{\rm arcmin^2}$ that includes Oph-A, Oph-B1, Oph-B2, Oph-C, Oph-E Oph-F and Oph-J. Sources with a peak brightness 5σ or more above the background noise level were extracted by eye from within a closed 3σ noise contour. Spatially resolved cores were given a size defined by an ellipse fitted to the 3σ contour. The intensity map is shown in figure 2.3

The masses here are the same as those stated by SNW08. Their mass calculations follow Equation 2.1 and they assume $T = T_{\rm SWW07}$ and $D = 139\,{\rm pc}$ with $\kappa(850\,\mu{\rm m}) = 0.01\,{\rm cm^2\,g^{-1}}$. The masses and sizes are given in Table 2.1 .

2.2.4 ABMP07

ABMP07 measure the width of the $N_2H^+(1–0)$ emission line from 27 prestellar cores within Ophiuchus. Of these 27 prestellar cores, 26 have mass estimates from MAN98. The line widths show the radial velocity dispersion, $\sigma_{\rm 1D}$, of N_2H^+ molecules within prestellar cores. These velocities have thermal and non-thermal components where

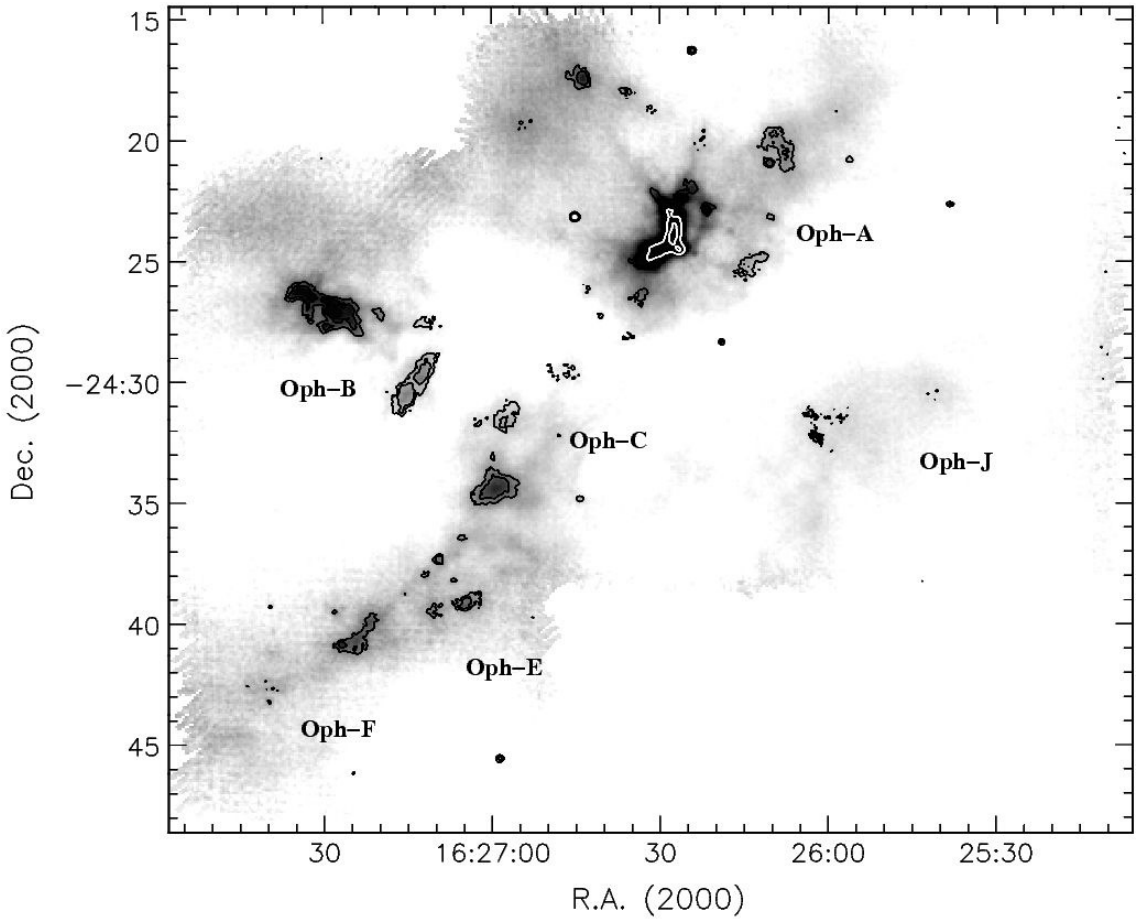

Figure 2.3: 850 µm dust emission intensity of the Ophiuchus main cloud, taken from Simpson et al. (2008). Black contours levels show 5σ and 10σ noise levels. White contours show 25σ and 100σ noise levels. The 1σ noise level varies from 4 MJy/sr to 11 MJy/sr.

$\sigma_{1D}^2 = \sigma_T^2 + \sigma_{NT}^2$ and the thermal component, σ_T, is given by

$$\sigma_T^2 = \frac{k_B T}{m_{MOL}} . \tag{2.4}$$

Here $m_{MOL} = 4.8 \times 10^{-23}\,\mathrm{g}$ is the mass of the N_2H^+ molecule. The non-thermal component, σ_{NT}, gives the magnitude of macroscopic gas motions, i.e. turbulence, rotation and contraction or expansion.

We list values of σ_{1D}, σ_T and σ_{NT} in Table 2.1. Note that σ_T and σ_{NT} are different to the values given by ABMP07 as we have assumed $T = T_{SWW07}$.

2.2.5 Comparison of Observations

There is some concern when comparing the masses observed by MAN98, SSGK06 and SNW08. As shown in figure 2.4, the derived CMFs from these surveys have peaks which vary by almost an order of magnitude. The peak of the MAN98 CMF is at $\sim 0.2\,\mathrm{M}_\odot$, the peak of the SSGK06 CMF is at $\sim 1\,\mathrm{M}_\odot$ and the peak of the SNW08 CMF is at $\sim 0.4\,\mathrm{M}_\odot$. These results are even more disparate when we look at specific cores like B1-MM2 with $M_{SNW08} = 1.2\,\mathrm{M}_\odot$, $M_{SSGK06} = 1.4\,\mathrm{M}_\odot$ and $M_{MAN98} = 0.2\,\mathrm{M}_\odot$, and B1-MM4 with $M_{SNW08} = 1.8\,\mathrm{M}_\odot$, $M_{SSGK06} = 0.3\,\mathrm{M}_\odot$ and $M_{MAN98} = 0.2\,\mathrm{M}_\odot$. Note that for B1-MM2 the SSGK06 mass roughly agrees with the SNW08 mass, but for B1-MM4, the SSGK06 mass roughly agrees with the MAN98 mass. It is our view that the different core extraction procedures used for each data set are the the main source of error. While the opacity of the sky will cause some differences between observations, extracting the cores from the background structure of the molecular cloud introduces considerable uncertainties in their column densities.

The cores observed by MAN98 have the largest number of velocity dispersions from ABMP07. This means that these two sets of observations will be the most effective at tracing the correlation between mass and velocity dispersion. Indeed, the observations by ABMP07 are a follow up to those by MAN98, so these two sets of results are the most consistent with one another. Therefore, for these reasons, we will use the MAN98 masses as the basis for initial conditions of simulations of prestellar cores.

[3]The probability density $P(\log(M))$ is calculated by smoothing each data point $\log(M)_i$ over a Gaussian kernel. For any value of $\log(M)$, $P(\log(M))$ is given by

$$P(\log(M)) = \frac{1}{N}\sum_{i=1}^{N} \frac{1}{\sqrt{2\pi h^2}} \exp\left(-\frac{(\log(M) - \mu_i)^2}{2h^2}\right) , \tag{2.5}$$

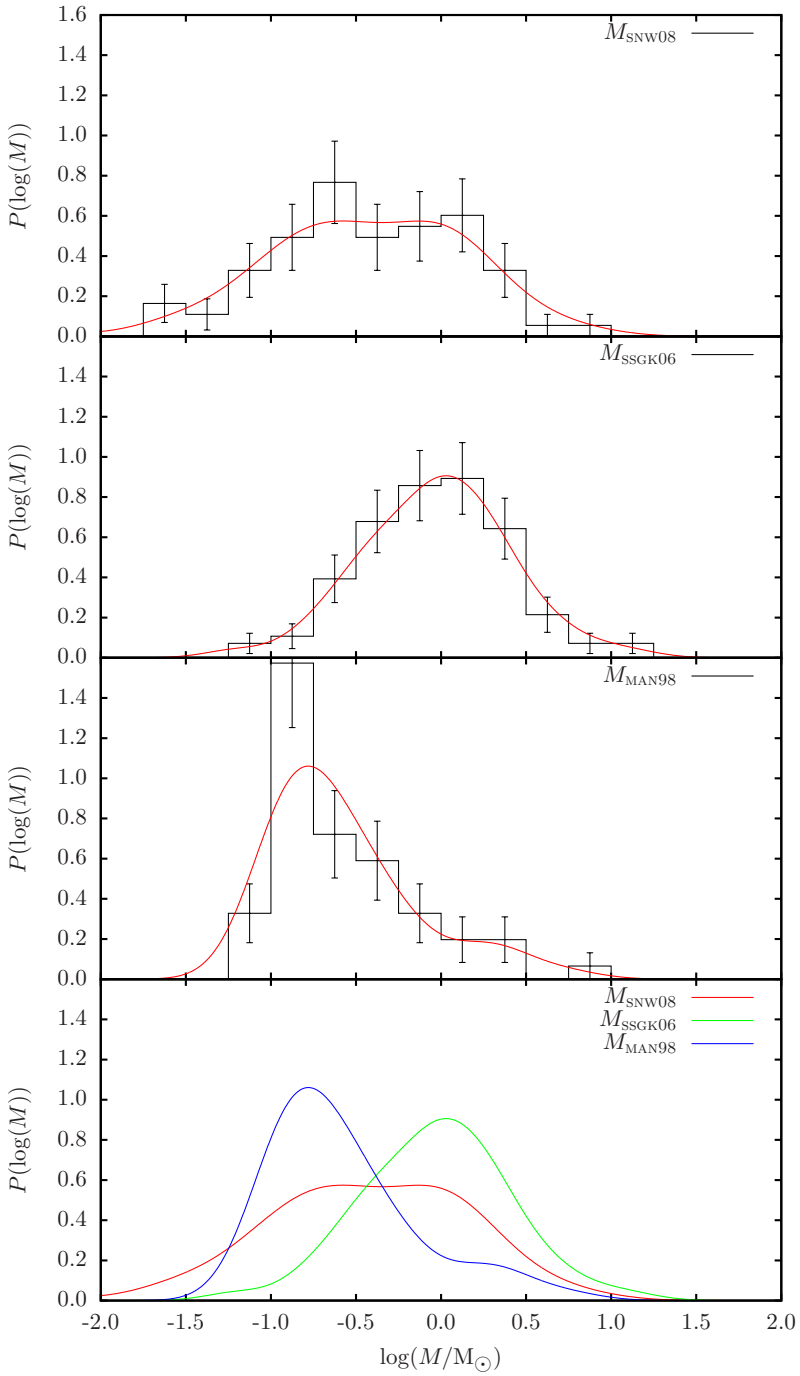

Figure 2.4: Measured CMFs in Ophiuchus. The black lines are histograms with a fixed bin width of 0.25 dex and the red lines a kernel smoothed probability density estimates[3]. The top panel gives the CMF measured by SNW08; the second panel down gives the CMF measured by SSGK06; the third panel down gives the CMF measured by MAN98; the bottom panel compares the CMFs of all three with SNW08 in red, SSGK06 in green and MAN98 in blue.

2.3 Isolated cores

In this thesis we treat cores as isolated objects; that is to say that we evolve individual cores in a vaccum. In reality they are not isolated, but embedded in molecular clouds. For convenience, we will assume that the cores' environment do not strongly affect star formation, but we conceed that this assumption may have to be relaxed in future. We can, however, test to see if time scale of core-core interactions is greater than core free fall times.

ABMP07 provide the bulk velocities of cores within Ophiuchus. As a collection of individual objects, these cores have a radial velocity dispersion $\sigma_{\rm 1D,C} = 0.36\,{\rm km\,s^{-1}}$. ABMP07 also give the diameter of the region $D_{\rm O} = 1.1\,{\rm pc}$. Assuming the the distribution of core velocities is Maxwellian, the crossing time of the main cloud is

$$t_{\rm CROSS} = \frac{D_{\rm O}}{\sqrt{3}\,\sigma_{\rm 1D,C}} = 0.8\,{\rm Myr}\,. \tag{2.7}$$

This gives the approximate time scale for cores to move across Ophiuchus. This can be compared to the typical free fall time of a core in Ophiuchus

$$t_{\rm FF} = \sqrt{\frac{\pi^2 \bar{R}^3}{8G\bar{M}}} = 0.05\,{\rm Myr}\,, \tag{2.8}$$

where $\bar{M} = 0.5\,{\rm M}_\odot$ is the mean value of $M_{\rm MAN98}$ and $\bar{R} = 3300\,{\rm AU}$ is the mean value of

$$R_{\rm MAN98} = \sqrt{{\rm FWHM_{maj}} \times {\rm FWHM_{min}}}\,. \tag{2.9}$$

As $t_{\rm CROSS}$ is more than an order of magnitude greater than $t_{\rm FF}$, this suggests that cores in Ophiuchus collapse before they interact.

We can provide a more refined analysis by calculating the mean free path of a core in Ophiuchus. To simplify this problem, we assume that all the cores are rigid, spherical 'billiard balls' which do not interact tidally. We also ignore any drag effects from the diffuse gas in which the core are embedded. If the cores are

where $\mu_i \equiv \log(M)_i$. As the probability density function of the CMF is likely to be roughly lognormal, we set

$$h = \left(\frac{4\hat{\sigma}^5}{3N}\right)^{\frac{1}{5}} \tag{2.6}$$

where $\hat{\sigma}$ is the standard deviation of $\log(M)_i$ (Silverman, 1998). This is a useful method of extracting large scale features from probability density functions which may be difficult to see in noisy histograms.

uniformly distributed throughout Ophiuchus, each core has a mean free path

$$\mathcal{L} = \frac{D_{\rm O}^3}{6NR_{\rm CS}^2}\,, \tag{2.10}$$

where $R_{\rm CS}$ is the radius of a core's cross sectional area. As each core has a physical size and will attract other cores through gravity, we have

$$R_{\rm CS} \approx 2\bar{R}\sqrt{\frac{2G\bar{M}}{v_{\rm R}^2\bar{R}} + 1}\,, \tag{2.11}$$

where $v_{\rm R}$ is the average relative velocity between cores, given by $v_{\rm R} = 4\sigma_{\rm 1D,C}/\sqrt{\pi}$. The core-core interaction time is therefore

$$t_{\rm I} = \frac{\mathcal{L}}{v_{\rm R}} \approx \frac{D_{\rm O}^3}{24Nv_{\rm R}\bar{R}^2\left(\frac{2G\bar{M}}{v_{\rm R}^2\bar{R}} + 1\right)} = 3.1\,{\rm Myr}\,. \tag{2.12}$$

We find that for the entire Ophiuchus main cloud, $t_{\rm I}$ is almost two orders of magnitude greater than $t_{\rm FF}$. However, the cores in Ophiuchus are sub-clustered into distinct regions, so it is more appropriate to apply this analysis on these individual regions. Table 2.3 gives the interaction and free fall time scales for different regions in Ophiuchus[4].

In Oph-A and Oph-B, the interaction time is at least an order of magnitude greater than the free fall time. This suggests that the large majority of cores in these regions collapse before they interact. In the region containing Oph-C, E and F, the interaction time is only 2.6 times greater than the free fall time. This means that it is likely that a significant fraction of cores interact before they collapse. However, as over three quarters of all the cores in Ophiuchus are in Oph-A and Oph-B, the assumption that *most* cores collapse before they interact is still likely to be valid.

2.4 Lognormal distribution

When we combine the MAN98 and ABMP07 core observations, there are 61 masses, 36 sizes and 27 velocity dispersions. However, there are only 20 cores which have all three of these measurements. To statistically model star formation in prestel-

[4]Note that this is an overly simple model that does not take into account protostellar cores lasting for more than a few free fall times. ABMP07 provide a similar analysis using values of $\bar{M} = 0.4\,{\rm M}_\odot$ and $\bar{R} = 2500\,{\rm AU}$ for cores in all regions of Ophiuchus. Their results are therefore different to ours.

Region	N	$\bar{M}$ ($M_\odot$)	$\bar{R}$ (AU)	$\sigma_{1D,C}$ ($km\,s^{-1}$)	v_R	D_O (pc)	$\mathcal{L}$	t_I (Myr)	t_{FF}	t_I/t_{FF}
Ophiuchus	61	0.51	3300	0.36	0.81	1.1	2.6	3.1	0.05	67
Oph-A	15	0.87	2300	0.19	0.43	0.28	0.10	0.24	0.02	11
Oph-B	22	0.32	2000	0.20	0.45	0.33	0.29	0.64	0.03	22
Oph-C,E,F	19	0.55	5400	0.39	0.88	0.44	0.22	0.25	0.10	2.6

Table 2.3: Core interaction parameters for regions in Ophiuchus. Column 1 gives the region; column 2 gives the number of cores in the region; column 3 gives mean core mass; column 4 gives the mean core size; column 5 gives the bulk radial velocity dispersion of cores; column 6 gives the average relative velocity between cores; column 7 gives the size of the region; column 8 gives the core mean free path; column 9 gives the core interaction time; column 10 gives the core free fall time; column 11 gives the core interaction time divided by the core free fall time.

lar cores, we need more than 20 initial conditions. Therefore, we use the data to calibrate a multivariate lognormal distribution of core properties in Ophiuchus. To within the errors of small number statistics, and modulo the assumption of a lognormal distribution, this will reproduce the observed properties *and* their correlations.

We draw $\boldsymbol{x} = (\log(M), \log(R), \log(\sigma_{NT}))$ from a lognormal distribution with probability density

$$P(\boldsymbol{x}) = \frac{1}{(2\pi)^{3/2}|\boldsymbol{\Sigma}|} \exp\left(-\frac{1}{2}(\boldsymbol{x}-\boldsymbol{\mu})^{\mathrm{T}}\boldsymbol{\Sigma}^{-1}(\boldsymbol{x}-\boldsymbol{\mu})\right), \tag{2.13}$$

where

$$\boldsymbol{\mu} \equiv \begin{pmatrix} \mu_M \\ \mu_R \\ \mu_{\sigma_{NT}} \end{pmatrix} \text{ and } \boldsymbol{\Sigma} \equiv \begin{pmatrix} \sigma_M^2 & \rho(M,R)\sigma_M\sigma_R & \rho(M,\sigma_{NT})\sigma_M\sigma_{\sigma_{NT}} \\ \rho(M,R)\sigma_M\sigma_R & \sigma_R^2 & \rho(R,\sigma_{NT})\sigma_R\sigma_{\sigma_{NT}} \\ \rho(M,\sigma_{NT})\sigma_M\sigma_{\sigma_{NT}} & \rho(R,\sigma_{NT})\sigma_R\sigma_{\sigma_{NT}} & \sigma_{\sigma_{NT}}^2 \end{pmatrix}^{5}. \tag{2.14}$$

Here, μ_{x_i} is the mean value of x_i and σ_{x_i} is its standard deviation. The values we use are given in Table 2.4 in the MAN98 and ABMP07 columns. The term $\rho(x_i, x_j)$ is Pearson's correlation coefficient and is defined by

$$\rho(x_i, x_j) = \frac{\sum_{k=1}^{N(x_i,x_j)} (x_{i,k} - \mu'_{x_i})(x_{j,k} - \mu'_{x_j})}{\sigma'_{x_i}\sigma'_{x_j}} \tag{2.15}$$

[5]To simplify the text we have omitted the logs from $\rho(x_i, x_j)$. For example, we represent $\rho(\log(M), \log(R))$ as $\rho(M, R)$.

Parameter		SNW08	SSGK06	MAN98	ABMP07
μ_M	$[\log(M/\mathrm{M}_\odot)]$	-0.44	-0.03	-0.57	-
σ_M	$[\log(M/\mathrm{M}_\odot)]$	0.59	0.43	0.43	-
μ_R	$[\log(R/\mathrm{AU})]$	3.15	3.76	3.11	-
σ_R	$[\log(R/\mathrm{AU})]$	0.10	0.19	0.27	-
$\mu_{\sigma_{\mathrm{NT}}}$	$[\log(\sigma_{\mathrm{NT}}/\mathrm{km\,s^{-1}})]$	-	-	-	-0.95
$\sigma_{\sigma_{\mathrm{NT}}}$	$[\log(\sigma_{\mathrm{NT}}/\mathrm{km\,s^{-1}})]$	-	-	-	0.2

Table 2.4: Arithmetic means and standard deviations of logged values of M, R and σ_{NT} from the SNW08, SSGK06, MAN98 and ABMP07 data.

Note that $N(x_i, x_j)$ is the number of cores that have a value for both x_i and x_j. With the MAN98 and AMBP07 data we have $N(M, R) = 36$, $N(M, \sigma_{\mathrm{NT}}) = 26$ and $N(R, \sigma_{\mathrm{NT}}) = 20$. The means and standard deviations μ'_{x_i}, μ'_{x_j}, σ'_{x_i} and σ'_{x_j} are calculated only from cores which have a measurement of both x_i and x_j .

From the data, we measure correlations

$$\boldsymbol{P} \equiv \begin{pmatrix} \rho(M,M) & \rho(M,R) & \rho(M,\sigma_{\mathrm{NT}}) \\ \rho(M,R) & \rho(R,R) & \rho(R,\sigma_{\mathrm{NT}}) \\ \rho(M,\sigma_{\mathrm{NT}}) & \rho(R,\sigma_{\mathrm{NT}}) & \rho(\sigma_{\mathrm{NT}},\sigma_{\mathrm{NT}}) \end{pmatrix} = \begin{pmatrix} 1 & 0.61 & 0.49 \\ 0.61 & 1 & 0.11 \\ 0.49 & 0.11 & 1 \end{pmatrix} . \tag{2.16}$$

As $\rho(x_i, x_j)$ is a measure of linear correlation between variates (where 0 implies no correlation and 1 implies absolute correlation), we see that $\log(M)$ and $\log(R)$ are moderately correlated, as are $\log(M)$ and $\log(\sigma_{\mathrm{NT}})$. There is little correlation between $\log(R)$ and $\log(\sigma_{\mathrm{NT}})$, however this may be due to the small number of data points. Figure 2.5 shows the probability density function $P(\boldsymbol{x})$ projected through all three of its dimensions. Superimposed are the observational data points as well as 100 data points drawn randomly from the distribution.

2.5 Summary

In this chapter we have stated the observations that we will use to create the initial conditions of SPH simulations of prestellar cores. Specifically, these are core mass and size measurements by MAN98 and non thermal velocity dispersions by ABMP07. There are other mass and size measurements by SNW08 and SSGK06, however these are not well matched with each other or with MAN98. We use the MAN98 measurements for convenience as they have largest number of velocity dispersions from ABMP07.

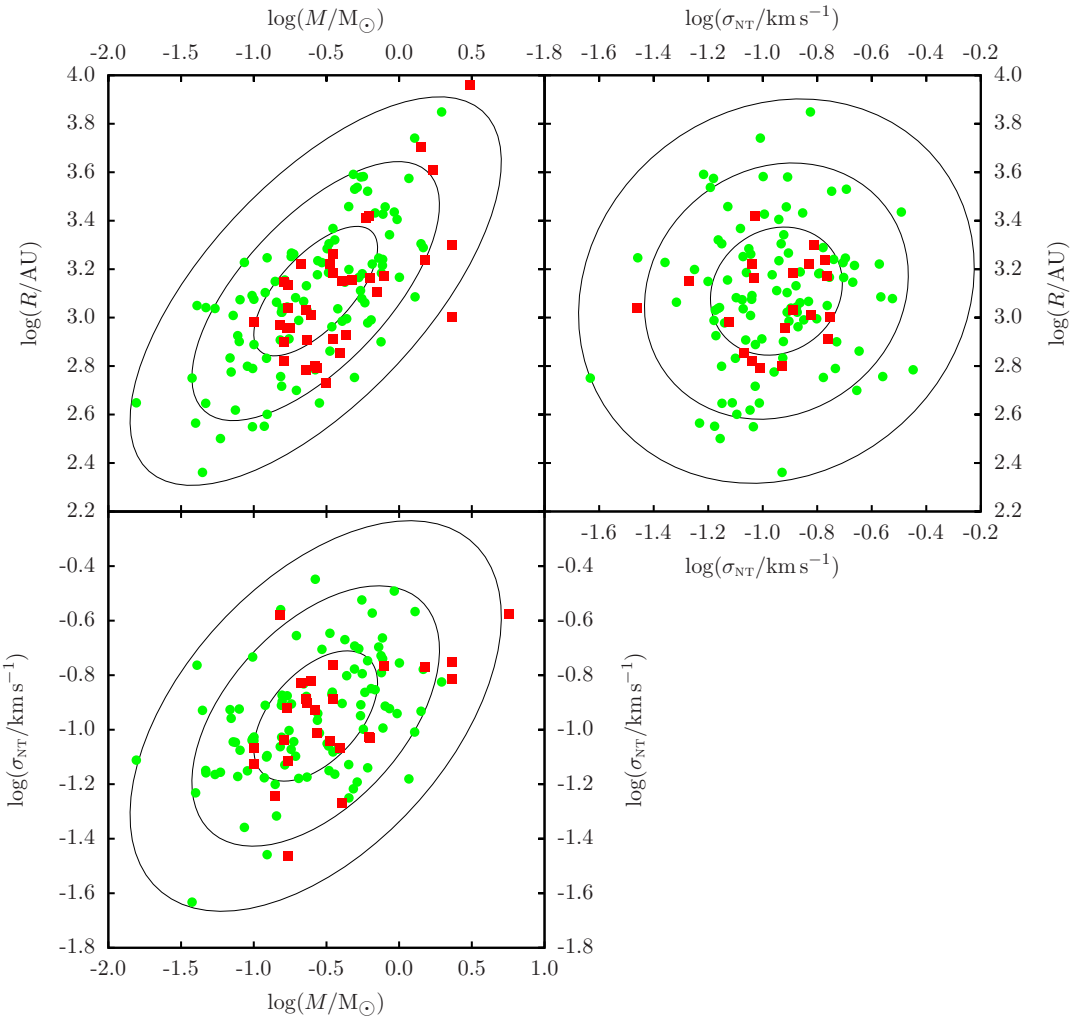

Figure 2.5: The multivariate lognormal distribution of $P(\boldsymbol{x})$ where $\boldsymbol{x} = (\log(M), \log(R), \log(\sigma_{\rm NT}))$. The top-left frame shows the distribution projected through the $\log(\sigma_{\rm NT})$ dimension; the top-right frame shows the distribution projected through the $\log(M)$ dimension; the bottom frame shows the distribution projected through the $\log(R)$ dimension. The concentric ellipses show the 1σ, 2σ and 3σ regions of the distribution. The red squares are the observational data by MAN98 and ABMP07 and the green circles are randomly drawn points from $P(\boldsymbol{x})$.

We have justified the assumption that most cores are likely to collapse in isolation. We show this using a simple model which compares the time taken for cores to interact with the free fall time of a typical core. We find that the core-core interaction time is at least an order of magnitude greater than the core free fall time for most cores in Ophiuchus.

We finally approximate the mass, size and velocity dispersion measurements from MAN98 and ABMP07 with a multivariate lognormal distribution. This should adequately reproduce the central region of the observed distribution. From this we can randomly draw any number of core masses, sizes and velocity dispersions.

Chapter 3

Intrinsic core shapes

In this chapter we address the problem of deducing the intrinsic shapes of cores from their observed aspect ratios. We propose four models based on the standard assumption that prestellar cores are intrinsically ellipsoidal.

The simplest, one-parameter model assumes that the axes of a prestellar core are drawn randomly from a log-normal distribution with zero mean and standard deviation $\tau_{\rm o}$. The more complex, two-parameter model assumes that the log-normal distribution has a finite mean, $\nu_{\rm o}$, defined so that $\nu_{\rm o} < 0$ means elongated (or filamentary) cores are favoured, and $\nu_{\rm o} > 0$ means flattened (or disc-like) cores are favoured. For further comparison we also invoke a second two-parameter model with two standard deviation parameters and a four-parameter model with two standard deviation and two mean parameters.

We apply a Bayesian analysis, where Markov chain Monte Carlo sampling is used to map out posterior probability density functions of the parameters, and models are compared using Bayes factors. We show that (i) the one-parameter model provides values of $\tau_{\rm o} \approx 0.57 \pm 0.07$ (to base e) and (ii) that despite an improved fit from some of the higher order models, it is difficult to justify the introduction of extra parameters.

3.1 Introduction

The shapes of prestellar cores projected onto the plane of the sky are not normally circular. Therefore we have a difficult inverse problem: while we can measure the and elongation of cores, there is no way of directly measuring their intrinsic shapes. Instead, we must deduce the likely distribution of intrinsic shapes through model fitting.

There have been several previous models developed to fit the observed aspect ra-

tios of cores, using both randomly oriented spheroids (e.g. Myers et al., 1991; Ryden, 1996) and randomly oriented ellipsoids (e.g. Goodwin et al., 2002; Jones and Basu, 2002; Tassis, 2007). These models invoke from two to four free parameters. Here we introduce a model in which the intrinsic shapes of prestellar cores are characterised by just one free parameter. Using Markov Chain Monte Carlo sampling (MCMC), we generate a probability density function (PDF) for this parameter, based on observations of the cores in Ophiuchus by Simpson et al. (2008) (SNW08), Stanke et al. (2006) (SSGK06) and Motte et al. (1998) (MAN98). We also define three more complex models by introducing additional parameters. These may provide a better fit, but the probability density of a specific set of parameters incurrs a penalty from being spread over extra dimensions.

In Section 3.2 we introduce each of the models, and explain how we derive projected shapes. In Section 3.3 we describe how we use Bayesian analysis to identify the best-fit model parameters, and the best models, using the observational data. In Section 8 we present and discuss the results, and in Section 3.5 we summarize our conclusions.

3.2 Modelling the shapes of cores

We follow the convention of approximating core shapes with ellipsoids having semi-axes A, B and C, where $A \geq B \geq C$. Furthermore, we assume that there is no relationship between the projected size and intrinsic shape of a prestellar core.

3.2.1 Model M1, one free parameter (τ_{o})

For the first model **M1**, we generate a family of core shapes with only one free parameter: τ_{o}. Each individual shape is an ellipsoid with semi-axes

$$\begin{aligned} A &= 1\,, \\ B &= \exp(\tau_{\mathrm{o}}\mathcal{G}_{\mathrm{B}})\,, \\ C &= \exp(\tau_{\mathrm{o}}\mathcal{G}_{\mathrm{C}})\,. \end{aligned} \tag{3.1}$$

Here – and in all further models – $\mathcal{G}_{\mathrm{B}}$ and $\mathcal{G}_{\mathrm{C}}$ are random numbers drawn from a Gaussian distribution with zero mean and unit standard deviation. Once the semi-axes of a core have been generated, they are re-ordered so that $A \geq B \geq C$ and normalised so that $A = 1$.

Increasing τ_{o} increases the likelihood that the axes of a core have very disparate sizes, and hence the likelihood that the projected shape of the core has a small

aspect ratio, q. Note that while this model *can* produce oblate cores (i.e. $B \approx A$ and $C < B$) and prolate cores (i.e. $B < A$ and $C \approx B$), it *does not* include a preference towards either shape. Most of the individual shapes are triaxial (i.e. $A \not\approx B \not\approx C$).

The core shapes from this model are likely to occur in the presence of turbulence. Statistically isotropic turbulence will shock gas randomly along different directions, producing randomly drawn intrinsic aspect ratios. Furthermore, Lin et al. (1965) show that an ellipsoidal core of gas undergoing free fall collapses fastest along its shortest axis. This would enhance any disparities in the intrinsic core aspect ratios provided by turbulence.

3.2.2 Model M2a, two free parameters $(\nu_{\mathbf{o}}, \tau_{\mathbf{o}})$

For the second model **M2a**, we generate a family of core shapes using two free parameters: $\nu_{\rm o}$, $\tau_{\rm o}$. Each ellipsoid has semi-axes

$$\begin{aligned} A &= 1\,, \\ B &= \exp(\nu_{\rm o} + \tau_{\rm o}\mathcal{G}_{\rm B})\,, \\ C &= \exp(\nu_{\rm o} + \tau_{\rm o}\mathcal{G}_{\rm C})\,. \end{aligned} \tag{3.2}$$

Unlike **M1**, we explicitly include the possibilty of a preference for oblate or prolate cores in **M2a**. When $\nu_{\rm o} \gtrsim \tau_{\rm o}$, cores tend to be oblate and when $\nu_{\rm o} \lesssim -\tau_{\rm o}$, cores tend to be prolate. When $|\nu_{\rm o}| \lesssim \tau_{\rm o}$, cores tend to be triaxial.

Roughly axisymmetric core shapes such as those provided by this model imply that the cores are in some form of equilibrium. Oblate core shapes may occur if the self-gravity of a core is balanced by rotation (e.g. Kiguchi et al., 1987) or restricted by a poloidal magnetic field (e.g. Mouschovias, 1976). It is also possible that prolate cores may be the result of toroidal or helical magnetic fields (e.g. Fiege and Pudritz, 2000; Tomisaka, 1991).

3.2.3 Model M2b, two free parameters $(\tau_{\mathbf{b}}, \tau_{\mathbf{c}})$

For the third model **M2b**, we generate a family of core shapes with two free parameters: $\tau_{\rm B}$ and $\tau_{\rm C}$. Each ellipsoid has semi-axes

$$\begin{aligned} A &= 1\,, \\ B &= \exp(\tau_{\rm B}\mathcal{G}_{\rm B})\,, \\ C &= \exp(\tau_{\rm C}\mathcal{G}_{\rm C})\,. \end{aligned} \tag{3.3}$$

With this model, if $\tau_{\rm B} \approx 0$ and $\tau_{\rm C} \gg \tau_{\rm B}$, we produce an ensemble of oblate and prolate cores. While there is no strong physical justification for adopting this model, it provides a second relatively obvious way of generating a two-parameter family of ellipsoidal shapes.

3.2.4 Model M4, four free parameters $(\nu_{\rm B}, \tau_{\rm B}, \nu_{\rm C}, \tau_{\rm C})$

For the fourth and final model **M4**, we generate a family of core shapes with four free parameters: $\nu_{\rm B}$, $\nu_{\rm C}$, $\tau_{\rm B}$ and $\tau_{\rm C}$. Each ellipsoid has semi-axes

$$\begin{aligned} A &= 1\,, \\ B &= \exp(\nu_{\rm B} + \tau_{\rm B}\mathcal{G}_{\rm B})\,, \\ C &= \exp(\nu_{\rm C} + \tau_{\rm C}\mathcal{G}_{\rm C})\,. \end{aligned} \tag{3.4}$$

With this model, if $|\nu_{\rm B}| > \tau_{\rm B}$ and $|\nu_{\rm C}| > \tau_{\rm C}$ we produce cores with roughly the same triaxial shape. This shape will be much more varied between cores if $|\nu_{\rm B}| \lesssim \tau_{\rm B}$ or $|\nu_{\rm C}| \lesssim \tau_{\rm C}$.

Similar to model **M1**, this model implies that the core shapes have been perturbed by turbulence. The parameters of these models can also be compared to results by Goodwin et al. (2002) and Jones et al. (2001). However, we note that it is difficult to imagine why turbulence would produce a population of cores all with roughly the same shape.

3.2.5 Projecting an arbitrarily oriented ellipsoid

We define a Cartesian co-ordinate system in which the x-axis is aligned along A, the y-axis along B, and the z-axis along C. To observe this core from an arbitrary direction, given by polar angles (θ, ϕ), we set

$$\theta = \cos^{-1}(2\mathcal{R}_\theta - 1)\,, \tag{3.5}$$

$$\phi = 2\pi\mathcal{R}_\phi\,, \tag{3.6}$$

where $\mathcal{R}_\theta$ and $\mathcal{R}_\phi$ are randomly drawn from a uniform distribution on the interval $(0, 1)$. The aspect ratio of the core is then given by

$$q = \sqrt{\frac{\alpha + \gamma - \sqrt{(\alpha-\gamma)^2 + \beta^2}}{\alpha + \gamma + \sqrt{(\alpha-\gamma)^2 + \beta^2}}} \tag{3.7}$$

where

$$\alpha = (A^2\cos^2(\phi) + B^2\sin^2(\phi))\cos^2(\theta) + C^2\sin^2(\theta), \tag{3.8}$$

$$\beta = (B^2 - A^2)\cos(\theta)\sin(2\phi), \tag{3.9}$$

$$\gamma = A^2\sin^2(\phi) + B^2\cos^2(\phi) \tag{3.10}$$

(see Binney, 1985).

3.3 Bayesian analysis

We use Bayesian analysis to determine the best-fit parameters of the different models, and to quantify their relative strengths. When comparing model $\mathbf{M}$ with parameters $\mathbf{x} \equiv (x_1, x_2, ...)$ against observational data $\mathbf{D}$, Bayes' theorem states that

$$P(\mathbf{x}|\mathbf{M},\mathbf{D}) = \frac{P(\mathbf{D}|\mathbf{M},\mathbf{x})P(\mathbf{x}|\mathbf{M})}{P(\mathbf{D}|\mathbf{M})}\,. \tag{3.11}$$

Here $P(\mathbf{x}|\mathbf{M},\mathbf{D})$ is the posterior probability of $\mathbf{x}$ given $\mathbf{D}$, $P(\mathbf{D}|\mathbf{M},\mathbf{x})$ is the likelihood of $\mathbf{D}$ given $\mathbf{x}$, $P(\mathbf{x}|\mathbf{M})$ is the prior PDF of $\mathbf{x}$ and $P(\mathbf{D}|\mathbf{M})$ is the marginal likelihood over all values of $\mathbf{x}$, i.e.

$$P(\mathbf{D}|\mathbf{M}) = \int_{\mathbf{x}} \mathbf{P}(\mathbf{D}|\mathbf{M},\mathbf{x})\mathbf{P}(\mathbf{x}|\mathbf{M})\,\mathrm{d}\mathbf{x}\,. \tag{3.12}$$

As $P(\mathbf{D}|\mathbf{M})$ is a constant, Equation (3.11) simplifies to

$$P(\mathbf{x}|\mathbf{M},\mathbf{D}) \propto \mathbf{P}(\mathbf{D}|\mathbf{M},\mathbf{x})\mathbf{P}(\mathbf{x}|\mathbf{M})\,, \tag{3.13}$$

where any generated posterior PDFs can be normalized to unity, post analysis.

3.3.1 Prior PDF

When generating prior PDFs for the model parameters $\mathbf{x}$ we assume that $P(\mathbf{x}|\mathbf{M})$ is finite and uniform within given limits, and zero outside them. This is to say, within credible limits, we impose no *a priori* preference for any specific $\mathbf{x}$.

For **M1**, the single parameter $\tau_{\rm o}$ must be able to reproduce the maximum and minimum observed aspect ratios in the data, viz. $q_{\rm MAX} \simeq 1$ and $q_{\rm MIN} \simeq 0.3$ (over all three data sets, there are only two cores with $q < 0.3$). Since the majority of aspect ratios delivered by **M1** satisfy $q \gtrsim \exp(-\tau_{\rm o})$, we set $-\ln(q_{\rm MAX}) \leq \tau_{\rm o} \leq -\ln(q_{\rm MIN})$, i.e. $0 \leq \tau_{\rm o} \leq 1.2$.

For **M2a** we set the range of $\nu_{\rm O}$ to $-1.2 \leq \nu_{\rm O} \leq 1.2$ so that a purely oblate or prolate population (i.e. one with $\tau_{\rm O} = 0$) could reproduce the observed aspect ratios. We then assign $\tau_{\rm O}$ the same range as in **M1**.

For both **M2b** and **M4** we assign $\tau_{\rm B}$ and $\tau_{\rm C}$ the same range as $\tau_{\rm O}$ in **M1**. For **M4** we assign $\nu_{\rm B}$ and $\nu_{\rm C}$ the same range as $\nu_{\rm O}$ in **M2a**.

With these ranges, the normalised prior PDFs are:

$$P(\tau_{\rm O}|\mathbf{M1}) = \begin{cases} \frac{1}{(1.2)} & \text{if } 0 \leq \tau_{\rm O} \leq 1.2, \\ 0 & \text{otherwise;} \end{cases}$$

$$P(\nu_{\rm O}, \tau_{\rm O}|\mathbf{M2a}) = \begin{cases} \frac{1}{2(1.2)^2} & \text{if } -1.2 \leq \nu_{\rm O} \leq 1.2 \\ & \text{and } 0 \leq \tau_{\rm O} \leq 1.2, \\ 0 & \text{otherwise;} \end{cases}$$

$$P(\tau_{\rm B}, \tau_{\rm C}|\mathbf{M2b}) = \begin{cases} \frac{1}{(1.2)^2} & \text{if } 0 \leq \tau_{\rm B} \leq 1.2 \\ & \text{and } 0 \leq \tau_{\rm C} \leq 1.2, \\ 0 & \text{otherwise;} \end{cases}$$

$$P(\nu_{\rm B}, \nu_{\rm C}, \tau_{\rm B}, \tau_{\rm C}|\mathbf{M_4}) = \begin{cases} \frac{1}{4(1.2)^4} & \text{if } -1.2 \leq \nu_{\rm B} \leq 1.2 \\ & \text{and } -1.2 \leq \nu_{\rm C} \leq 1.2 \\ & \text{and } 0 \leq \tau_{\rm B} \leq 1.2 \\ & \text{and } 0 \leq \tau_{\rm C} \leq 1.2, \\ 0 & \text{otherwise}\,. \end{cases} \tag{3.14}$$

Note that these prior PDFs *will not* affect the inferences on specific parameter values as long as the posterior distribution of $\mathbf{x}$ is within these credible limits. These priors *will* affect the strength of specific models, discussed further in Section 3.3.3.

3.3.2 Markov chain Monte Carlo sampling

For each observational data set, $\mathbf{D}$, we generate a histogram of aspect ratios. The histogram has ten bins ($k = 1$ to 10), evenly spaced between $q = 0$ and $q = 1$, and O_k is the number of observed cores in bin k.

For a given model, $\mathbf{M}$, and a given choice of the associated free parameters, $\mathbf{x_i}$, we generate 10^4 ellipsoids, and view each one from an arbitrary direction to determine its aspect ratio, q, as described in Section 3.2. The resulting q-values are then used to construct an equivalent histogram of expectation values, E_j, ($j = 1$ to 10), normalised so that $\sum_j \{E_j\} = \sum_j \{O_j\}$. The likelihood of the observational data, $\mathbf{D}$,

being reproduced by $\mathbf{M}, \mathbf{x_i}$ is then

$$P(\mathbf{D}|\mathbf{M}, \mathbf{x_i}) = \exp\left\{ -\sum_{j=1}^{j=10} \frac{(O_j - E_j)^2}{2O_j} \right\} . \tag{3.15}$$

We have assumed purely Poisson errors on the counts in each bin O_j because error estimates for individual observed q-values are not available. Bins that have less than five counts are pooled together so that the Gaussian approximation to Poisson errors is valid.

To build a Markov Chain, we consider the observational values, O_k, from a particular data set, $\mathbf{D}$, and we invoke a particular model, $\mathbf{M}$. We pick a set of model parameters ($\mathbf{x_0}$) in the middle of the ranges defined in Section 3.3.1, and compute $P(\mathbf{D}|\mathbf{M}, \mathbf{x_0})$, as described in the preceding paragraph. We then build the chain by stepping from one set of model parameters to another, $\mathbf{x_0} \rightarrow \mathbf{x_1} \rightarrow \mathbf{x_2} \rightarrow \mathbf{x_3}$.... Each step, $\Delta\mathbf{x} = \mathbf{x_{i+1}} - \mathbf{x_i}$ is drawn randomly from a Gaussian distribution centred on zero. The step is only made if

$$\frac{P(\mathbf{D}|\mathbf{M}, \mathbf{x_{i+1}})}{P(\mathbf{D}|\mathbf{M}, \mathbf{x_i})} \geq \mathcal{R}_{\text{STEP}} , \tag{3.16}$$

where $\mathcal{R}_{\text{STEP}}$ is a random number from a uniform distribution on the interval (0,1). Otherwise the step is rejected and a new step is drawn; this ensures that the points on the chain tend to concentrate in regions of high probability. The coefficients regulating the mean step size should be adjusted so that roughly half the steps are rejected. The first 10^3 points on the chain are discarded, to remove any memory of the starting point. The subsequent 5×10^5 points are used to identify the best-fit parameters and their uncertainties.

We have built a Markov Chain for each possible combination of the four models and the three data sets. The points on the chain are then used to determine the posterior PDFs of the model parameters. The results are presented in Figures 3.1, 3.2, 3.3 and 3.4. The best fits obtained with **M1** and **M2a** are compared with the observations in Figures 3.5 and 3.6.

3.3.3 Model selection

Bayesian analysis can also be used to compare different models. Given a list of competing models, $\mathbf{M_1}, \mathbf{M_2}, \ldots, \mathbf{M_n}$, the probability of a particular model, $\mathbf{M_k}$, is

$$P(\mathbf{M_k}|\mathbf{D}) = \frac{\mathbf{P(D|M_k)P(M_k)}}{\mathbf{P(D)}} , \tag{3.17}$$

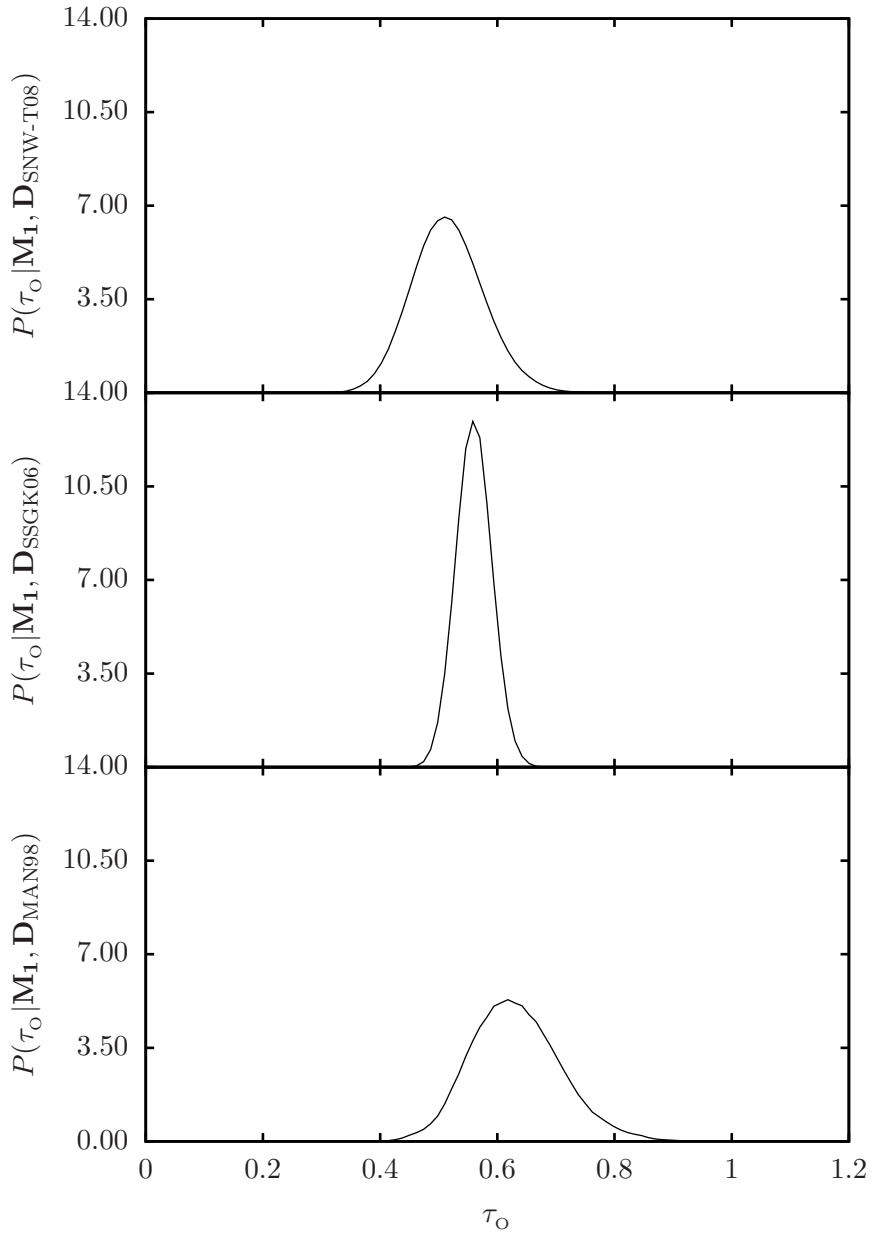

Figure 3.1: Posterior PDFs for $\tau_{\rm O}$ in **M1**, from the SNW08, SSGK06 and MAN98 data.

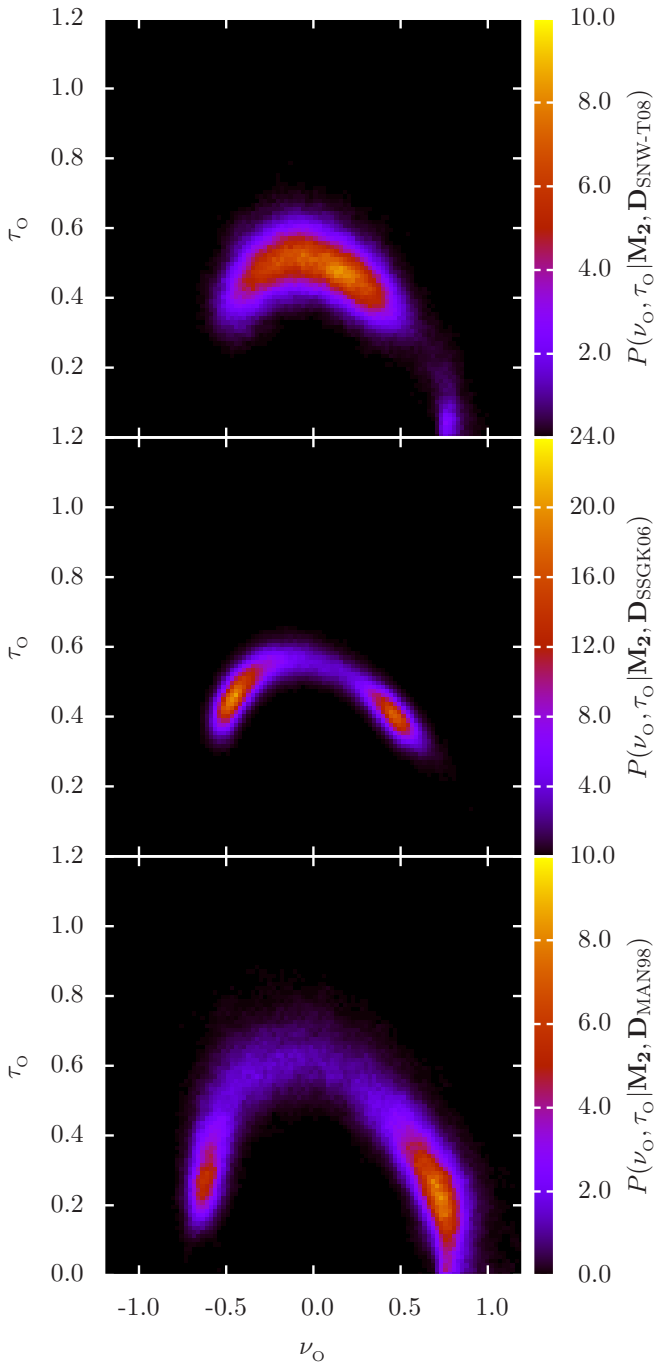

Figure 3.2: Posterior PDFs for ν_0 and τ_0 in **M2a**, from the SNW08, SSGK06 and MAN98 data.

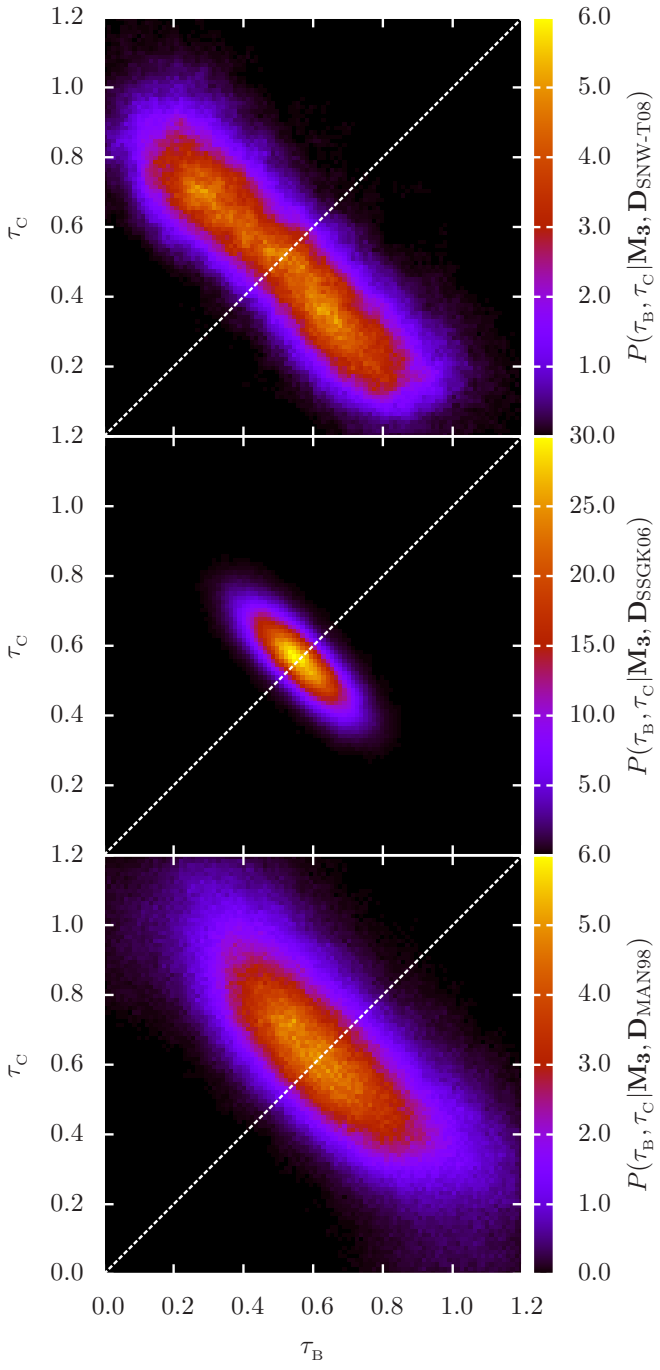

Figure 3.3: Posterior PDFs for τ_B and τ_C in **M2b**, from the SNW08, SSGK06 and MAN98 data. The white dashed line represents $\tau_B = \tau_C$, about which the distribution should be symmetric.

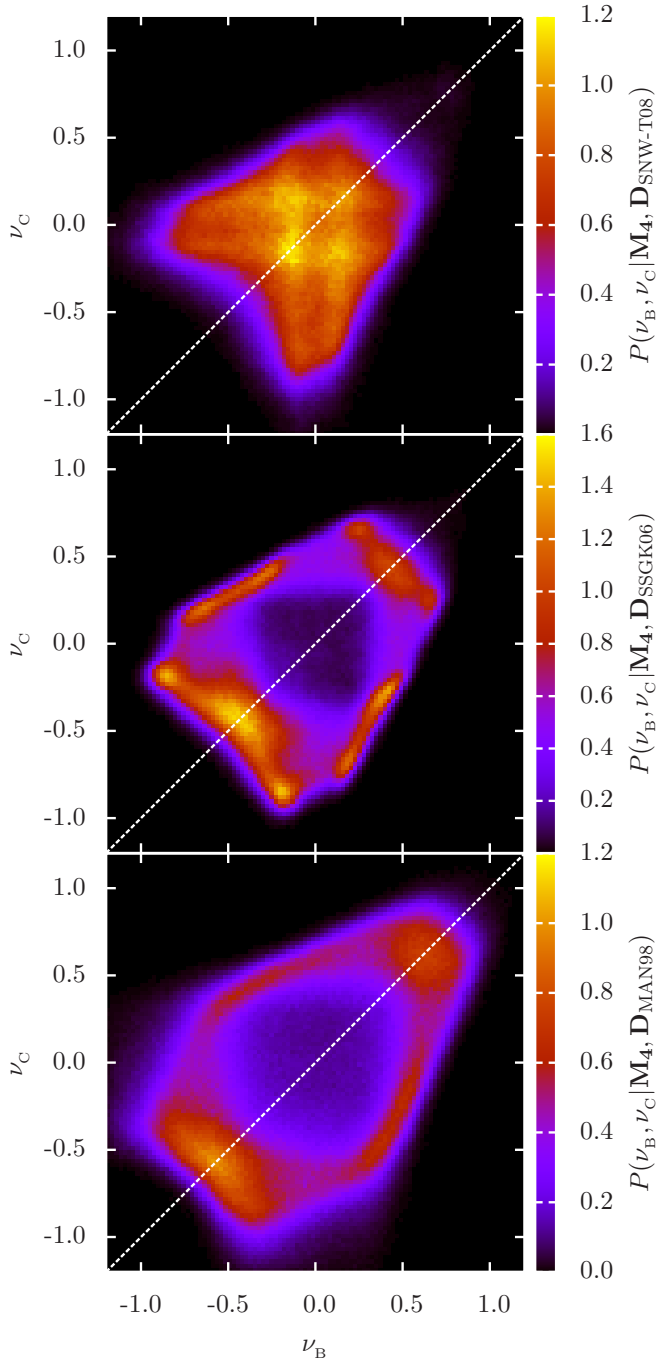

Figure 3.4: Posterior PDFs for ν_B, ν_C in **M4**, from the SNW08, SSGK06 and MAN98 data. τ_B and τ_C have been marginalized out, i.e. $P(\nu_B, \nu_C|\mathbf{M4}, \mathbf{D}) = \iint P(\nu_B, \nu_C, \tau_B, \tau_C|\mathbf{M4}, \mathbf{D})\, d\tau_B\, d\tau_C$. The white dashed line represents $\nu_B = \nu_C$, about which the distribution should be symmetric.

where

$$P(\mathbf{D}) = \sum_{\mathbf{k=1}}^{\mathbf{k=n}} \mathbf{P(D|M_k)P(M_k)}\,. \tag{3.18}$$

To calculate $P(\mathbf{D}|\mathbf{M_k})$ we must marginalise each model's likelihood over its associated parameter space (see Eqn. 3.12). We evaluate this integral by organising the points on the associated Markov Chain into a balanced binary tree (Weinberg, 2009). This has the effect of dividing the parameter space into cells, each of which contains a single point. Each point, $\mathbf{x_i}$, now has a likelihood (see Eqn. 3.15) and a volume of parameter space, $\delta V_\mathbf{i}$ equal to the volume of the cell it occupies. Hence the marginalised likelihood is approximated by

$$P(\mathbf{D}|\mathbf{M_k}) \approx \frac{1}{V_k} \sum_{\mathbf{i}=1}^{\mathbf{i}=N} P(\mathbf{D}|\mathbf{M_k}, \mathbf{x_i})\, \delta V_\mathbf{i}\,. \tag{3.19}$$

Here N is the number of points on the Markov Chain and V_k is the total volume of parameter space associated with model $\mathbf{M_k}$. As MCMC sampling is most noisy around the edges of the distribution, we omit from the summation any cells that extend to the boundaries of the parameter space. These regions are under sampled and have disproportionately large cells; including them generally overestimates $P(\mathbf{D}|\mathbf{M_k})$.

Note that $1/V_k$ is the probability density of the prior PDFs given in Equation (3.14). This term decreases exponentially with the number of free parameters in each model. So, for example, model **M4** would need to produce a much better fit to the data than **M1** to give $P(\mathbf{D}|\mathbf{M4}) > P(\mathbf{D}|\mathbf{M1})$.

The relative likelihood of one model, $\mathbf{k}$, with respect to another, $\mathbf{k'}$, is quantified by the Bayes factor

$$K_{\mathbf{kk'}} = \frac{P(\mathbf{M_k}|\mathbf{D})}{P(\mathbf{M_{k'}}|\mathbf{D})} = \frac{P(\mathbf{D}|\mathbf{M_k})\mathbf{P(M_k)}}{P(\mathbf{D}|\mathbf{M_{k'}})\mathbf{P(M_{k'})}}\,. \tag{3.20}$$

Given that we have no *a priori* preference for either model, i.e. $P(\mathbf{M_k}) = P(\mathbf{M_{k'}})$, Equation (3.20) reduces to the ratio of the marginalised likelihoods. Bayes factors quantifying the relative performance of the different models are presented in Table 3.1 .

3.4 Results

3.4.1 Parameter estimation for M1

Figure 3.1 shows the posterior PDFs for $\tau_{\rm O}$ in **M1**, based on the different data sets. Since the PDFs are all unimodal and not overly skewed, we can calculate means and standard deviations, viz. $\tau_{\rm O}=0.51\pm0.06$ (SNW−T09), 0.56 ± 0.03 (SSGK06), 0.63 ± 0.08 (MAN98). These values can be combined to give $\tau_{\rm O}=0.57\pm0.07$, i.e. the principal axes of a core typically differ by a factor of order $\exp(\tau_{\rm O})\approx1.7$.

Figure 3.5 compares the observed distributions of aspect ratio from the different data sets with the best fits from **M1**. **M1** fits the SSGK06 data (which, with 111 cores, has the least noisy statistics) well. The fits to the SNW08 data (52 cores) and the MAN98 data (35 cores) are less good. For example, the MAN98 data hints at a sharp peak between $q=0.5$ and $q=0.6$ which **M1** is unable to reproduce; however, this may just be the product of small-number statistics.

3.4.2 Parameter estimation for M2a

Figure 3.2 shows the posterior PDFs of $\nu_{\rm O}$ and $\tau_{\rm O}$ in **M2a**, based on the different data sets. We recall that $\nu_{\rm O}$ determines whether cores have a tendency to be filamentary ($\nu_{\rm O}<0$) or disc-like ($\nu_{\rm O}>0$). For all three data sets there is a degeneracy, because the intrinsic asymmetry of the cores is promoted both by increasing $\tau_{\rm O}$, and by increasing $|\nu_{\rm O}|$. Consequently solutions with reduced $\tau_{\rm O}$ and increased $|\nu_{\rm O}|$ have high probability. Indeed, for the SSGK06 and MAN98 data sets these are actually the preferred solutions. However, in neither case is there a clear preference for filamentary over disc-like cores, or *vice versa*.

Figure 3.6 compares the observed distributions of aspect ratio with the best fits from **M2a**. **M2a** delivers a markedly better fit – than **M1** – to the SSGK06 and MAN98 data sets, irrespective of whether we use the filamentary or disc-like parameters. However, the best fit to the SNW08 data set is not much better than with **M1**.

3.4.3 Parameter estimation for M2b

Figure 3.3 shows the posterior PDFs of $\tau_{\rm B}$ and $\tau_{\rm C}$ in **M2b**, based on the different data sets. For the SSGK06 data we find a peak at $\tau_{\rm B}\simeq\tau_{\rm C}\simeq0.55$, and for the MAN98 data at $\tau_{\rm B}\simeq\tau_{\rm C}\simeq0.60$. For the SNW08 data, the distribution of $\tau_{\rm B}$ and $\tau_{\rm C}$ is somewhat broader, but nowhere does it exceed that for $\tau_{\rm B}\simeq\tau_{\rm C}\simeq0.50$. Thus, for

all three data sets, the two parameters of **M2b** do not provide a better fit than the single parameter of **M1**.

3.4.4 Parameter estimation for M4

Figure 3.4 shows the posterior PDFs of $\nu_{\rm B}$ and $\nu_{\rm C}$ in **M4**, based on the different data sets; for simplicity, we have marginalized $\tau_{\rm B}$ and $\tau_{\rm C}$ out of the PDFs. For all three data sets, the highest probabilities lie on the line $\nu_{\rm B} \simeq \nu_{\rm C}$, which suggests that **M4** is unable to improve on **M2a**. There are also regions of moderately high probability where $\nu_{\rm B} \neq \nu_{\rm C}$, but these are outweighed by the regions where $\nu_{\rm B} \simeq \nu_{\rm C}$, and there is no hint of a preference for filamentary over disc-like shapes, or *vice versa*.

3.4.5 Model selection

We quantify the quality of the different models, for the different data sets, by calculating Bayes factors, $K_{\mathbf{k}\mathbf{k}'}$, as described in Section 3.3.3. The results are presented in Table 3.1, where $K > 1$ indicates a preference for the model denoted in the column header, and $K < 1$ indicates a preference for the model in the row label. Jeffreys (1961) suggests the following qualitative interpretation for different values of $K_{\mathbf{k}\mathbf{k}'}$:

$$
\begin{aligned}
K_{\mathbf{k}\mathbf{k}'} &\leq 1/10 && \text{Strongly supports } \mathbf{M}_{\mathbf{k}'}\,, \\
1/10 < K_{\mathbf{k}\mathbf{k}'} &\leq 1/3 && \text{Moderately supports } \mathbf{M}_{\mathbf{k}'}\,, \\
1/3 < K_{\mathbf{k}\mathbf{k}'} &< 1 && \text{Weakly supports } \mathbf{M}_{\mathbf{k}'}\,, \\
K_{\mathbf{k}\mathbf{k}'} &= 1 && \text{No preference}\,, \\
1 < K_{\mathbf{k}\mathbf{k}'} &< 3 && \text{Weakly supports } \mathbf{M}_{\mathbf{k}}\,, \\
3 \leq K_{\mathbf{k}\mathbf{k}'} &< 10 && \text{Moderately supports } \mathbf{M}_{\mathbf{k}}\,, \\
K_{\mathbf{k}\mathbf{k}'} &\geq 10 && \text{Strongly supports } \mathbf{M}_{\mathbf{k}}\,;
\end{aligned}
$$

we stress that these categories are only intended to be indicative.

The SNW08 data are much better fitted by **M1** or **M2b**, than by **M2a** or **M4**; there is little to chose between **M1** and **M2b**. Conversely, the SSGK06 and MAN98 data sets are both fitted best by **M2a**, with **M1** also giving a good fit, and **M2b** and **M4** giving relatively poor fits. To combine the data sets, we have simply taken the products of their individual Bayes factors, and these are given in the last panel of Table 3.1. These values suggest that **M1** is the best model. **M2a** is almost as good, and should remain in the reckoning against the day when sufficient data is available to distinguish between filamentary and disc-like cores.

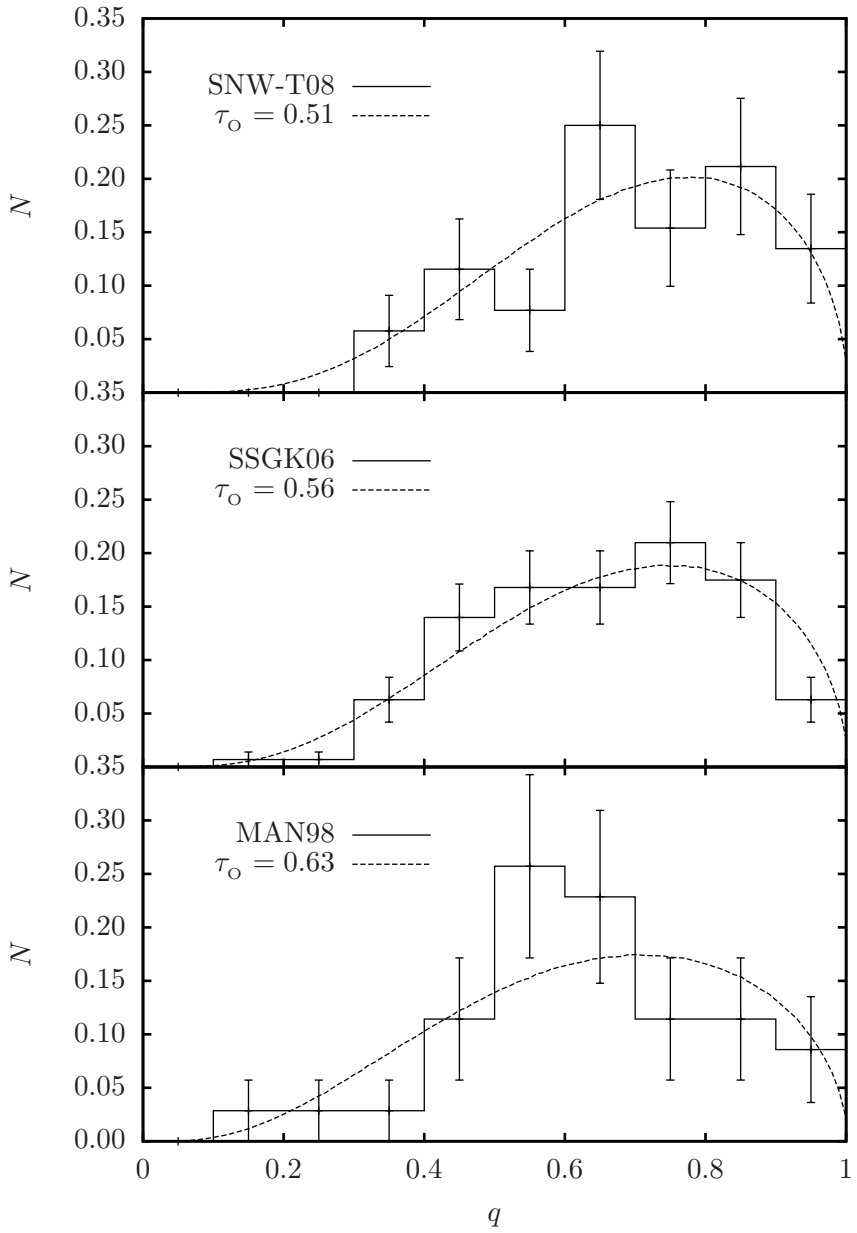

Figure 3.5: The histograms represent the distributions of aspect ratio obtained by SSGK06 (top), MAN98 (middle) and SNW08 (bottom), with $\sqrt{N}$ errors. The dashed lines represent the best fits obtained with **M1**.

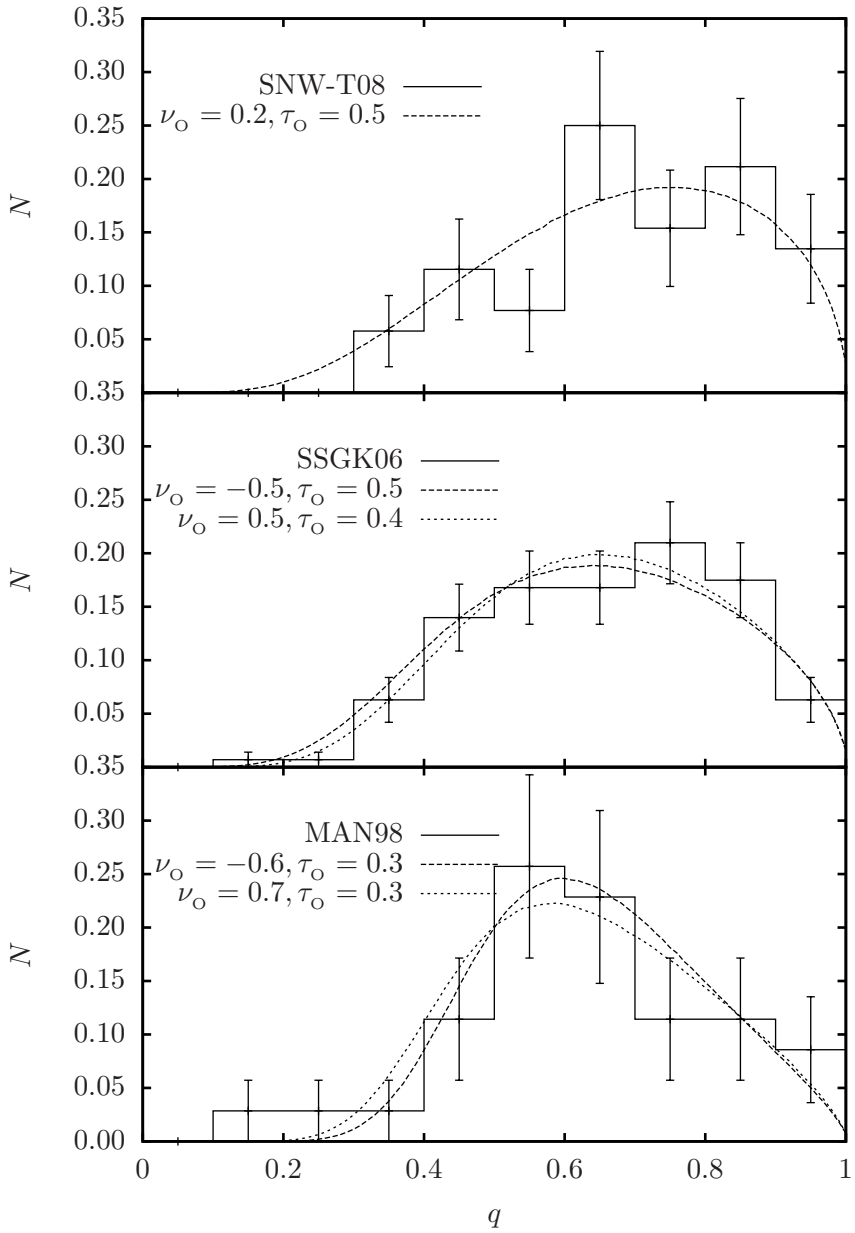

Figure 3.6: As Figure 3.5, but for **M2a**.

SNW08				
	M1	**M2a**	**M2b**	**M4**
M1	1	0.31	1.02	0.08
M2a	3.20	1	3.27	0.26
M2b	0.98	0.31	1	0.08
M4	12.11	3.78	12.36	1
SSGK06				
	M1	**M2a**	**M2b**	**M4**
M1	1	1.80	0.31	0.48
M2a	0.56	1	0.17	0.27
M2b	3.23	5.80	1	1.54
M4	2.10	3.76	0.65	1
MAN98				
	M1	**M2a**	**M2b**	**M4**
M1	1	1.76	0.75	0.60
M2a	0.57	1	0.43	0.34
M2b	1.33	2.34	1	0.80
M4	1.67	2.93	1.25	1
COMBINED				
	M1	**M2a**	**M2b**	**M4**
M1	1	0.98	0.24	0.023
M2a	1.02	1	0.24	0.024
M2b	4.21	4.21	1	0.10
M4	42.5	41.6	10.0	1

Table 3.1: Bayes factors, $K = P(\mathbf{M}_{\rm COLUMN}|\mathbf{D})/P(\mathbf{M}_{\rm ROW}|\mathbf{D})$, calculated using Eqn. 3.20. The first three panels give values for the individual data sets, and the fourth panel gives their product.

Since our analysis has not included the errors on individual data points (they are not available), the Poisson errors in Figures 3.5 and 3.6, and in Eqn. (3.15), should be larger. This would broaden the posterior PDFs for all models, but the effect would tend to be larger for models with more free parameters, in the sense that the probability would be smeared over more dimensions, and therefore their marginal likelihoods would be reduced more. Since we have already concluded that **M1** performs best, we infer that this conclusion would be reinforced if observational errors were included.

3.5 Summary

We have used Bayesian analysis to infer the intrinsic shapes of prestellar cores in Ophiuchus. We find that the observational data are well fitted with a one-parameter

model, **M1**, in which cores are triaxial ellipsoids with axes chosen from a log-normal distribution having zero mean and standard deviation $\tau_{\rm o} \simeq 0.57 \pm 0.07$. The two-parameter model **M2b** does not sufficiently improve the fit to justify its adoption, and the four-parameter model, **M4** is completely unjustified.

There is some evidence to suggest that model **M2a** performs as well as **M1**. However the strong degeneracy between mostly disc-like and mostly filamentary cores makes it difficult to determine which shape is more likely. Indeed, it may be the case that cores in Ophiuchus are a mixture of both these shapes. However, the projected distributions of q for filamentary and disc like cores are very similar, so the ratio of one shape to the other might be very difficult to infer from observations. Furthermore, the addition of the extra free parameter would decrease the statistical robustness of the model.

As **M1** is a strong model with an unambiguous result, we use it to define the initial shapes of prestellar cores in this thesis. By setting $\tau_{\rm o} = 0.6$, we can randomly draw intrinsic aspect ratios Q_B and Q_C, and use sizes drawn from observations to fully define the ellipsoidal shapes of cores.

Chapter 4

Internal structure

In the previous two chapters, we have stated how we generate the masses, sizes, internal velocity dispersions and intrinsic shapes for model prestellar cores. These core properties are closely informed by observations of cores in Ophiuchus. In this chapter we define and justify the assumptions made on the cores' radial density profiles and velocity fields.

We characterise the radial density profile of the core as that of a critical Bonnor-Ebert sphere and we model the velocity field as a mixture of small-scale turbulence and large scale rotational and radial motions. For simplicity and clarity, throughout this chapter we assume that cores are spherically symmetric. The procedure for creating triaxial prestellar cores is explained in Chapter 7.

4.1 The density profile

Observations show that the density profiles of some dense cores are well matched with those of critical Bonner-Ebert (BE) spheres (e.g. Alves et al., 2001; Harvey et al., 2001; Lada et al., 2008). A BE sphere (Bonnor, 1956) is a pressure contained self-gravitating sphere of isothermal gas. As described in Section 4.1, the density profile of a BE sphere is determined only by its dimensionless radius $\xi_{\rm B}$. A critical BE sphere has $\xi_{\rm B} = \xi_{\rm CRIT} = 6.451$ and is marginally stable against gravitational collapse so long as the gas pressure at its boundary is matched by an equal external pressure. BE spheres with $\xi_{\rm B} < \xi_{\rm CRIT}$ are stable against gravitational collapse and BE spheres with $\xi_{\rm B} > \xi_{\rm CRIT}$ are unstable against gravitational collapse. The density profile of a critical BE sphere is given in Figure 4.1 .

We assume critical BE density profiles when modelling prestellar cores. While the cores in Ophiuchus are not necessarily isothermal or in hydrostatic equilibrium, a critical BE density profile provides a flat central region and inverse square envelope.

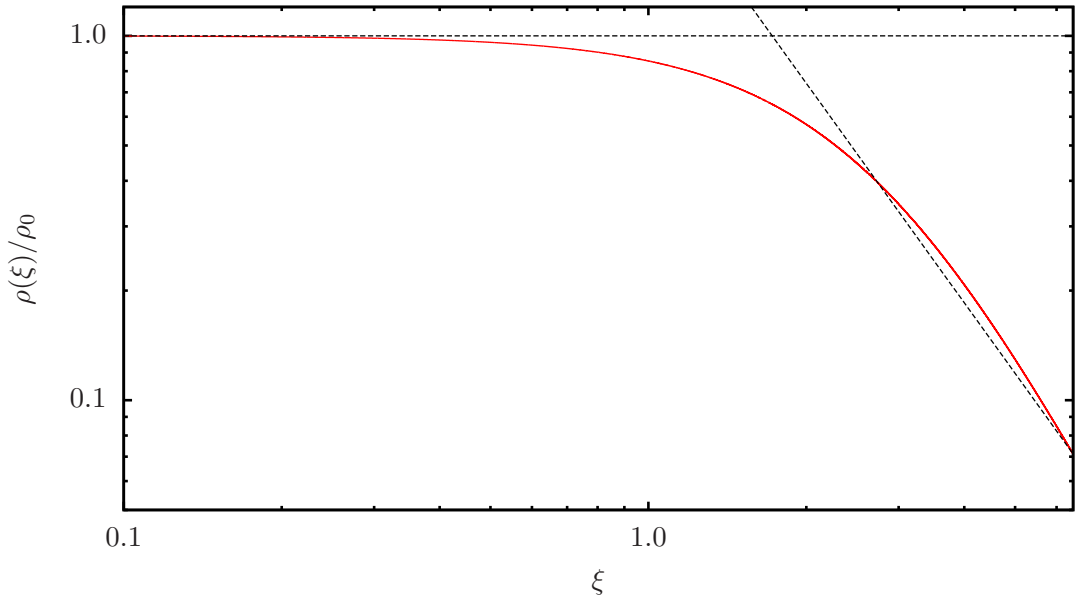

Figure 4.1: The solid red line show the dimensionless density $\rho(\xi)/\rho_0$ of a critical BE sphere against dimensionless radius ξ. The density is given by $e^{\psi(\xi)}$ where $\psi(\xi)$ is given in Equation (4.6). The dashed lines show the flat core and approximately inverse square envelope.

These features are found in many models of core collapse and provide convenient initial conditions.

The density profile of a BE sphere can be calculated by considering the forces upon a core. A spherically symmetric core of isothermal gas will be in hydrostatic equilibrium if

$$\frac{\mathrm{d}P}{\mathrm{d}r} = -\frac{GM(r)\rho(r)}{r^2}\,. \tag{4.1}$$

As the gas is isothermal and has equation of state

$$P = c_\mathrm{s}^2\rho \tag{4.2}$$

where c_s is the isothermal sound speed, we can eliminate P from Equation (4.1) so that

$$\frac{\mathrm{d}}{\mathrm{d}r}\ln(\rho(r)) = -\frac{GM(r)}{c_\mathrm{s}^2 r^2}\,. \tag{4.3}$$

We now introduce the dimensionless radius

$$\xi = \frac{r}{R_0}\,, \tag{4.4}$$

dimensionless mass

$$\mu(\xi) = \frac{M(\xi R_0)}{M_0}\,, \tag{4.5}$$

and the dimensionless potential

$$\psi(\xi) = -\ln\left(\frac{\rho(\xi R_0)}{\rho_0}\right), \tag{4.6}$$

where ρ_0 is the central density of the cloud, and

$$R_0 = \frac{c_{\rm S}}{\sqrt{4\pi G\rho_0}}, \tag{4.7}$$

$$M_0 = \frac{c_{\rm S}^3}{G\sqrt{4\pi G\rho_0}}. \tag{4.8}$$

Equations (4.5) and (4.6) then reduce to

$$\frac{{\rm d}\mu}{{\rm d}\xi} = \xi^2 {\rm e}^{-\psi(\xi)}, \tag{4.9}$$

$$\frac{{\rm d}\psi}{{\rm d}\xi} = \frac{\mu(\xi)}{\xi^2}. \tag{4.10}$$

Equations (4.9) and (4.10) are integrated numerically to give $\mu(\xi)$ and $\psi(\xi)$.

If we consider the boundary of the cloud $\xi_{\rm B}$, the hydrostatic gas pressure will be

$$P(\xi_{\rm B}) = c_{\rm S}^2 \rho(\xi_{\rm B}) = c_{\rm S}^2 \rho_0 {\rm e}^{-\psi(\xi_{\rm B})}. \tag{4.11}$$

For the cloud to be in equilibrium with its surroundings, we require an external pressure $P_{\rm EXT} = P(\xi_{\rm B})$. For low values of $\xi_{\rm B}$, $P_{\rm EXT}$ is low and the cloud is extended with a flat density profile and weak self gravity. Increasing $\xi_{\rm B}$ increases $P_{\rm EXT}$ and the cloud becomes smaller and more centrally condensed. $P_{\rm EXT}$ reaches its maximum at $\xi_{\rm B} = \xi_{\rm CRIT} = 6.451$, and for larger values of $P_{\rm EXT}$ there are no further equilibria and the cloud collapses under its own self-gravity.

We integrate Equations (4.9) and (4.10) within limits $0 \leq \xi \leq \xi_{\rm CRIT}$ to give the mass profile of a critical Bonnor-Ebert sphere. Values of ξ and $\mu(\xi)$ are stored in a lookup table; any solutions between entries in the table are estimated by linear interpolation. Note that this mass profile will be scaled to arbitrary values of M and R and will therefore not generally be in equilibrium. A full description of the application of this profile to a triaxial core is given in Chapter 7.

4.2 The velocity field

Spectroscopic observations of prestellar cores suggest that their velocity fields contain ordered rotational motions (e.g. Goodman et al., 1993), ordered radial ex-

cursions from of inward or outward pulsation (e.g. Keto et al., 2006) and random turbulent motions (e.g. Dubinski et al., 1995). The observed radial non-thermal velocity dispersion $\sigma_{\rm NT}$ therefore has contributions from each of these components:

$$\sigma^2_{\rm NT} = \sigma^2_{\rm ROT} + \sigma^2_{\rm RAD} + \sigma^2_{\rm TURB}\,. \tag{4.12}$$

Here $\sigma_{\rm ROT}$ is the velocity dispersion along the line of sight from rotational motions, $\sigma_{\rm RAD}$ is the velocity dispersion from radial excursions and $\sigma_{\rm TURB}$ is the velocity dispersion from turbulent motions.

If we consider a simple model where a spherical core with measured $\sigma_{\rm NT}$ is i) in solid-body rotation about an axis perpendicular to the line of sight, ii) is undergoing isotropic expansion or contraction and iii) also contains some random turbulence, we are presented with at least two free parameters: the relative weights of $\sigma_{\rm ROT}$, $\sigma_{\rm RAD}$, $\sigma_{\rm TURB}$. This problem becomes more complicated if the core is ellipsoidal instead of spherical. Lin et al. (1965) show that gravitational infall of a core is likely to be fastest along its shortest axis. This anisotropy adds further free parameters to the problem and we have no way of estimating particular values for any of them.

To simplify this problem, we only consider the turbulent component of the velocity field. We show that turbulent velocity fields can be modified to reproduce ordered rotational and radial motions as well as turbulence without adding further free parameters.

4.2.1 Turbulent motions

We simulate turbulence by constructing a random Gaussian velocity field in which the amount of energy at different scales is defined by the power spectrum

$$P(k) \propto \begin{cases} k^{-\alpha} & \text{if } k_{\rm MIN} \leq k \leq k_{\rm MAX}\,, \\ 0 & \text{otherwise}\,, \end{cases} \tag{4.13}$$

where k is the wavenumber of the velocity mode. The wavelength of a velocity mode is given by $\lambda = 2\pi/k$. The power spectrum exponent α defines how the total energy of the system is distributed amongst different length scales; larger values of α concentrate more energy in longer wavelength modes. $k_{\rm MIN}$ defines the lowest permitted wavenumber (and hence longest wavelength) and $k_{\rm MAX}$ defines the highest permitted wavenumber (shortest wavelength).

We consider the velocity field within a three-dimensional computational domain of edge-length 2π. Burkert and Bodenheimer (2000) suggest that $\alpha = 2$ agrees well with theory and observations. We set $k_{\rm MIN} = 1$ so that the largest velocity modes are

the same size as the domain. As α is positive, the only constraint we need to place on k_{MAX} is that it is large enough that $P(k_{\mathrm{MIN}}) \gg P(k_{\mathrm{MAX}})$. We adopt $k_{\mathrm{MAX}} = 64$.

In three dimensions, each velocity mode has a spatial frequency along each of the three axes and is therefore characterized by a wavevector $\boldsymbol{k} = (k_x, k_y, k_z)$ with wavenumber $k = |\boldsymbol{k}|$. The amount of energy between modes k and $k + \mathrm{d}k$ is given by

$$\mathrm{d}P_k = k^{-\alpha}\,\mathrm{d}k\,, \tag{4.14}$$

and the volume of k-space between k and $k + \mathrm{d}k$ is given by

$$\mathrm{d}V_k = 4\pi k^2\,\mathrm{d}k\,. \tag{4.15}$$

Hence we define the specific spectral energy density

$$E(k) = \frac{\mathrm{d}P_k}{\mathrm{d}V_k} = \frac{1}{4\pi}k^{-(\alpha+2)}\,, \tag{4.16}$$

where $E(k)$ gives the energy density at position $\boldsymbol{k}$ in k-space.

We statistically reproduce the power spectrum given in Equation (4.13). For all wavevectors $\boldsymbol{k}$ with $k_{\mathrm{MIN}} \leq k \leq k_{\mathrm{MAX}}$ and integer values of k_x, k_y and k_z, we assign amplitude and phase

$$\begin{aligned} \boldsymbol{a}(\boldsymbol{k}) &= \sqrt{E(k)}\,\boldsymbol{\mathcal{G}}\,, \\ \boldsymbol{\varphi}(\boldsymbol{k}) &= 2\pi\,\boldsymbol{\mathcal{R}}\,, \end{aligned} \tag{4.17}$$

where $\boldsymbol{\mathcal{G}}$ is a vector of three numbers drawn from a Gaussian distribution with zero mean and unit variance and $\boldsymbol{\mathcal{R}}$ is a vector of three numbers drawn from a uniform distribution between zero and one. The amplitudes and phases are now used to generate a velocity field in real space via the Fourier transform

$$\boldsymbol{v}(\boldsymbol{x}) = \frac{1}{(2\pi)^2}\mathrm{Re}\left(\int \hat{\boldsymbol{v}}(\boldsymbol{k})e^{i\boldsymbol{k}\boldsymbol{x}}\,\mathrm{d}^3k\right), \tag{4.18}$$

where

$$\hat{\boldsymbol{v}}(\boldsymbol{k}) = \boldsymbol{a}(\boldsymbol{k})\cos(\boldsymbol{\varphi}(\boldsymbol{k})) + \mathrm{i}\,\boldsymbol{a}(\boldsymbol{k})\sin(\boldsymbol{\varphi}(\boldsymbol{k})) \tag{4.19}$$

We solve Equation (4.18) numerically using the fast Fourier transform library FFTW (Frigo and Johnson, 2005) which produces a 128^3 grid of the velocity field with a spatial edge length of 2π. The velocities of individual SPH particles are then computed by linear interpolation on this grid (see Chapter 7).

4.2.2 Ordered motions

We can introduce large scale rotation and radial motion into the velocity field whilst maintaining the power spectrum in Equation (4.13) by i) modifying the $k = 1$ modes and ii) aligning the centre of the core with centre of the velocity grid. If we consider a core velocity-field with only $\boldsymbol{k} = (1, 0, 0)$, $\boldsymbol{k} = (0, 1, 0)$ and $\boldsymbol{k} = (0, 0, 1)$, we see from Figure 4.2 that we produce ordered compression and rotation if these modes have

$$\begin{aligned} \begin{bmatrix} \boldsymbol{a}(1,0,0) \\ \boldsymbol{a}(0,1,0) \\ \boldsymbol{a}(0,0,1) \end{bmatrix} &= \sqrt{E(1)} \begin{bmatrix} r_x & \omega_z & -\omega_y \\ -\omega_z & r_y & \omega_x \\ \omega_y & -\omega_x & r_z \end{bmatrix}, \\ \begin{bmatrix} \boldsymbol{\varphi}(1,0,0) \\ \boldsymbol{\varphi}(0,1,0) \\ \boldsymbol{\varphi}(0,0,1) \end{bmatrix} &= \begin{bmatrix} \pi/2 & \pi/2 & \pi/2 \\ \pi/2 & \pi/2 & \pi/2 \\ \pi/2 & \pi/2 & \pi/2 \end{bmatrix}, \end{aligned} \tag{4.20}$$

where r_x, r_y and r_z are radial velocity amplitudes and ω_x, ω_y and ω_z are rotational velocity amplitudes. The diameter of the core is scaled to π to remove the periodicity of these large-scale modes.

The value of a radial amplitude is proportional to the rate at which the core expands along the denoted axis. For example, if $r_x < 1$, then the core is collapsing along the x-axis. If $r_x > 1$, then the core is expanding along the x-axis. The rotational amplitudes control bulk rotation. If we consider the vector $\boldsymbol{\omega} = (\omega_x, \omega_y, \omega_z)$, the core's axis of rotation is given by the unit vector $\hat{\boldsymbol{\omega}}$ with angular momentum proportional to $|\boldsymbol{\omega}|$. The values of r_x, r_y, r_z, ω_x, ω_y and ω_z are independently drawn from a Gaussian distribution with mean zero and unit variance. This ensures that the velocity field maintains the power spectrum given in Equation (4.13).

The velocity field can be orientated to give any arbitrary ordering of r_x, r_y and r_z. In Chapter 7 we apply these fields to triaxial ellipsoids with semi-axes $A \geq B \geq C$ respectively aligned with the x, y and z directions. We orientate the fields so that $r_x \leq r_y \leq r_z$. This reflects the assumption that the cores are collapsing fastest along their shortest axes and slowest along their longest. The axis of rotation has a random direction.

Note that we *only* modify the $k = 1$ velocity modes. All modes with $k > 1$ remain unchanged from the prescription given in Section 4.2.1. Hence we have a velocity field composed of ordered rotation, ordered radial excursions *and* stochastic turbulent motions.

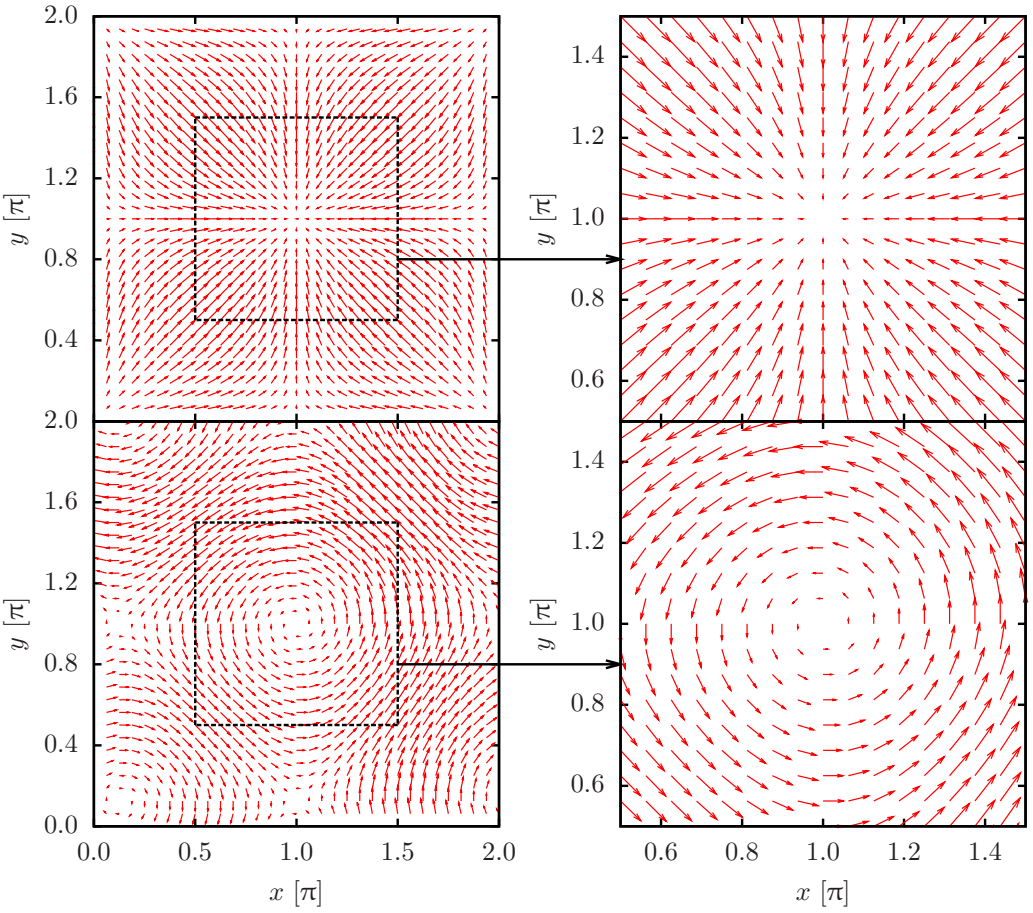

Figure 4.2: Top left: A two-dimensional compressive velocity field with modes

$$\begin{bmatrix} \boldsymbol{a}(1,0) \\ \boldsymbol{a}(0,1) \end{bmatrix} = \begin{bmatrix} -1 & 0 \\ 0 & -1 \end{bmatrix},$$
$$\begin{bmatrix} \boldsymbol{\varphi}(1,0) \\ \boldsymbol{\varphi}(0,1) \end{bmatrix} = \begin{bmatrix} \pi/2 & 0 \\ 0 & \pi/2 \end{bmatrix}.$$

Bottom left: A two-dimensional solenoidal velocity field with modes

$$\begin{bmatrix} \boldsymbol{a}(1,0) \\ \boldsymbol{a}(0,1) \end{bmatrix} = \begin{bmatrix} 0 & 1 \\ -1 & 0 \end{bmatrix},$$
$$\begin{bmatrix} \boldsymbol{\varphi}(1,0) \\ \boldsymbol{\varphi}(0,1) \end{bmatrix} = \begin{bmatrix} 0 & \pi/2 \\ \pi/2 & 0 \end{bmatrix}.$$

Within the limits $\pi/2 \leq x \leq 3\pi/2$ and $\pi/2 \leq y \leq 3\pi/2$ we have large-scale rotation and radial motions, as seen on the right.

4.2.3 Compressive and solenoidal velocity fields

We introduce a single free parameter to the generation of velocity fields: the ratio of solenoidal to compressive energy. The velocity field can be modified to produce a purely compressive or a purely solenoidal field. For a purely compressive field, $\nabla \times \boldsymbol{v} = 0$ at all points in space. Such a field consists only of regions of infall, expansion and shocks. This includes the large-scale radial velocity components described in Section 4.2.2. For a purely solenoidal field, $\nabla \cdot \boldsymbol{v} = 0$ at all points in space. This field consists only of regions of shearing and rotation. This includes the large-scale rotational velocity components described in Section 4.2.2.

To produce a purely compressive velocity field, we apply the transformation

$$\boldsymbol{a}(\boldsymbol{k}) \rightarrow (\hat{\boldsymbol{k}} \cdot \boldsymbol{a}(\boldsymbol{k}))\hat{\boldsymbol{k}}\,, \tag{4.21}$$

where $\hat{\boldsymbol{k}}$ is the unit vector of $\boldsymbol{k}$. Conversely, we can produce a purely solenoidal field via the transformation

$$\boldsymbol{a}(\boldsymbol{k}) \rightarrow \boldsymbol{a}(\boldsymbol{k}) - (\hat{\boldsymbol{k}} \cdot \boldsymbol{a}(\boldsymbol{k}))\hat{\boldsymbol{k}}\,. \tag{4.22}$$

Applying neither transformation results in a thermal velocity field with on average twice as much energy in solenoidal modes as compressive modes.

We define the parameter

$$\Xi = \frac{\bar{E}_{\mathrm{SOL}}}{\bar{E}_{\mathrm{COM}}} \tag{4.23}$$

where $\bar{E}_{\mathrm{SOL}}$ is the average amount of energy injected into solenoidal velocity modes and $\bar{E}_{\mathrm{COM}}$ is the average amount of energy injected into compressive velocity modes. From Equations (4.21) and (4.22), we have three possibilities: $\Xi = \infty$ for a purely solenoidal field, $\Xi = 0$ for a purely compressive field and $\Xi = 2$ for the thermal mixture of the two.

4.3 Summary

In this chapter we have defined the density and velocity structure used to model prestellar cores. For convenience we adopt the radial density profile of a critical Bonnor-Ebert sphere. The cores are not generally in equilibrium, however many observed core density profiles share the flat peak and inverse-square envelope of a critical Bonnor-Ebert density profile.

We generate a velocity field where large-scale rotation and radial motions are linked to the power spectrum of a random Gaussian field. This gives a velocity field in which the strongest velocity modes produce radial excursions and rotation,

and the remaining velocity modes produce shocks, shearing and vortices (i.e. turbulence). We can also modify the field to ensure that it is purely compressive, purely solenoidal or a 2:1 thermal mixture of solenoidal to compressive energy. Given the constraints on values of $\sigma_{\rm NT}$ from Chapter 2, we reduce the number of free parameters defining the velocity field to one: $\Xi = \bar{E}_{\rm SOL}/\bar{E}_{\rm COM}$, modulo the random seed used to generate different realisations.

Chapter 5

Smoothed Particle Hydrodynamics

In the previous three chapters we have defined the initial conditions of prestellar cores. Now we need a means of evolving them. In this chapter we provide an overview of the numerical method used to model gas flow within prestellar cores. We use the SEREN implementation of Smoothed Particle Hydrodynamics which includes hydrodynamical forces and self-gravity. We also include radiative transport which is discussed in Chapter 6.

Dense regions of gas which are gravitationally bound are replaced by sink particles. These are point masses which are analogous to protostars. They do not interact hydrodynamically with the surrounding environment, but they do experience gravitational forces and accrete infalling gas.

5.1 Introduction

The evolution of a star forming gas is generally a non-linear process which needs to be solved numerically instead of analytically. If we consider only the hydrodynamical forces within a gas, its evolution can be followed by solving the equations of hydrodynamics at all points in space. These equations are given by

$$\frac{\mathrm{d}\rho}{\mathrm{d}t} \equiv \frac{\partial \rho}{\partial t} + \boldsymbol{v} \cdot \nabla \rho = -\rho \nabla \cdot \boldsymbol{v}\,, \qquad \text{Continuity equation;} \qquad (5.1)$$

$$\rho \frac{\mathrm{d}\boldsymbol{v}}{\mathrm{d}t} \equiv \frac{\partial \rho \boldsymbol{v}}{\partial t} + \rho \boldsymbol{v} \cdot \nabla \boldsymbol{v} = -\nabla P \qquad \text{Momentum equation;} \qquad (5.2)$$

$$\frac{\mathrm{d}u}{\mathrm{d}t} \equiv \frac{\partial u}{\partial t} + \boldsymbol{v} \cdot \nabla u = -\frac{P}{\rho} \nabla \cdot \boldsymbol{v} \qquad \text{Energy equation.} \qquad (5.3)$$

Here we have gas velocity $\boldsymbol{v}$, density ρ and specific internal energy u. The gas pressure P is related to ρ and u by the equation of state

$$P = \frac{\rho k_{\rm B} T}{\bar{m}}\,, \tag{5.4}$$

where $\bar{m} \approx 4.8 \times 10^{-23}$ g is the mean molecular mass for cold interstellar gas. In this thesis we calculate the pressure implicitly from the internal energy. The calculation is defined in Chapter 6 .

The equations of hydrodynamics can be solved using two different formulations. The Eulerian formulation assumes a static reference frame against which the fluid can move. The computational domain is typically divided into a fixed position grid. At each grid point, the Eulerian derivatives $\partial\rho/\partial t$, $\partial\rho\boldsymbol{v}/\partial t$ and $\partial u/\partial t$ are integrated to evolve the gas over a timestep.

Conversely, the Lagrangian formulation assumes a reference frame which moves with the fluid. The fluid is typically divided into a finite number of particles, each with position and velocity. The Lagrangian derivatives $\mathrm{d}\rho/\mathrm{d}t$, $\rho\mathrm{d}\boldsymbol{v}/\mathrm{d}t$ and $\mathrm{d}u/\mathrm{d}t$ are integrated at each particle position to evolve the gas over a timestep.

Both these methods have advantages and disadvantages, however the Lagrangian formulation has some features which are particularly useful for simulations of star formation: i) as the particles can move freely, this method can inherently cope with length scales which vary by several orders of magnitude; ii) unlike Eulerian grids, there are no preferred directions along which gas flows (this is particularly useful for modelling anything that rotates, e.g. accretion discs). However, there are some disadvantages to particle based schemes. For example, particles can interpenetrate unphysically in colliding flows (see Section 5.2.5) and density calculations from a distribution of particles can be noisier than those from a grid.

In this thesis we use the SEREN Smoothed Particle Hydrodynamics (SPH) code (Hubber et al., 2011) to model gas evolution in star forming regions. In Section 5.2 of this chapter we give a brief overview of SPH including artificial viscosity and self gravity. In Section 5.3 we describe the concept of sink particles which are used to model to protostars.

5.2 The concept of SPH

SPH is a Lagrangian formulation of hydrodynamics first introduced by Lucy (1977) and then Gingold and Monaghan (1977). It models a continuous fluid as an ensemble of N particles. At each particle position, the momentum equation and energy

equation are integrated to evolve the gas. Each particle has mass m_i, therefore density is a function of the particle coordinates and the continuity equation generally does not need to be solved.

To model a continuous fluid, each particle is smoothed over a kernel which overlaps with $\mathcal{N}$ other particles. The value of a continuous physical quantity, A, convolved with the smoothing kernel at point $\boldsymbol{r}$ in space is given by

$$\langle A(\boldsymbol{r})\rangle = \int_V A(\boldsymbol{r'})W(\boldsymbol{r}-\boldsymbol{r'},h)\,\mathrm{d}\boldsymbol{r'}^3\,, \tag{5.5}$$

where $W(\boldsymbol{r}-\boldsymbol{r'},h)$ is the kernel function centred at $\boldsymbol{r}$ with length-scale h. We can choose any kernel function so long as two conditions are satisfied. First, the kernel function must tend to a Dirac delta function as h tends to zero, i.e.

$$\lim_{h\to 0}[W(\boldsymbol{r}-\boldsymbol{r'},h)] = \delta(\boldsymbol{r}-\boldsymbol{r'})\,, \tag{5.6}$$

and second, the kernel function must be normalised so that

$$\int_V W(\boldsymbol{r}-\boldsymbol{r'},h)\,\mathrm{d}\boldsymbol{r'}^3 = 1\,. \tag{5.7}$$

To perform SPH calculations, we replace the integral in Equation (5.5) with a summation over $\mathcal{N}$ particles within the extent of the kernel, i.e.

$$\langle A(\boldsymbol{r_i})\rangle = \sum_{j=1}^{\mathcal{N}} \frac{m_j}{\rho_j} A_j W(\boldsymbol{r}_{ij},h)\,. \tag{5.8}$$

Where $\boldsymbol{r}_{ij} \equiv \boldsymbol{r}_i - \boldsymbol{r}_j$. Note that the volume element $\mathrm{d}\boldsymbol{r'}^3$ has been replaced by $\frac{m_j}{\rho_j}$. We can also calculate the spatial derivative of A,

$$\langle \nabla A(\boldsymbol{r_i})\rangle = \sum_{j=1}^{\mathcal{N}} \frac{m_j}{\rho_j} A_j \nabla W(\boldsymbol{r}_{ij},h)\,. \tag{5.9}$$

This is useful as most kernel functions will have well known analytical solutions to $\nabla W(\boldsymbol{r}_{ij},h)$.

5.2.1 Kernel

The original formulation of SPH by Lucy (1977) used a Gaussian smoothing kernel. This kernel is infinite in extent and each SPH calculation needs to be iterated over

all of the particles, i.e. $\mathcal{N} \equiv N$. This can be a very computationally expensive process. Furthermore, it is arguable that this is physically unrealistic as quantities such as pressure and density only act locally and should not be smoothed over the entire fluid. Instead, most modern SPH codes adopt the M4 kernel (Monaghan and Lattanzio, 1985) which has compact support. This kernel is spherically symmetric and in three dimensions is given by

$$W_{\mathrm{M4}}(s) = \frac{1}{\pi h^3} \begin{cases} 1 - \frac{3}{2}s^2 + \frac{3}{4}s^3 & \text{if } 0 \leq s \leq 1; \\ \frac{1}{4}(2-s)^3 & \text{if } 1 \leq s \leq 2; \\ 0 & \text{if } s > 2 \end{cases} , \tag{5.10}$$

where $s \equiv |\boldsymbol{r}_{ij}|/h$. The first spatial derivative is then

$$\frac{\mathrm{d}W_{\mathrm{M4}}}{\mathrm{d}r}(s) = \frac{1}{\pi h^4} \begin{cases} 3s - \frac{9}{4}s^2 & \text{if } 0 \leq s \leq 1; \\ \frac{3}{4}(2-s)^2 & \text{if } 1 \leq s \leq 2; \\ 0 & \text{if } s > 2 \end{cases} \tag{5.11}$$

where $\nabla W_{\mathrm{M4}} \equiv \hat{\boldsymbol{r}}_{ij} \frac{\mathrm{d}W_{\mathrm{M4}}}{\mathrm{d}r}$.

5.2.2 Smoothing length

Early SPH simulations used global smoothing lengths based on average inter-particle spacing. However, in order to sufficiently resolve gas physics at different length scales, it is necessary for each particle to have a smoothing length that varies with gas density.

Monaghan (2002) suggests that the smoothing length should be a function of density, i.e.

$$h_i = \eta \left(\frac{m_i}{\rho_i} \right)^{\frac{1}{3}} , \tag{5.12}$$

where $\eta = 1.2$, as suggested by Price and Monaghan (2004). Note that ρ_i is an SPH quantity given by

$$\rho_i = \sum_{j=1}^{\mathcal{N}} m_j W(\boldsymbol{r}_{ij}, h_i) . \tag{5.13}$$

As these two quantities are interdependent, the value of h_i must be solved by iteration. Given an initial estimate of h_i and a target value h calculated from Equation (5.12). Equations (5.13) and (5.12) are then iterated until $|h_i - h|/h < 10^{-2}$.

For the M4 kernel in three dimensions, each SPH particle has an average number

of neighbours

$$\bar{\mathcal{N}} \approx \frac{4}{3}\pi(2\eta)^3 \approx 58\,. \tag{5.14}$$

5.2.3 SPH equations

Using Equation (5.8) we can calculate SPH quantities at each particle position. To ensure that all forces between particle pairs are equal and opposite, the identity

$$\frac{\nabla A}{\rho} = \nabla\left(\frac{A}{\rho}\right) + \frac{A}{\rho^2}\nabla\rho\,, \tag{5.15}$$

is substituted into Equation (5.2) to give

$$\left.\frac{\mathrm{d}\boldsymbol{v}_i}{\mathrm{d}t}\right|_{\text{HYDRO}} = -\sum_{j=1}^{\mathcal{N}} m_j \left(\frac{P_i}{\rho_i^2} + \frac{P_j}{\rho_j^2}\right)\nabla_i W(\boldsymbol{r}_{ij}, h_i)\,. \tag{5.16}$$

The rate of change of specific internal energy is calculated by substituting Equation (5.1) into Equation (5.3) to give

$$\frac{\mathrm{d}u_i}{\mathrm{d}t} = \frac{P_i}{\rho_i^2}\frac{\mathrm{d}\rho_i}{\mathrm{d}t}\,. \tag{5.17}$$

As an SPH quantity, this is calculated as

$$\left.\frac{\mathrm{d}u_i}{\mathrm{d}t}\right|_{\text{HYDRO}} = \frac{P_i}{\rho_i^2}\sum_{j=1}^{\mathcal{N}} m_j \boldsymbol{v}_{ij}\cdot\nabla_i W(\boldsymbol{r}_{ij}, h_i)\,, \tag{5.18}$$

where $\boldsymbol{v}_{ij} \equiv \boldsymbol{v}_i - \boldsymbol{v}_j$.

5.2.4 Additional terms

Nelson and Papaloizou (1994) note that variable smoothing lengths can cause SPH calculations to fail to conserve energy over time. To correct for this, Monaghan (2002) shows that Equations (5.16) and (5.16) should be replaced by

$$\left.\frac{\mathrm{d}\boldsymbol{v}_i}{\mathrm{d}t}\right|_{\text{HYDRO}} = -\sum_{j=1}^{\mathcal{N}} m_j \left(\frac{P_i}{\rho_i^2\Omega_i}\nabla_i W(\boldsymbol{r}_{ij}, h_i) + \frac{P_j}{\rho_j^2\Omega_j}\nabla_i W(\boldsymbol{r}_{ij}, h_j)\right)\,, \tag{5.19}$$

and

$$\left.\frac{\mathrm{d}u_i}{\mathrm{d}t}\right|_{\text{HYDRO}} = \frac{P_i}{\rho_i^2\Omega_i}\sum_{j=1}^{\mathcal{N}} m_j \boldsymbol{v}_{ij}\cdot\nabla_i W(\boldsymbol{r}_{ij}, h_i)\,, \tag{5.20}$$

respectively, where

$$\Omega_i = 1 - \frac{\partial h_i}{\partial \rho_i} \sum_{j=1}^{\mathcal{N}} m_j \frac{\partial W}{\partial h}(\boldsymbol{r}_{ij}, h_i)\,, \tag{5.21}$$

and

$$\frac{\partial W_{\text{M4}}}{\partial h} = \frac{1}{\pi h^4} \begin{cases} -3 + \frac{15}{2}s^2 - \frac{9}{2}s^3 & \text{if } 0 \leq s \leq 1; \\ -6 + 12s - \frac{15}{2}s^2 + \frac{3}{2}s^3 & \text{if } 1 \leq s \leq 2; \\ 0 & \text{if } s > 2\,. \end{cases} \tag{5.22}$$

5.2.5 Artificial viscosity

Artificial viscosity is added to ensure that shocks are captured adequately. Without this, SPH particles can oscillate unphysically behind a shock front. Also, for converging flows with high Mach number, particles can interpenetrate instead of decelerating at the shock front.

To alleviate this problem, Monaghan (1997) introduces a viscosity based contribution to the equation of motion:

$$\left.\frac{\mathrm{d}\boldsymbol{v}_i}{\mathrm{d}t}\right|_{\text{VISC}} = -\sum_{j=1}^{\mathcal{N}} m_j \Pi_{ij} \nabla_i \bar{W}(\boldsymbol{r}_{ij}, h_i, h_j)\,, \tag{5.23}$$

where

$$\bar{W}(\boldsymbol{r}_{ij}, h_i, h_j) = \frac{\nabla_i W(\boldsymbol{r}_{ij}, h_i) + \nabla_i W(\boldsymbol{r}_{ij}, h_j)}{2}\,, \tag{5.24}$$

and

$$\Pi_{ij} = \begin{cases} -\dfrac{\alpha v_{\text{SIG}} \boldsymbol{v}_{ij} \cdot \boldsymbol{r}_{ij}}{\bar{\rho}_{ij} |\boldsymbol{r}_{ij}|} & \text{if } \boldsymbol{v}_{ij} \cdot \boldsymbol{r}_{ij} \leq 0\,; \\ 0 & \text{if } \boldsymbol{v}_{ij} \cdot \boldsymbol{r}_{ij} > 0\,. \end{cases} \tag{5.25}$$

Here $\bar{\rho}_{ij} = (\rho_i + \rho_j)/2$, and v_{SIG} is the signal velocity:

$$v_{\text{SIG}} = c_i + c_j - \beta \frac{\boldsymbol{v}_{ij} \cdot \boldsymbol{r}_{ij}}{|\boldsymbol{r}_{ij}|}\,. \tag{5.26}$$

The dissipation of kinetic energy will then heat the gas with

$$\left.\frac{\mathrm{d}u_i}{\mathrm{d}t}\right|_{\text{VISC}} = \sum_{j=1}^{\mathcal{N}} m_j \Lambda_{ij} \hat{\boldsymbol{r}}_{ij} \cdot \bar{W}(\boldsymbol{r}_{ij}, h_i, h_j)\,, \tag{5.27}$$

where

$$\Lambda_{ij} = \begin{cases} -\dfrac{\alpha v_{\text{SIG}} (\boldsymbol{v}_{ij} \cdot \boldsymbol{r}_{ij})^2}{2\bar{\rho}_{ij} |\boldsymbol{r}_{ij}|^2} & \text{if } \boldsymbol{v}_{ij} \cdot \boldsymbol{r}_{ij} \leq 0\,; \\ 0 & \text{if } \boldsymbol{v}_{ij} \cdot \boldsymbol{r}_{ij} > 0\,. \end{cases} \tag{5.28}$$

The terms α and β control the artificial viscosity in regions of low and high-Mach number shocks respectively. Monaghan (1997) suggests values of $\alpha = 1$ and $\beta = 2$ in order to adequately capture these shocks. Morris and Monaghan (1997) simplify this parametrisation by explicitly setting $\beta \equiv 2\alpha$.

5.2.6 Time-dependent viscosity

This formulation of artificial viscosity is well suited to planar shocks, however it can unintentionally add viscosity to shearing flows, leading to the unphysical transport of angular momentum. In order to mitigate this effect, Morris and Monaghan (1997) assign a value of α_i to each SPH particle. This can decay with time so that artificial viscosity is reduced in regions where it is not needed.

Each particle has α_i which evolves according to

$$\frac{\mathrm{d}\alpha_i}{\mathrm{d}t} = \frac{\alpha_{\mathrm{MIN}} - \alpha_i}{\tau_i} + S_i \,. \tag{5.29}$$

Here, α_{MIN} is the minimum value of α_i, as suggested by Morris and Monaghan (1997), and τ is the time scale at which α_i decays:

$$\tau_i = \frac{h_i}{c_i C} \,, \tag{5.30}$$

where c_i is the local sound speed and $C = 0.1$. The source term S_i is given by Rosswog et al. (2000) as

$$S_i = (\alpha_{\mathrm{MAX}} - \alpha_{\mathrm{MIN}}) \begin{cases} -\nabla \cdot \boldsymbol{v}_i & \text{if } \nabla \cdot \boldsymbol{v}_i \leq 0 \,; \\ 0 & \text{if } \nabla \cdot \boldsymbol{v}_i > 0 \,. \end{cases} \tag{5.31}$$

This formulation ensures that $\alpha_i = \alpha_{\mathrm{MAX}} = 1$ in shocked regions, but then α_i can decay down to α_{MIN} outside of these regions. Here we set $\alpha_{\mathrm{MIN}} = 0.1$. The value of α in Equations (5.25) and (5.28) is now replaced by α_{ij} where $\alpha_{ij} = (\alpha_i + \alpha_j)/2$.

5.2.7 Gravity

As SPH particles are not point masses, the gravitational forces acting upon a particle must be kernel softened. Price and Monaghan (2007) derive a formulation of gravity

with a potential smoothing kernel

$$\phi(\boldsymbol{r},h) = 4\pi\left(-\frac{1}{r}\int_0^r W(\boldsymbol{r'},h)r'^2\,\mathrm{d}r' + \int_0^r W(\boldsymbol{r'},h)r'\,\mathrm{d}r' - \int_0^{2h} W(\boldsymbol{r'},h)r'\,\mathrm{d}r'\right), \tag{5.32}$$

and force smoothing kernel

$$\phi'(\boldsymbol{r},h) = \frac{4\pi}{r^2}\int_0^r W(\boldsymbol{r'},h)r'^2\,\mathrm{d}r', \tag{5.33}$$

The acceleration due to gravity for each particle is then given by

$$\left.\frac{\mathrm{d}\boldsymbol{v}_i}{\mathrm{d}t}\right|_{\mathrm{GRAV}} = -G\sum_{j=1}^{N} m_j\bar{\phi}'(\boldsymbol{r}_{ij},h_i,h_j)\hat{\boldsymbol{r}}_{ij} - \frac{G}{2}\sum_{j=1}^{\mathcal{N}}\left(\frac{\xi_i}{\Omega_i}\nabla_i W(\boldsymbol{r}_{ij},h_i) + \frac{\xi_j}{\Omega_j}\nabla_i W(\boldsymbol{r}_{ij},h_j)\right), \tag{5.34}$$

where

$$\bar{\phi}'(\boldsymbol{r}_{ij},h_i,h_j) = \frac{\phi'(\boldsymbol{r}_{ij},h_i)+\phi'(\boldsymbol{r}_{ij},h_j)}{2}, \tag{5.35}$$

and

$$\xi_i = \frac{\partial h_i}{\partial \rho_i}\sum_{j=1}^{\mathcal{N}} m_j\frac{\partial\phi}{\partial h}(\boldsymbol{r}_{ij},h_i). \tag{5.36}$$

Here the first term on the right gives the standard prescription of kernel softened gravity and the second terms corrects the force at small distances to conserve energy. For the M4 kernel, we have

$$\phi'_{\mathrm{M4}}(s) = \frac{1}{h^2}\begin{cases}\frac{4}{3}s^3 - \frac{6}{5}s^5 + \frac{1}{2}s^6 & \text{if } 0\le s\le 1;\\ \frac{8}{3}s - 3s^2 + \frac{6}{5}s^3 - \frac{1}{6}s^4 - \frac{1}{15}s^{-2} & \text{if } 1\le s\le 2;\\ 1 & \text{if } s>2,\end{cases} \tag{5.37}$$

and

$$\frac{\partial\phi_{\mathrm{M4}}}{\partial h}(s) = \frac{1}{h^2}\begin{cases}\frac{7}{5} - 2s^2 + \frac{3}{2}s^4 - \frac{3}{5}s^5 & \text{if } 0\le s\le 1;\\ \frac{8}{5} - 4s^2 + 4s^3 - \frac{3}{2}s^4 + \frac{1}{5}s^5 & \text{if } 1\le s\le 2;\\ 0 & \text{if } s>2,\end{cases} \tag{5.38}$$

The gravitational potential at the position of particle i is given by

$$\Phi_i = G\sum_{j=1}^{N} m_j\bar{\phi}(\boldsymbol{r}_{ij},h_i,h_j), \tag{5.39}$$

where

$$\bar{\phi}(\boldsymbol{r}_{ij}, h_i, h_j) = \frac{\phi(\boldsymbol{r}_{ij}, h_i) + \phi(\boldsymbol{r}_{ij}, h_j)}{2}\,, \tag{5.40}$$

and

$$\phi_{\mathrm{M4}}(s) = \frac{1}{h}\begin{cases} \frac{7}{5} - \frac{2}{3}s^2 + \frac{3}{10}s^4 - \frac{1}{10}s^5 & 0 \leq s \leq 1; \\ \frac{8}{5} - \frac{4}{3}s^2 + s^3 - \frac{3}{10}s^4 + \frac{1}{30}s^5 - \frac{1}{5}s^{-1} & 1 \leq s \leq 2; \\ s^{-1} & \text{if } s > 2\,. \end{cases} \tag{5.41}$$

Calculating gravitational contributions from individual particles is a computationally expensive process. For efficiency, the SEREN SPH code uses a tree structure to identify clusters whose gravitational contributions can treated collectively using a multipole expansion. A detailed description of the algorithm is given by Hubber et al. (2011). We use a GADGET-style multipole acceptance criterion (Springel et al., 2001) with an error parameter of $\alpha_{\mathrm{MAC}} = 10^{-4}$.

5.2.8 Integration scheme

We numerically integrate Equations (5.16) and (5.18) to update the positions and velocities of each SPH particle. To advance each particle from the n^{th} to the $(n+1)^{\mathrm{th}}$ timestep we use a second-order Leapfrog drift-kick-drift scheme:

$$\boldsymbol{r}_i^{n+1/2} = \boldsymbol{r}_i^n + \boldsymbol{v}_i^n \frac{\Delta t_i}{2}\,, \tag{5.42}$$

$$\boldsymbol{v}_i^{n+1/2} = \boldsymbol{v}_i^n + \left.\frac{\mathrm{d}\boldsymbol{v}_i}{\mathrm{d}t}\right^{n-1/2} \frac{\Delta t_i}{2}\,, \tag{5.43}$$

$$\boldsymbol{v}_i^{n+1} = \boldsymbol{v}_i^n + \left.\frac{\mathrm{d}\boldsymbol{v}_i}{\mathrm{d}t}\right^{n+1/2} \Delta t_i\,, \tag{5.44}$$

$$\boldsymbol{r}_i^{n+1} = \boldsymbol{r}_i^n + \frac{1}{2}(\boldsymbol{v}_i^n + \boldsymbol{v}_i^{n+1})\Delta t_i\,, \tag{5.45}$$

$$\tag{5.46}$$

Here we define

$$\frac{\mathrm{d}\boldsymbol{v}_i}{\mathrm{d}t} \equiv \left.\frac{\mathrm{d}\boldsymbol{v}_i}{\mathrm{d}t}\right|_{\mathrm{HYDRO}} + \left.\frac{\mathrm{d}\boldsymbol{v}_i}{\mathrm{d}t}\right|_{\mathrm{VISC}} + \left.\frac{\mathrm{d}\boldsymbol{v}_i}{\mathrm{d}t}\right|_{\mathrm{GRAV}}\,. \tag{5.47}$$

Note that we do not update u_i using this scheme. The specific internal energy is updated using a quasi-implicit scheme detailed in Chapter 6.

The SEREN code uses multiple particle timesteps to assign an appropriate timestep to each individual particle (Hubber et al. (2011) provides a full description of the

algorithm). Each particle has a maximum timestep

$$\Delta t_{\rm MAX}, i = \gamma {\rm MIN}\left[\sqrt{\frac{h_i}{|\frac{{\rm d}\boldsymbol{v}_i}{{\rm d}t}|}}, \frac{h_i}{(1+1.2\alpha_i)c_i + (1+1.2\beta_i)h_i|\nabla\cdot\boldsymbol{v}_i|}\right]. \tag{5.48}$$

The first term on the right hand side is the standard SPH Courant condition and the second term is a modified version of the Courant condition that takes artificial viscosity into account. We choose a value of $\gamma = 0.1$ to ensure that the timesteps are suitably small.

5.2.9 Resolution

For all simulations presented in this thesis, we use a fixed particle mass of $M_{\rm SPH} = 10^{-5}\,{\rm M}_\odot$. The minimum resolvable mass in SPH simulations is roughly the total mass within a typical smoothing kernel, i.e. $M_{\rm MIN} \approx \bar{\mathcal{N}}\,M_{\rm SPH}$. Given Equation (5.14), we have $M_{\rm MIN} \approx 6\times10^{-4}\,{\rm M}_\odot$. The theoretical minimum mass for star formation (also known as *the opacity limit* (e.g. Whitworth and Stamatellos, 2006)) is $M_{\rm O} \approx 3\times10^{-3}\,{\rm M}_\odot \approx 3\,{\rm M}_{\rm J}$ and is therefore well resolved.

5.3 Sink particles

In simulations of star formation, regions of gas can collapse and produce very high densities. These densities can reduce the timesteps to a level so small that it is no longer computationally practical to continue the simulation. To overcome this, Bate et al. (1995) introduce *sink particles* which replace dense, gravitationally bound regions of gas with a single point mass. Sink particles do not experience or contribute to hydrodynamic forces, but they do interact gravitationally with SPH particles. Sink particles have an *accretion radius* and any SPH particle which is gravitationally bound to the sink and falls within this radius will be accreted on to the sink. This significantly improves the computational speed of the simulation at the expense of being unable to resolve the small scale physics within the sink radius.

5.3.1 Sink creation

In this thesis we use sink particles to model the formation of protostars. Candidate SPH particles are replaced by sink particles when gravitational collapse is assumed to be inevitable. We use the following criteria for sink creation:

- The candidate particle has a density greater than $\rho_{\rm SINK} = 10^{-9}\,{\rm g\,cm^3}$. This is

three or four orders of magnitude more dense than a core of gas which has begun to contract quasi-statically.

- The candidate particle must be at a local gravitational potential minimum, i.e. the gravitational potential at the candidate particle position is lower than that of all $\mathcal{N}$ of its neighbours.
- The candidate particle and all its neighbours are gravitationally bound, i.e. the sum of the kinetic energy plus the gravitational potential energy is negative.
- The velocity divergence at the position of the candidate particle is negative.
- The candidate particle is not within the accretion radius of another sink particle. This prevents the formation of overlapping sink particles.

5.3.2 Sink accretion

Upon creation, the sink particle is assigned an accretion radius. SPH particles that lie within this radius are accreted on to the sink. We choose the radius by calculating the smoothing length, $h_{\rm SINK}$, of an SPH particle with density $\rho_{\rm SINK}$. The accretion radius is then set to $2h_{\rm SINK}$. This means that the radius of each sink should roughly match the size of the smoothing kernels of the highest density SPH particles in the simulation. For $\rho_{\rm SINK} = 0^{-9}\,{\rm g\,cm^3}$, we have $h_{\rm SINK} \approx 0.2\,{\rm AU}$.

When a sink particle accretes an SPH particle, the mass, linear momentum and angular momentum of the SPH particle is added to the sink. When calculating kernel softened gravitational forces, each sink is assumed to have a smoothing length of $h_{\rm SINK}$.

5.4 Summary

In this chapter we have outlined the numerical method used to model gas dynamics in the interstellar medium. Hydrodynamical forces, viscosity and self-gravity are modelled using the Seren implementation of SPH. Regions of gas which are sufficiently dense and gravitationally bound are replaced by sink particles. These are point masses which i) significantly shorten the time needed to run a simulation and ii) provide a convenient model of protostars.

Chapter 6

Constituent physics

In this chapter we detail the additional physics included with the standard formulation of SPH. We use the radiative transfer algorithm proposed by Stamatellos et al. (2007a) to follow the specific internal energy of each particle and solve the equation of state.

Radiative heating from gas accreting onto protostars is included in the simulations. This heats the surrounding gas and can suppress disc fragmentation. Here we outline the semi-empirical model of episodic accretion proposed by Stamatellos et al. (2011). Unlike continuous accretion, this involves short, intense accretion events interspersed with long periods of low luminosity, during which stars may form.

6.1 Radiative transfer

We use the method proposed by Stamatellos et al. (2007a) to model radiative transfer within SPH simulations. This method assumes that each SPH particle is embedded in a polytropic pseudo-cloud, the parameters of which are calibrated to properties of the SPH particle. A mean optical depth is calculated for each particle, and this is used to determine the heating or cooling rate.

The method captures thermal inertia effects without adding significant computational expense and has been extensively tested by Stamatellos et al. (2007a) and Stamatellos and Whitworth (2008). Although the method can give inaccurate cooling rates discs (Wilkins and Clarke, 2012), it works well within high-density fragments (Young et al., 2012).

In this section we provide an overview of the radiative transport calculations and how this method is used to solve the equation of state. Analysis of the method, including benchmarks, can be found in the original publication.

6.1.1 Pseudo-cloud

Each SPH particle is assumed to be embedded in a pseudo-cloud at radius $R = \xi R_{\rm O}$. The cloud has central density $\rho_{\rm C}$, scale-length $R_{\rm O}$ and polytropic index n, where ξ is a dimensionless radius. Values of $R_{\rm O}$ and $\rho_{\rm C}$ are chosen to reflect physical quantities attributed to the SPH particle, i.e.

$$\rho_{\rm C}\theta^n(\xi) = \rho_i\,, \tag{6.1}$$

$$-4\pi G\rho_{\rm C}R_{\rm O}^2\phi(\xi) = \Phi_i\,, \tag{6.2}$$

where ρ_i is the density of SPH particle and Φ_i is the gravitational potential at the position of the SPH particle. Here $\theta(\xi)$ is the Lane-Emden Function for a polytropic index of n (Chandrasekhar, 1939),

$$\phi(\xi) = -\xi_{\rm B}\frac{{\rm d}\theta}{{\rm d}\xi}(\xi_{\rm B}) + \theta(\xi)\,, \tag{6.3}$$

and $\xi_{\rm B}$ is the dimensionless boundary of the polytrope. By fixing n and choosing a value of $\xi \leq \xi_{\rm B}$, we have

$$\rho_{\rm C} = \rho_i\theta^{-n}(\xi)\,, \tag{6.4}$$

$$R_{\rm O} = \sqrt{-\frac{\Phi_i\theta^n(\xi)}{4\pi G\rho_i\phi(\xi)}}\,. \tag{6.5}$$

The central temperature of the pseudo-cloud is then chosen to reflect the actual temperature of the SPH particle, i.e.

$$T_{\rm C} = T_i\theta^{-1}(\xi)\,. \tag{6.6}$$

The radial column-density from dimensionless radius ξ to $\xi_{\rm B}$ is given by

$$\begin{aligned}\Sigma_i(\xi) &= \int_{\xi'=\xi}^{\xi'=\xi_{\rm B}} \rho_{\rm C}\theta^n(\xi')R_{\rm O}\,{\rm d}\xi' \\ &= \sqrt{-\frac{\Phi_i\rho_i}{4\pi G\phi(\xi)\theta^n(\xi)}}\int_{\xi'=\xi}^{\xi'=\xi_{\rm B}} \theta^n(\xi')\,{\rm d}\xi'\,.\end{aligned} \tag{6.7}$$

The pseudo-mean column-density is therefore a mass weighted average of $\Sigma_i(\xi)$ over

all values of ξ, i.e.

$$\begin{aligned}\bar{\Sigma}_i &= \left[-\xi_{\rm B}^2\frac{{\rm d}\theta}{{\rm d}\xi}(\xi_{\rm B})\right]^{-1}\int\limits_{\xi=0}^{\xi=\xi_{\rm B}}\Sigma_i(\xi)\theta n(\xi)\xi^2\,{\rm d}\xi \\ &= \zeta_n\sqrt{-\frac{\Phi_i\rho_i}{4\pi G}}\,,\end{aligned} \tag{6.8}$$

where $-\xi_{\rm B}^2\frac{{\rm d}\theta}{{\rm d}\xi}(\xi_{\rm B})$ is the dimensionless mass of the pseudo cloud and

$$\zeta_n = \left[-\xi_{\rm B}^2\frac{{\rm d}\theta}{{\rm d}\xi}(\xi_{\rm B})\right]^{-1}\int\limits_{\xi=0}^{\xi=\xi_{\rm B}}\int\limits_{\xi'=\xi}^{\xi'=\xi_{\rm B}}\theta^n(\xi')\sqrt{\frac{\theta^n(\xi)}{\phi(\xi)}}\xi^2\,{\rm d}\xi'{\rm d}\xi\,. \tag{6.9}$$

As suggested by Stamatellos et al. (2007a), we adopt $n = 2$.

The optical depth is calculated by integrating the Rosseland-mean opacity along the radial line from ξ to $\xi_{\rm B}$, i.e.

$$\begin{aligned}\tau_i(\xi) &= \int\limits_{\xi'=\xi}^{\xi'=\xi_{\rm B}}\kappa_{\rm R}(\rho_{\rm C}\theta^n(\xi'),T_{\rm C}\theta(\xi'))\rho_{\rm C}\theta^n(\xi')R_{\rm O}\,{\rm d}\xi' \\ &= \sqrt{-\frac{\Phi_i\rho_i\theta^n(\xi)}{4\pi G\phi(\xi)}}\int\limits_{\xi'=\xi}^{\xi'=\xi_{\rm B}}\kappa_{\rm R}\left(\rho_i\left[\frac{\theta(\xi')}{\theta(\xi)}\right]^n,T_i\left[\frac{\theta(\xi')}{\theta(\xi)}\right]\right)\left[\frac{\theta(\xi')}{\theta(\xi)}\right]^n{\rm d}\xi'\,.\end{aligned} \tag{6.10}$$

where $\kappa_{\rm R}(\rho,T)$ is the local Rosseland-mean opacity. The pseudo-mean optical depth is obtained by averaging $\tau_i(\xi)$ over all values of ξ, i.e.

$$\begin{aligned}\bar{\tau}_i &= \left[-\xi_{\rm B}^2\frac{{\rm d}\theta}{{\rm d}\xi}(\xi_{\rm B})\right]^{-1}\sqrt{-\frac{\Phi_i\rho_i}{4\pi G}} \\ &\times\int\limits_{\xi=0}^{\xi=\xi_{\rm B}}\int\limits_{\xi'=\xi}^{\xi'=\xi_{\rm B}}\kappa_{\rm R}\left(\rho_i\left[\frac{\theta(\xi')}{\theta(\xi)}\right]^n,T_i\left[\frac{\theta(\xi')}{\theta(\xi)}\right]\right)\theta^n(\xi')\sqrt{\frac{\theta^n(\xi)}{\phi(\xi)}}\xi^2\,{\rm d}\xi'{\rm d}\xi\,.\end{aligned} \tag{6.11}$$

By defining the pseudo-mean mass opacity:

$$\bar{\kappa}_{{\rm R},i} = \frac{\bar{\tau}_i}{\bar{\Sigma}_i}\,, \tag{6.12}$$

it can be evaluated as

$$\bar{\kappa}_{\rm R}(\rho,T) = \left[-\zeta_n \xi_{\rm B}^2 \frac{{\rm d}\theta}{{\rm d}\xi}(\xi_{\rm B})\right]^{-1} \times \int_{\xi=0}^{\xi=\xi_{\rm B}} \int_{\xi'=\xi}^{\xi'=\xi_{\rm B}} \kappa_{\rm R}\left(\rho_i \left[\frac{\theta(\xi')}{\theta(\xi)}\right]^n, T_i \left[\frac{\theta(\xi')}{\theta(\xi)}\right]\right) \theta^n(\xi') \sqrt{\frac{\theta^n(\xi)}{\phi(\xi)}} \xi^2 \, {\rm d}\xi' {\rm d}\xi \,. \tag{6.13}$$

Note that if n is fixed, then $\bar{\kappa}_{\rm R}(\rho,T)$ is purely a function of ρ and T. Therefore, solutions to Equation (6.13) can be stored in a dense lookup table without the need for re-evaluations at each timestep. The variation of $\kappa_{\rm R}(\rho,T)$ with ρ and T is shown in Figure 6.2 .

6.1.2 Radiative heating and cooling

The rate of change of the specific internal energy of an SPH particle through radiative heating and cooling is given by

$$\left.\frac{{\rm d}u_i}{{\rm d}t}\right|_{\rm RAD} = \frac{4\sigma_{\rm SB}(T_{\rm O}(\boldsymbol{r}_i)^4 - T_i^4)}{\bar{\Sigma}_i^2 \bar{\kappa}_{\rm R}(\rho_i,T_i) + \kappa_{\rm P}^{-1}(\rho_i,T_i)} \,, \tag{6.14}$$

where $\kappa_{\rm P}(\rho_i,T_i)$ is the Planck-mean opacity and $T_{\rm O}$ is the background temperature field. In this thesis, we assume the background temperature arises from the combination of an ambient background radiation field and the luminosity from protostars. Therefore at any point $\boldsymbol{r}$ in space, the background temperature is given by

$$T_{\rm O}^4(\boldsymbol{r}) = T_{\rm AMB}^4 + \sum_{i=1}^{N_\star} \frac{L_{\star,i}}{16\pi\sigma_{\rm SB}|\boldsymbol{r} - \boldsymbol{r}_{\star,i}|^2} \,, \tag{6.15}$$

Where $T_{\rm AMB}$ is the ambient background temperature, $L_\star$ is the luminosity of a protostar and $\boldsymbol{r}_\star$ is its position. In keeping with the temperature estimates by Stamatellos et al. (2007c), we set $T_{\rm AMB} = 10\,{\rm K}$.

6.1.3 Quasi-implicit scheme

The specific internal energy of each particle, u_i, is updated using a quasi-implicit scheme. This accounts for thermal inertia effects without the need for very for small timesteps. First, the equilibrium temperature, $T_{{\rm EQ},i}$, is calculated from

$$\left.\frac{{\rm d}u_i}{{\rm d}t}\right|_{\rm HYDRO} + \left.\frac{{\rm d}u_i}{{\rm d}t}\right|_{\rm VISC} + \frac{4\sigma_{\rm SB}(T_{\rm O}(\boldsymbol{r}_i)^4 - T_{{\rm EQ},i}^4)}{\bar{\Sigma}_i^2 \bar{\kappa}_{\rm R}(\rho_i,T_i) + \kappa_{\rm P}^{-1}(\rho_i,T_i)} = 0 \,. \tag{6.16}$$

From this, the thermalisation time scale is calculated to be

$$t_{\mathrm{THERM},i} = (u_{\mathrm{EQ},i} - u_i) \left(\left.\frac{\mathrm{d}u_i}{\mathrm{d}t}\right|_{\mathrm{HYDRO}} + \left.\frac{\mathrm{d}u_i}{\mathrm{d}t}\right|_{\mathrm{VISC}} + \left.\frac{\mathrm{d}u_i}{\mathrm{d}t}\right|_{\mathrm{RAD}} \right)^{-1} . \tag{6.17}$$

Here $u_{\mathrm{EQ}} = u(T_{\mathrm{EQ},i}\,, \rho_i)$ and its calculation is given in Section 6.1.6. The value of u_i is then advanced through timestep Δt:

$$u_i(t + \Delta t) = u_i(t) \exp\left(\frac{-\Delta t}{t_{\mathrm{THERM},i}}\right) + u_{\mathrm{EQ},i} \left[1 - \exp\left(\frac{-\Delta t}{t_{\mathrm{THERM},i}}\right)\right] . \tag{6.18}$$

This method accounts for thermal inertia effects without the need for very for small timesteps.

6.1.4 Implementation

In summary, for each particle i at each timestep, the following steps are taken:

1. Calculate the pseudo-mean column-density $\bar{\Sigma}_i$ from ρ_i, Φ_i and T_i using Equation (6.8).
2. Calculate the pseudo-mean opacity $\bar{\kappa}_{\mathrm{R}}(\rho_i, T_i)$ and Planck-mean opacity $\kappa_{\mathrm{A}}(\rho_i, T_i)$ (This is performed using lookup tables. The variation of opacity with density and temperature is shown in Section 6.1.7).
3. Calculate the radiative heating rate $\mathrm{d}u_i/\mathrm{d}t|_{\mathrm{RAD}}$ using Equation (6.14).
4. Calculate the equilibrium temperature, $T_{\mathrm{EQ},i}$, using Equation (6.16) and thermalisation time scale $t_{\mathrm{THERM},i}$ using Equation (6.17).
5. Advance u_i over the timestep using Equation (6.18); From u_i, also update T_i (The relationship between u_i and T_i is given in Section 6.1.6).

6.1.5 Equation of state

The equation of state is determined almost entirely by the gas-phase chemistry of hydrogen and helium. We assume that the gas is 70% hydrogen and 30% helium, i.e. $X = 0.7$, $Y = 0.3$ and $Z = 0$. By defining $y = n_{\mathrm{H^o}}/2n_{\mathrm{H_2}}$ as the dissociation fraction of hydrogen and $x = n_{\mathrm{H^+}}/n_{\mathrm{H^o}}$, $z_2 = n_{\mathrm{He^{++}}}/n_{\mathrm{He^+}}$, $z_1 = n_{\mathrm{He^+}}/n_{\mathrm{He^o}}$ as the ionisation fractions of hydrogen, neutral helium and singly ionised helium, the mean molecular weight is given by

$$\mu_i = \mu(\rho_i, T_i) = \left[(1 + y_i + 2x_i y_i)\frac{X}{2} + (1 + z_{1,i} + z_{1,i}z_{2,i})\frac{Y}{4}\right]^{-1} . \tag{6.19}$$

The parameters x_i, y_i, $z_{1,i}$ and $z_{2,i}$ depend on ρ_i and T_i and are calculated using the Saha Equations. The variation of μ_i with ρ_i and T_i is shown in Figure 6.1. The gas pressure is then given by

$$P_i = \frac{\rho_i k_{\rm B} T_i}{\mu_i m_{\rm H}}\,, \tag{6.20}$$

assuming that the fluid behaves as an ideal gas.

6.1.6 Specific internal energy

The total specific internal energy of an SPH particle is the sum of the specific internal energies of molecular hydrogen, atomic hydrogen, ionised hydrogen, neutral helium, singly ionised helium and doubly ionised helium, as well as contributions from dissociation and ionisation energies, i.e.

$$u_i = u_{\rm H_2} + u_{\rm H} + u_{\rm He} + u_{\rm H_2\,DISS} + u_{\rm H\,ION} + u_{\rm He\,ION} + u_{\rm He^+\,ION}\,, \tag{6.21}$$

where

$$u_{\rm H_2} = X(1-y_i)\left[\frac{3}{2} + c(T_i)\right]\frac{k_{\rm B}T_i}{2m_{\rm H}}\,, \tag{6.22}$$

$$u_{\rm H} = Xy_i(1+x_i)\frac{3k_{\rm B}T_i}{2m_{\rm H}}\,, \tag{6.23}$$

$$u_{\rm He} = Y(1+z_{1,i}+z_{1,i}z_{2,i})\frac{3k_{\rm B}T_i}{8m_{\rm H}}\,, \tag{6.24}$$

$$u_{\rm H_2\,DISS} = Xy_i\frac{\mathcal{D}_{\rm H_2\,DISS}}{2m_{\rm H}}\,, \tag{6.25}$$

$$u_{\rm H\,ION} = Xx_iy_i\frac{\mathcal{I}_{\rm H\,ION}}{m_{\rm H}}\,, \tag{6.26}$$

$$u_{\rm He\,ION} = Yz_{1,i}(1-z_{2,i})\frac{\mathcal{I}_{\rm He\,ION}}{4m_{\rm H}}\,, \tag{6.27}$$

$$u_{\rm He^+\,ION} = Yz_{1,i}z_{2,i}\frac{\mathcal{I}_{\rm He^+\,ION}}{4m_{\rm H}}\,. \tag{6.28}$$

Here $\mathcal{D}_{\rm H_2} = 4.5\,{\rm eV}$ is the dissociation energy of hydrogen, $\mathcal{I}_{\rm H\,ION} = 13.6\,{\rm eV}$ is the ionisation energy of hydrogen, $\mathcal{I}_{\rm He\,ION} = 24.6\,{\rm eV}$ is the first ionisation energy of helium and $\mathcal{I}_{\rm He^+\,ION} = 54.5\,{\rm eV}$ is the second ionisation energy of helium. The function $c(T)$ is given by

$$c(T) = \left(\frac{T_{\rm ROT}}{T}\right)^2 f(T) + \left(\frac{T_{\rm VIB}}{T}\right)^2 \frac{\exp(T_{\rm VIB}/T)}{[\exp(T_{\rm VIB}/T)-1]^2}\,, \tag{6.29}$$

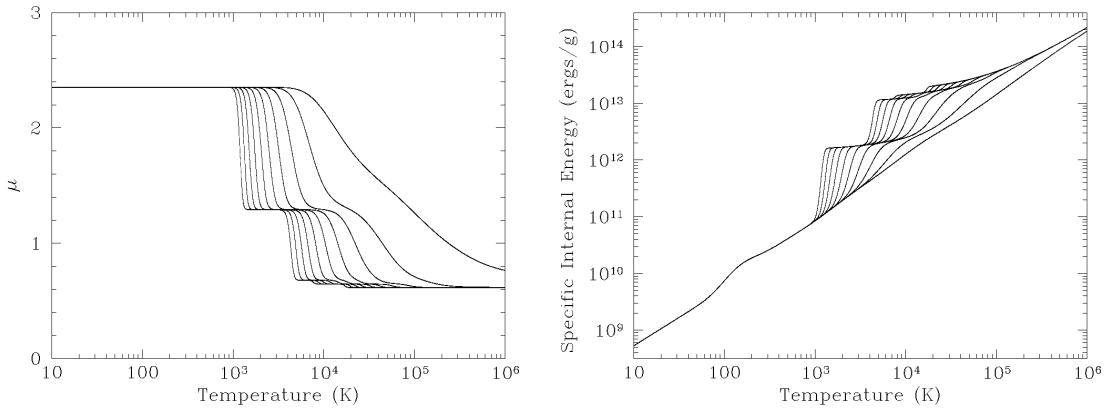

Figure 6.1: Left: Mean molecular weight versus temperature. Right: Specific internal energy versus temperature. From top to bottom, isopycnic curves have density $\rho = 10^{-18}\,\mathrm{g\,cm^{-3}}$ to $\rho = 1\,\mathrm{g\,cm^{-3}}$, with a spacing of two orders of magnitude. Figures taken from Stamatellos et al. (2007a).

where $T_{\mathrm{ROT}} = 85.4\,\mathrm{K}$ and $T_{\mathrm{VIB}} = 6100\,\mathrm{K}$. These are the temperatures at which the rotational and vibrational degrees of freedom of molecular hydrogen start to excite. The function $f(T)$ depends of the relative abundances of ortho- and para-H_2. This ratio is assumed to be $3:1$ for all T.

Equation (6.21) can be used to build an internal energy lookup table of $u(\rho, T)$. This function is shown in Figure 6.1. Furthermore, it can be inverted to give temperature $T(\rho, u)$, which is used to update an SPH particle's temperature.

6.1.7 Opacity

The opacity is calculated using the parametrisation proposed by (Bell and Lin, 1994):

$$\kappa_{\mathrm{R}}(\rho, T) = \kappa_{\mathrm{P}}(\rho, T) = \kappa_0 \rho^a T^b \,. \tag{6.30}$$

Here κ_0, a and b are constants that depend on the dominant source of opacity. This varies for different regimes of temperature and density. The values of these parameters are given in Table 6.1 and the dependence of mean opacity on temperature and density is shown in Figure 6.2.

At low temperatures, the opacity is dominated by ice grains which evaporate at $T \sim 150\,\mathrm{K}$. For temperatures between $150\,\mathrm{K} \lesssim T \lesssim 1,000\,\mathrm{K}$, the opacity is largely due the the presence of metal grains. After the metal grains evaporate out, the opacity falls steeply between temperatures $1,000\,\mathrm{K} \lesssim T \lesssim 2,000\,\mathrm{K}$. In this temperature regime, the opacity is mainly from molecules, as it is too hot for dust to exist and too cool for H^- absorption to occur. This region of low opacity is known

Table 6.1: Opacity law parameters, taken from Bell and Lin (1994).

Physical process	κ_0 $(\mathrm{cm}^{(2-3a)}\,\mathrm{g}^{-(1+a)}\,\mathrm{K}^{-b})$	a	b
Ice grains	2×10^{-4}	0	2
Evaporation of ice grains	2×10^{16}	0	-7
Metal grains	0.1	0	1/2
Evaporation of metal grains	2×10^{81}	1	-24
Molecules	10^{-8}	2/3	3
H^- absorption	10^{-36}	1/3	10
bf and ff transitions	1.5×10^{20}	1	-5/2
Electron scattering	0.348	0	0

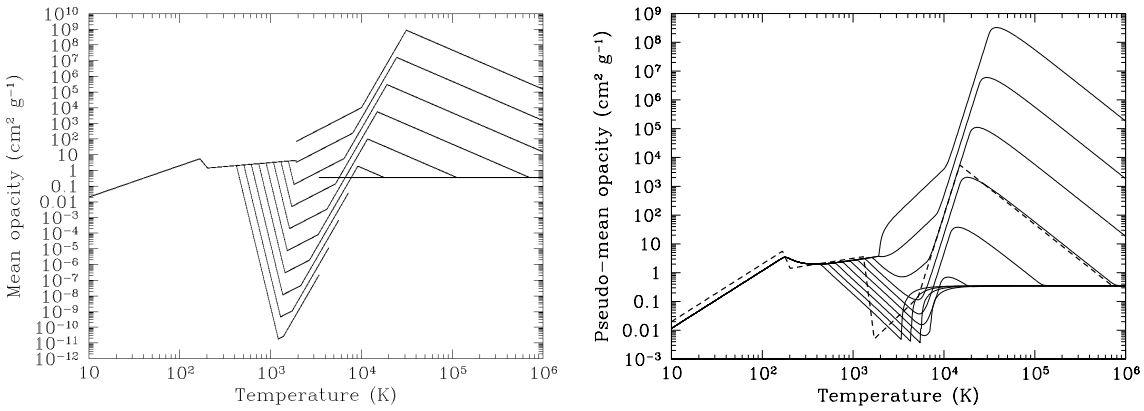

Figure 6.2: Left: *local* Rosseland-mean opacity versus temperature. Right: *pseudo-mean* Rosseland-mean opacity versus temperature. From top to bottom, isopycnic curves have density $\rho = 10^{-18}\,\mathrm{g\,cm^{-3}}$ to $\rho = 1\,\mathrm{g\,cm^{-3}}$, with a spacing of two orders of magnitude. This dashed line on the right is the *local* opacity at $\rho = 10^{-6}\,\mathrm{g\,cm^{-3}}$. Figures taken from Stamatellos et al. (2007a).

as the *opacity gap*. At temperatures between $2,000\,\mathrm{K} \lesssim T \lesssim 10,000\,\mathrm{K}$ the opacity rises again due to H^- absorption. At higher temperatures the opacity is dominated by free-free transitions, and by electron scattering at very high temperatures.

The variation of the *pseudo-mean* Rosseland-mean opacity with temperature and density is also shown in Figure 6.2. Here we see that the opacity gap is not as pronounced as it is for the *local* Rosseland-mean opacity. This is because an element of gas occupying the opacity gap is likely to be shielded by cooler material.

6.2 Accretion luminosity

Until recently, the effects of radiative feedback from protostars in simulations of star formation were ignored (e.g. Bate, 2009a), largely due to the computational difficulties of modelling radiative transport. However, accretion of material onto protostars can produce high luminosities (potentially up to $\sim 100\,\mathrm{L}_{\odot}$), so the feedback is likely to have a strong effect on the star formation process.

For a protostar with mass $M_{\star}$, radius $R_{\star}$ and accretion rate $\dot{M}_{\star}$, the luminosity is given by

$$\mathrm{L}_{\star} \approx \left(\frac{M_{\star}}{\mathrm{M}_{\odot}}\right)^{3} \mathrm{L}_{\odot} + f\frac{GM_{\star}\dot{M}_{\star}}{R_{\star}}\,. \tag{6.31}$$

Here $f = 0.75$ is the the amount of energy radiated away at the surface of the protostar. The rest is assumed to drive winds and jets (Offner et al., 2009). In this thesis we will assume that each protostar has a typical radius of $R_{\star} = 3\,\mathrm{R}_{\odot}$ (Palla and Stahler, 1993).

Recent studies have been undertaken which include radiative heating from *continuous* accretion (e.g. Bate, 2009c; Krumholz, 2006; Krumholz et al., 2010; Offner et al., 2009, 2010; Urban et al., 2010). The accretion rate onto the protostar is assumed to be equal to the accretion rate onto the sink-particle. (Bate, 2009c; Offner et al., 2009) note that as protostellar discs are heated, they become stable against fragmentation and fail to produce low mass stars.

6.2.1 Episodic accretion

There is growing observational evidence that suggests accretion is *episodic* instead of *continuous*, i.e. it occurs intermittently in short, intense outbursts (e.g. Dopita, 1978; Greene et al., 2008; Hartmann and Kenyon, 1996; Herbig, 1977; Reipurth, 1989). In particular, FU Ori-type stars (e.g. Green et al., 2011; Greene et al., 2008; Herbig, 1977; Peneva et al., 2010) exhibit large increases in their brightness that last for tens to hundreds of years.

The physical cause of episodic accretion is unclear. Candidate mechanisms include gravitational interactions within small N systems (e.g. Bonnell and Bastien, 1992; Forgan and Rice, 2010), thermal or gravitational instabilities within accretion discs (e.g. Bell and Lin, 1994; Hartmann and Kenyon, 1985; Machida et al., 2011; Vorobyov and Basu, 2005) or a combination of gravitational and magneto-rotational instabilities within discs (e.g. Martin and Lubow, 2011; Martin et al., 2012a,b; Zhu et al., 2007, 2009a, 2010a, 2009b, 2010b).

We adopt the numerical method proposed by Stamatellos et al. (2011, 2012),

based on work by Zhu et al. (2007, 2009a, 2010a, 2009b, 2010b) which models the effects of gravitational and magneto-rotational instabilities (MRI) in discs. Here, a protostar has an outer accretion disc which is cool enough to form spiral arms from gravitational instabilities. These arms transport angular momentum outwards from the disc, while material flows inwards. Conversely, there is an inner accretion disc (IAD) which is too hot for gravitational instabilities to form. However, when the gas in the IAD is sufficiently heated, it ionises and couples with the local magnetic field. The MRI then activates and angular momentum is transported outwards, allowing the material in the IAD to rapidly accrete onto the protostar. Once most of the material has left the IAD, the gas cools down and the episode resets.

6.2.2 Time dependent model

In this thesis we use SPH to model the physics of the outer accretion disc and the semi-empirical model by Stamatellos et al. (2011, 2012) to model the physics of the IAD. Here, each sink represents a protostar with an inner disc (the disc is assumed to exist, but not explicitly modelled in the simulation). The mass of sink particle is therefore equal to

$$M_{\rm SINK} = M_\star + M_{\rm IAD}\,, \tag{6.32}$$

where $M_\star$ is the protostellar mass and $M_{\rm IAD}$ is the mass of the IAD. It is assumed that the accretion rate of material from the IAD onto the protostar is given by

$$\dot{M}_\star = \dot{M}_{\rm BRG} + \dot{M}_{\rm MRI}\,, \tag{6.33}$$

where $\dot{M}_{\rm MRI}$ is accretion rate from the MRI and $\dot{M}_{\rm BRG}$ is the quiescent background accretion rate.

Models by Zhu et al. (2009a, 2010a, 2009b, 2010b) suggest that material within the IAD will couple to the magnetic field once the temperature reaches $T_{\rm MRI} \sim 1400\,{\rm K}$. Zhu et al. (2010b) estimate that the accretion rate during an outburst is roughly

$$\dot{M}_{\rm MRI} \sim 5 \times 10^{-4}\,{\rm M}_\odot \left(\frac{\alpha_{\rm MRI}}{0.1}\right) \tag{6.34}$$

where $\alpha_{\rm MRI}$ is the viscosity parameter. Zhu et al. (2010b) also estimate the duration of an outburst is roughly

$$\Delta t_{\rm MRI} \sim 0.25\,{\rm kyr} \left(\frac{\alpha_{\rm MRI}}{0.1}\right)^{-1} \left(\frac{M_\star}{0.2\,{\rm M}_\odot}\right)^{2/3} \left(\frac{\dot{M}_{\rm IAD}}{10^{-5}\,{\rm M}_\odot\,{\rm yr}^{-1}}\right)^{1/9}, \tag{6.35}$$

Here $\dot{M}_{\rm IAD}$ is the accretion rate of gas onto the sink particle (The gas is assumed to

immediately enter the IAD). The gas temperature of the IAD is assumed to reach $T_{\rm MRI}$ once the IAD has accumulated mass

$$\begin{aligned} M_{\rm IAD} > M_{\rm MRI} &\sim \dot{M}_{\rm MRI}\Delta t_{\rm MRI}\,, \\ &> 0.13\,{\rm M}_\odot \left(\frac{M_\star}{0.2\,{\rm M}_\odot}\right)^{2/3} \left(\frac{\dot{M}_{\rm IAD}}{10^{-5}\,{\rm M}_\odot\,{\rm yr}^{-1}}\right)^{1/9}\,. \end{aligned} \tag{6.36}$$

Once the mass of the IAD exceeds $M_{\rm MRI}$, an accretion outburst commences. The accretion rate of material from the IAD onto the protostar is given by

$$\dot{M}_{\rm MRI} = \frac{M_{\rm MRI}}{\Delta t_{\rm MRI}} \exp\left(-\frac{(t-t_0)}{\Delta t_{\rm MRI}}\right)\,,\; t_{\rm O} < t < t_{\rm O} + \Delta t_{\rm MRI}\,, \tag{6.37}$$

where $t_{\rm O}$ is the time at which the outburst starts. The outburst subsequently ceases once the time reaches $t_{\rm O} + \Delta t_{\rm MRI}$.

The time between each outburst required for the IAD to re-accumulate $M_{\rm MRI}$ is given by

$$\begin{aligned} \Delta t_{\rm ACC} &\sim \frac{M_{\rm MRI}}{\dot{M}_{\rm IAD}} \\ &\sim 13\,{\rm kyr} \left(\frac{M_\star}{0.2\,{\rm M}_\odot}\right)^{2/3} \left(\frac{\dot{M}_{\rm IAD}}{10^{-5}\,{\rm M}_\odot\,{\rm yr}^{-1}}\right)^{-8/9} \end{aligned} \tag{6.38}$$

If we assume that the bracketed terms in this equation are usually of order unity, this interval agrees with observations of young stellar objects by Scholz et al. (2013), who infer that $\Delta t_{\rm ACC} \sim 10^4\,{\rm yr}$ within limits of $5\times10^3\,{\rm yr} < \Delta t_{\rm ACC} < 5\times10^4\,{\rm yr}$.

The two parameters in this model, $\alpha_{\rm MRI}$ and $\dot{M}_{\rm BRG}$, are not well constrained. Indeed, it is probable that they vary from protostar to protostar. At present, observations and simulations suggest $0.01 < \alpha_{\rm MRI} < 0.4$ (e.g. Balbus and Hawley, 1998; Isella et al., 2009; King et al., 2007) and $10^{-11}\,{\rm M}_\odot\,{\rm yr}^{-1} < \dot{M}_{\rm BRG} < 10^{-6}\,{\rm M}_\odot\,{\rm yr}^{-1}$ (e.g. Calvet et al., 2004; Mohanty et al., 2005; Muzerolle et al., 2005; Natta et al., 2004). Stamatellos et al. (2012) demonstrate that parameter values of $\alpha_{\rm MRI} > 0.01$ and $\dot{M}_{\rm BRG} < 10^{-6}\,{\rm M}_\odot\,{\rm yr}^{-1}$ are required to allow disc fragmentation in the presence of radiative heating from accretion. In other words, $\dot{M}_{\rm MRI}$ needs to be at least three or four orders of magnitude greater than $\dot{M}_{\rm BRG}$ and $\Delta t_{\rm ACC}$ needs to be at least one or two orders of magnitude greater than $\Delta t_{\rm MRI}$.

We adopt the parameter values used by Stamatellos et al. (2011): $\alpha_{\rm MRI} = 0.1$ and $\dot{M}_{\rm BRG} = 10^{-7}\,{\rm M}_\odot\,{\rm yr}^{-1}$. We must note that future observations and simulations of young stars may tighten the constraints on $\alpha_{\rm MRI}$ and $\dot{M}_{\rm BRG}$. In that case, these

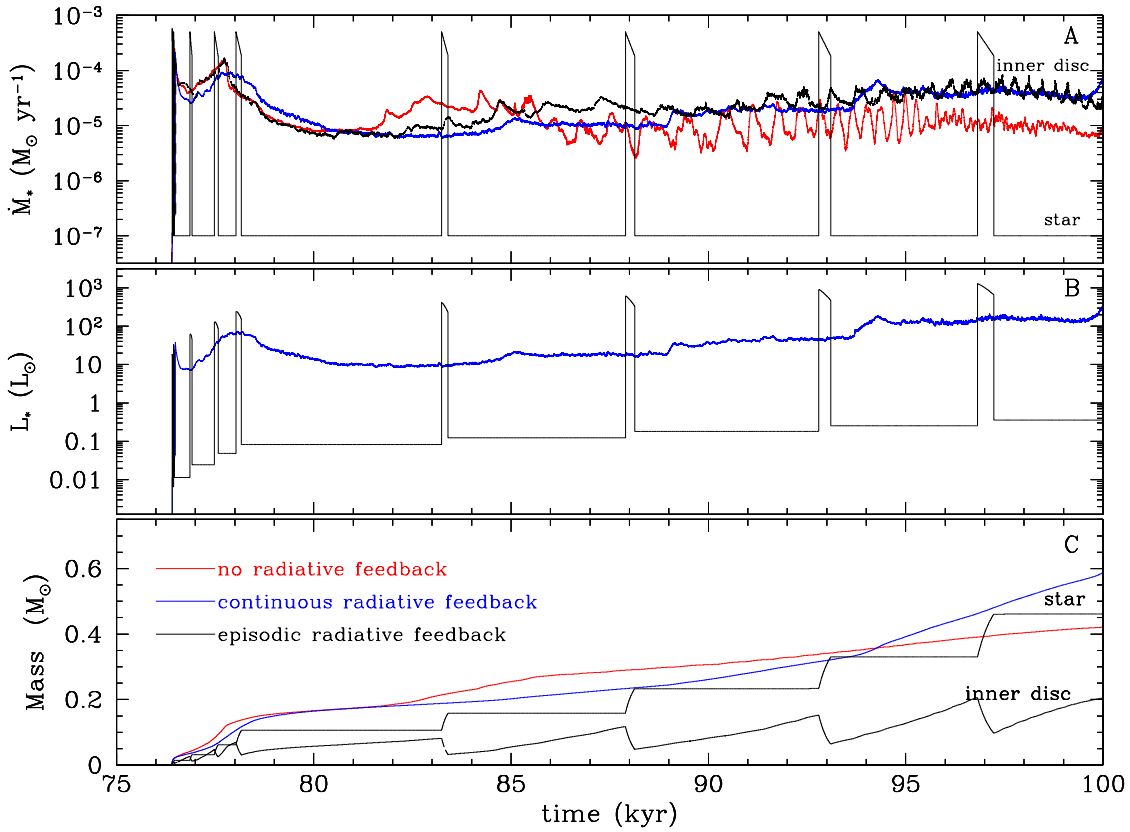

Figure 6.3: Evolution of a protostar and its IAD. Figure take from Stamatellos et al. (2011). Red lines are used for the case with accretion but no radiative feedback, blue lines for the case with continuous accretion feedback and black lines for the case with episodic accretion feedback. The top panel shows the accretion rate on to the sink; for episodic accretion, the accretion rate on to the star is also given. The middle panel shows the luminosity of the protostar. The bottom panel shows mass of the the sink; for episodic accretion, the mass is split into the mass of the star and the mass of the IAD. All three cases were taken from simulations with the same initial conditions.

adopted values may require revision.

Figure 6.3 shows the evolution of protostellar accretion rate and luminosity over time with the episodic accretion model. For comparison, the same quantities are plotted for a protostar with continuous accretion. Note that with the episodic model, there are extended periods of low luminosity when disc fragmentation may occur. With the continuous accretion model, the luminosity stays between $10\,\mathrm{L}_\odot \lesssim L \lesssim 100\,\mathrm{L}_\odot$ once accretion starts. At this luminosity, the gas within 100 AU of the protostar has a temperature of $T \sim 100\,\mathrm{K}$, which means disc fragmentation is unlikely.

6.3 Summary

In this chapter we have outlined the constituent physics included in addition to the standard formulation of SPH. Radiative heating is modelled by assuming that each particle is embedded in a polytropic pseudo-cloud with parameters set to SPH quantities. The mean optical depth through the pseudo-cloud is used to calculate heating or cooling rates.

We also include luminosity from protostellar accretion. This can be modelled as continuous accretion or episodic accretion. Continuous accretion as been shown to suppress star formation is discs whereas episodic accretion can allow stars to form during long periods of low luminosity.

There is a growing body of evidence in support of episodic accretion. However, the parameters that control the quiescent accretion rate and duration of the episodic outbursts are not well constrained. Indeed, these parameters may vary from protostar to protostar. We have adopted values that are supported by observations, albeit with large uncertainties.

Chapter 7

Setting up initial conditions

In this chapter we provide the technical details on how to set up simulations of prestellar cores. We tabulate the core masses, sizes and velocity dispersions taken from the lognormal distribution in Chapter 2, and core shapes from the model in Chapter 3. We also specify how we apply a critical Bonnor-Ebert density profile a turbulent velocity field, as given in Chapter 4 , to an ensemble of SPH particles. We finish by defining suites of simulations which have different accretion feedback and turbulence parameters.

7.1 Core parameters

We generate an ensemble of model cores with statistical properties similar to those defined in Ophiuchus. Each core is assigned a set of primary parameters which describe its global features, i.e. total mass $M_{\rm CORE}$, velocity dispersion $\sigma_{\rm NT}$, size $R_{\rm CORE}$ and intrinsic aspect ratios Q_B and Q_C.

In Chapter 2 we defined a lognormal distribution from which we can draw mass $M_{\rm OBS}$, size $R_{\rm OBS}$ and non-thermal velocity dispersion $\sigma_{\rm NT}$. Note that $M_{\rm OBS}$ and $R_{\rm OBS}$ are not the same as the final core masses and sizes. $R_{\rm OBS}$ is the size of the core's surface density full width at half maximum (FWHM). As a critical Bonnor-Ebert sphere also has a well defined surface density FWHM at $\frac{\xi_{\rm FWHM}}{\xi_{\rm CRIT}} = 0.413$, we define the core size as

$$R_{\rm CORE} = \frac{R_{\rm OBS}}{0.413} = 2.424\, R_{\rm OBS}\,. \tag{7.1}$$

We set $M_{\rm CORE} = 2M_{\rm OBS}$ to bring the core masses closer in line with the more recent Ophiuchus observations by Stanke et al. (2006). This is also close to observed core masses in other star forming regions (e.g. Könyves et al., 2010; Nutter and Ward-Thompson, 2007).

The core is modelled as a triaxial ellipsoid with semi-axes A, B and C. We draw intrinsic aspect ratios $Q_B = B/A$ and $Q_C = C/A$ from the shape fitting model **M1** in Chapter 3, with $\tau_0 = 0.6$. We now set the core axes to

$$\begin{aligned} A =& \frac{R_{\text{CORE}}}{(Q_B Q_C)^{\frac{1}{3}}}\,, \\ B =& Q_B\, A\,, \\ C =& Q_C\, A\,. \end{aligned} \tag{7.2}$$

Table 7.1 gives the list of primary parameters used to model all the simulations in this thesis. We also list the average density of the core and a notional free fall time, assuming a spherical core of radius R_{CORE} and mass M_{CORE}.

7.2 Internal structure

7.2.1 Settled glass

We randomly place 10^5 SPH particles in a periodic cube and use SEREN to settle the particles until the RMS difference in particle density is at most 0.3% (i.e. the denisty is approximately uniform). As the cube is periodic, it can be replicated along any of its dimensions in order to have more particles if necessary. For each core, we cut a uniform density ellipsoid with axis ratios Q_B and Q_C containing $M_{\text{CORE}}/M_{\text{SPH}}$ SPH particles from the cube (recall that $M_{\text{SPH}} = 10^{-5}\,\text{M}_\odot$). The size of the ellipsoid is finally scaled to the core axis lengths A, B and C.

7.2.2 Density profile

We apply the dimensionless mass function $\mu(\xi)$ from Section 4.1 to the uniform density ellipsoid by inverting the lookup Table to give $\xi(\mu)$. For each particle, we define the quantity

$$s_i = \sqrt{\frac{x_i^2}{A^2} + \frac{y_i^2}{B^2} + \frac{z_i^2}{C^2}}\,, \tag{7.3}$$

and make a list of all particles in ascending order of s_i. We assign each particle a cumulative mass

$$M_i = \sum_{k=1}^{i} m_k\,, \tag{7.4}$$

and apply the following transformation on each particle position $\boldsymbol{x_i}$:

$$\boldsymbol{x_i} \rightarrow \frac{\xi(\mu_i)}{\xi_{\text{CRIT}}} \boldsymbol{x_i}\,, \tag{7.5}$$

Table 7.1: Initial condition parameters drawn from Ophiuchus observations and shape fitting model. Column 1 gives the core number; column 2 gives the total mass of the core, column 3 gives the one-dimensional non-thermal velocity dispersion assigned to the core; column 4 gives the effective radius of the core where $R_{\rm CORE} = (A\,B\,C)^{\frac{1}{3}}$ and A, B and C are the semi-axes of an ellipsoid; column 5 gives the longest axis of the core; column 6 gives the intrinsic aspect ratio between the longest and intermediate axis of the core; column 7 gives the intrinsic aspect ratio between the longest and shortest axis of the core; column 8 gives the average density of the core; column 9 gives the notional free-fall time of the core where $t_{\rm FF} = (\frac{3\pi}{32\,G\,\bar{\rho}})^{\frac{1}{2}}$.

Core N	$M_{\rm CORE}$ ($\rm M_\odot$)	$\sigma_{\rm NT}$ ($\rm km\,s^{-1}$)	$R_{\rm CORE}$ (AU)	A	B/A	C/A	$\bar{\rho}$ ($10^{-17}\,\rm g\,cm^{-1}$)	$t_{\rm FF}$ (Myr)
1	0.478	0.066	2360	5045	0.333	0.308	0.516	0.029
2	0.809	0.135	2222	2722	0.906	0.601	1.045	0.021
3	1.881	0.122	6945	7728	0.947	0.766	0.080	0.075
4	0.096	0.172	2718	3887	0.657	0.520	0.068	0.081
5	0.169	0.090	2474	3961	0.538	0.453	0.159	0.053
6	0.110	0.069	2666	4320	0.508	0.463	0.082	0.073
7	1.425	0.179	8054	13833	0.525	0.376	0.039	0.107
8	2.999	0.098	13347	24006	0.586	0.294	0.018	0.157
9	0.540	0.132	3281	4193	0.864	0.554	0.217	0.045
10	2.358	0.176	3556	6121	0.508	0.386	0.744	0.024
11	1.307	0.160	3677	4087	0.917	0.794	0.373	0.034
12	0.164	0.110	1446	2581	0.510	0.345	0.769	0.024
13	0.088	0.023	1365	1611	0.975	0.625	0.492	0.030
14	1.532	0.268	4034	5119	0.948	0.516	0.331	0.037
15	1.160	0.203	8211	20024	0.306	0.225	0.030	0.122
16	1.606	0.140	6555	9715	0.629	0.488	0.081	0.074
17	0.330	0.063	3418	5890	0.566	0.345	0.117	0.062
18	0.368	0.127	2653	3084	0.811	0.785	0.279	0.040
19	0.230	0.092	859	915	0.930	0.892	5.137	0.009
20	0.889	0.085	2637	4919	0.704	0.219	0.687	0.025
21	3.020	0.271	2952	3839	0.943	0.482	1.665	0.016
22	0.951	0.125	2342	3427	0.737	0.433	1.049	0.021
23	1.427	0.072	2304	2551	0.865	0.852	1.655	0.016
24	0.231	0.185	1495	2676	0.729	0.239	0.979	0.021
25	0.104	0.118	557	1012	0.465	0.359	8.567	0.007
26	2.016	0.119	5326	9700	0.411	0.403	0.189	0.048
27	3.439	0.166	4715	8225	0.452	0.417	0.465	0.031
28	1.137	0.061	9459	10348	0.899	0.850	0.019	0.152
29	1.763	0.187	1927	4687	0.506	0.137	3.496	0.011
30	0.176	0.090	1007	1089	0.913	0.867	2.438	0.013
31	0.767	0.087	3722	8278	0.307	0.296	0.211	0.046

Initial condition parameters drawn from Ophiuchus observations and shape fitting model.

Core N	$M_{\rm CORE}$ ($M_\odot$)	$\sigma_{\rm NT}$ ($\rm km\,s^{-1}$)	$R_{\rm CORE}$ (AU)	A	Q_B	Q_C	$\bar{\rho}$ ($10^{-17}\,\rm g\,cm^{-1}$)	$t_{\rm FF}$ (Myr)
32	0.202	0.044	4095	6312	0.961	0.284	0.042	0.103
33	0.189	0.084	2874	7390	0.292	0.202	0.113	0.063
34	0.278	0.067	864	1112	0.780	0.601	6.111	0.009
35	1.772	0.162	3700	4143	0.973	0.732	0.496	0.030
36	1.698	0.201	4269	5263	0.789	0.676	0.310	0.038
37	0.235	0.091	2885	3246	0.888	0.791	0.139	0.056
38	1.506	0.141	2372	3564	0.563	0.523	1.600	0.017
39	0.426	0.124	4476	6444	0.645	0.519	0.067	0.081
40	1.240	0.198	3549	5082	0.643	0.530	0.393	0.034
41	0.518	0.147	2829	3381	0.934	0.628	0.324	0.037
42	0.823	0.083	5656	10628	0.485	0.311	0.065	0.083
43	1.059	0.056	3829	6401	0.567	0.377	0.268	0.041
44	0.287	0.079	1647	2194	0.720	0.588	0.911	0.022
45	0.773	0.071	4893	7223	0.651	0.477	0.094	0.069
46	0.161	0.118	1652	2687	0.487	0.477	0.508	0.030
47	0.364	0.123	2551	2773	0.958	0.812	0.311	0.038
48	0.138	0.070	768	1126	0.654	0.486	4.327	0.010
49	0.281	0.123	3075	6261	0.682	0.174	0.137	0.057
50	1.365	0.137	2792	2995	0.994	0.815	0.890	0.022
51	2.272	0.115	6165	9575	0.745	0.358	0.138	0.057
52	1.300	0.299	2905	4481	0.614	0.444	0.752	0.024
53	0.399	0.133	2681	4405	0.502	0.449	0.293	0.039
54	0.546	0.067	2600	3567	0.981	0.395	0.441	0.032
55	0.236	0.094	1877	2482	0.864	0.500	0.505	0.030
56	0.455	0.080	2930	3855	0.765	0.574	0.257	0.042
57	0.212	0.071	1527	1867	0.905	0.605	0.845	0.023
58	0.784	0.226	1763	2070	0.929	0.665	2.030	0.015
59	0.290	0.035	4279	5756	0.778	0.528	0.052	0.092
60	0.749	0.089	4664	9058	0.434	0.315	0.105	0.065
61	0.229	0.091	2989	3776	0.772	0.642	0.121	0.060
62	1.279	0.123	9222	10779	0.939	0.667	0.023	0.138
63	1.022	0.158	2397	3293	0.928	0.415	1.053	0.021
64	0.815	0.137	3742	4487	0.792	0.732	0.221	0.045
65	1.801	0.217	3981	8985	0.387	0.224	0.405	0.033
66	1.157	0.167	1373	2851	0.366	0.305	6.335	0.008
67	1.807	0.182	4214	7354	0.826	0.228	0.342	0.036
68	0.127	0.068	2644	2811	0.953	0.874	0.098	0.067
69	4.597	0.150	17103	25626	0.703	0.423	0.013	0.184
70	0.187	0.119	1931	2431	0.787	0.637	0.367	0.035

Initial condition parameters drawn from Ophiuchus observations and shape fitting model.

Core N	$M_{\rm CORE}$ ($\rm M_\odot$)	$\sigma_{\rm NT}$ ($\rm km\,s^{-1}$)	$R_{\rm CORE}$ (AU)	A	Q_B	Q_C	$\bar{\rho}$ ($10^{-17}\,\rm g\,cm^{-1}$)	$t_{\rm FF}$ (Myr)
71	0.622	0.356	1476	2322	0.699	0.368	2.744	0.013
72	0.442	0.090	4432	6119	0.761	0.499	0.072	0.078
73	2.173	0.323	6611	10977	0.745	0.293	0.107	0.064
74	0.037	0.077	1079	1418	0.684	0.644	0.413	0.033
75	0.424	0.085	4332	5173	0.841	0.699	0.074	0.077
76	0.357	0.087	1959	2463	0.826	0.609	0.673	0.026
77	0.290	0.080	967	1853	0.544	0.262	4.545	0.010
78	0.110	0.071	1073	1958	0.591	0.278	1.258	0.019
79	0.461	0.221	1214	2235	0.494	0.324	3.655	0.011
80	0.847	0.069	5071	7475	0.719	0.434	0.092	0.069
81	1.815	0.101	6481	8012	0.877	0.603	0.095	0.068
82	0.664	0.097	1077	1258	0.990	0.634	7.537	0.008
83	1.332	0.100	9262	15025	0.607	0.386	0.024	0.136
84	0.994	0.214	3394	5859	0.977	0.199	0.361	0.035
85	0.337	0.048	2805	4211	0.691	0.428	0.216	0.045
86	0.410	0.099	1980	2052	0.969	0.926	0.750	0.024
87	0.182	0.067	2042	5611	0.277	0.174	0.303	0.038
88	0.368	0.134	2551	3441	0.755	0.539	0.314	0.038
89	0.383	0.074	3464	4575	0.749	0.580	0.131	0.058
90	1.273	0.113	3135	4948	0.557	0.456	0.586	0.027
91	1.208	0.064	8357	18062	0.393	0.252	0.029	0.123
92	0.647	0.115	4163	5090	0.857	0.639	0.127	0.059
93	2.737	0.066	9102	10841	0.847	0.699	0.051	0.093
94	0.359	0.276	1384	2865	0.389	0.290	1.923	0.015
95	0.365	0.094	1262	1830	0.573	0.573	2.573	0.013
96	0.644	0.108	3642	5406	0.575	0.531	0.189	0.048
97	1.055	0.074	6965	10928	0.562	0.461	0.044	0.100
98	3.319	0.117	4889	8811	0.462	0.370	0.403	0.033
99	0.691	0.197	4088	8322	0.492	0.241	0.144	0.056
100	0.093	0.059	889	1324	0.640	0.474	1.885	0.015

where

$$\mu_i = \mu(\xi_{\rm CRIT})\frac{M_i}{M_{\rm TOT}}\,. \tag{7.6}$$

As seen in Figure 7.1, applying a density profile to settled cube of particles adds further noise to the SPH density. The SPH density is calculated from the $\mathcal{N}$ nearest neighbours and this value is altered when inter-particle distances are

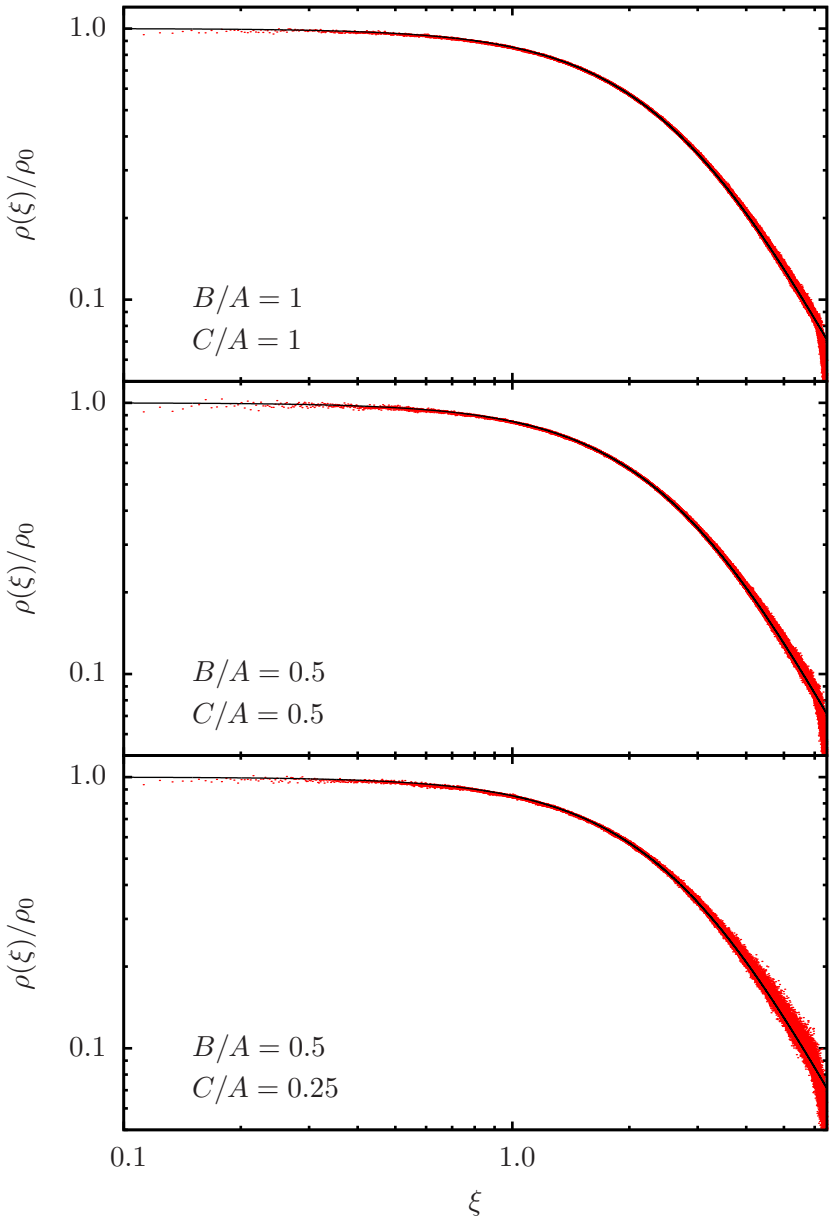

Figure 7.1: SPH particle densities after the application of a critical Bonnor-Ebert density profile. From top to bottom, the geometry of the system is spherical, a prolate spheroid with $(B/A = 0.5, C/A = 0.5)$ and a triaxial ellipsoid with $(B/A = 0.5, C/A = 0.25)$. The red dots show the SPH density of 10^5 particles and the black line shows the semi-analytical solution. In all cases, $\xi = s\xi_{\rm crit}$ where s is defined in Equation (7.3) and $\xi_{\rm crit} = 6.451$. The RMS deviation of the particle density from the solution is approximately 1.5% for the sphere, 2% for the prolate spheroid and 3% for the triaxial ellipsoid. In all cases, we only use SPH densities from the inner 95% of particles.

stretched or compressed. This effect is more apparent in triaxial ellipsoids than in spheres because of spatial anisotropy. We find that the average RMS density variation is about 3% for a triaxial ellipsoid with $Q_B = 0.5$, $Q_C = 0.25$ and $N_{\rm SPH} = 10^5$ compared to 1.5% for a sphere. Fortunately, this level of triaxiality represents an extreme in the core shapes and the 3% noise is significantly smaller than the order of magnitude difference between the core central density and boundary density.

7.2.3 Velocity field

We apply the velocity field given in Section 4.2 to the ensemble of particles. The velocity of each particle is calculated by interpolating the velocity of neighbouring grid-points to the particle position. As the grid is a cube of edge-length 2π and cores are triaxial, we define the dimensionless particle coordinates

$$\boldsymbol{s_i} = \frac{\pi}{2}\left(\frac{x_i}{A}, \frac{y_i}{B}, \frac{z_i}{C}\right) . \tag{7.7}$$

The particles' centre of mass is aligned with the centre of the cube and the particles are assigned velocities based on their dimensionless coordinates.

We subtract the bulk velocity and normalise each particle to the target velocity dispersion $\sigma_{\rm NT}$:

$$\boldsymbol{v}_i \rightarrow \frac{\sigma_{\rm NT}\,\boldsymbol{v}_i}{\sigma_v} , \tag{7.8}$$

where

$$\sigma_v = \sqrt{\frac{1}{N_{\rm SPH}}\sum_{i=1}^{N_{\rm SPH}} (\hat{\boldsymbol{u}}\cdot\boldsymbol{v}_i)^2} \tag{7.9}$$

and $\hat{\boldsymbol{u}}$ is a unit vector defining a random line of sight.

7.3 Simulation suites

We adopt the following naming scheme for individual core simulations:

`CORE ID = <CORE NUMBER>_<FEEDBACK MECHANISM>_<VELOCITY TYPE>`

The value of `CORE NUMBER` is taken from the core number column in Table 7.1. The label `FEEDBACK MECHANISM` states which mode of radiative feedback is being implemented. The value `NRF` denotes no radiative feedback, the value `CRF` denotes continuous radiative feedback and the value `ERF` denotes episodic radiative feedback. The label `VELOCITY TYPE` states which velocity modes are populated, as defined in Section 4.2.3 . The value `THR` denotes a thermal mix of 2:1 solenoidal to compressive

modes, the value SOL denotes purely solenoidal modes and the value COM denotes purely compressive modes. As an example, the core ID 008_CRF_COM identifies the simulation with parameters taken from the eighth row of Table 7.1 using continuous radiative feedback and a purely compressive velocity field.

We have nine different combinations of FEEDBACK MECHANISM and VELOCITY TYPE. We will run suites of simulations to model star formation using each of them. The number of individual simulations run in each suite is given in Table 7.2 .

Table 7.2: Number of simulations for different model parameters. The columns give different implementations of radiative feed back and the rows give different velocity fields. The contents of the table give the range of core parameters from Table 7.1 used in each suite.

	NRF	CRF	ERF
THR	1 - 100	1 - 100	1 - 100
SOL	1 - 50	1 - 50	1 - 50
COM	1 - 50	1 - 50	1 - 50

7.4 Summary

In this chapter we have tabulated the parameters used to the model prestellar cores. We have also described the methods used to apply Bonnor-Ebert density profiles and turbulent velocity fields to an ellipsoidal ensemble of particles.

We can now run batches of core simulations to statistically study core fragmentation and star formation. We model cores using the physical parameters listed in Table 7.1 and we repeat the simulations with i) different solenoidal to compressive velocity mode ratios and ii) different models of accretion feedback.

Chapter 8

Results

In this chapter we present and discuss the results of the simulations run using the initial conditions from Chapter 7. All cores were evolved for 2×10^5 yrs. We tabulate details of the sinks produced by each core and give mass functions from each simulation suite. We also calculate binary statistics from the sink particles, and compare the results with observations.

This chapter is split into three sections. In Section 8.1 we discuss the results of the simulations with $\Xi = 2$. These have a 2:1 mixture of of solenoidal to compressive velocity modes. In Section 8.2 we discuss the preliminary results of simulations with purely compressive ($\Xi = 0$) and purely solenoidal ($\Xi = \infty$) velocity fields. In both sections, we have repeated the simulations with no accretion feedback, episodic accretion feedback and continuous accretion feedback. We conclude this chapter in Section 8.3 where we give a summary of our findings.

8.1 Simulations with 2:1 turbulence: $\Xi = 2$

In this section we present and discuss the results of the simulations that have a 2:1 mixture of solenoidal and compressive turbulence. The simulations were run for 2×10^5 yrs. In Section 8.1.1 we present the masses of sink particles formed in the simulations. We will hereafter refer to the sinks as young stellar objects (YSOs). In Section 8.1.2 we provide a statistical comparison of the mass distribution of YSOs with the Chabrier (2005) IMF. In Section 8.1.4 we discuss the modes of core collapse and fragmentation that occur in the simulations. In Section 8.1.5 we analyse the binary statistics of the YSOs from the simulations and compare these with observations. Simulation snapshots in this chapter are rendered using SPLASH (Price, 2007).

8.1.1 Protostellar masses

Table 8.1 lists information on the sinks formed in simulations with $\Xi = 2$. These simulations were evolved for $t = 2 \times 10^5$ yrs. Sixty of the one hundred cores are prestellar. The remaining forty are omitted from the table. The first four columns give the core number, the mass of the core, $M_{\rm CORE}$, the ratio of thermal to gravitational energy, $\alpha_{\rm THERM}$, and the ratio of turbulent to gravitational energy $\alpha_{\rm TURB}$. The next three columns give the sum of YSO masses from each core, $\sum M_{\rm YSO}$, the number of stellar-mass objects $N_\star$ and the number of brown dwarf-mass objects $N_{\rm BD}$ formed when the YSOs have no radiative feedback (NRF). The next three columns give the same statistics when the YSOs have episodic radiative feedback (ERF) and the next three give statistics when the YSOs have continuous radiative feedback (CRF). We define 'stellar-mass' as $M > 0.08\,{\rm M}_\odot$ and 'brown dwarf-mass' as $M \leq 0.08\,{\rm M}_\odot$.

From the NRF simulations, we find that the cores have a mean star formation efficiency of 71%, and form on average 3.3 stars and 3.4 brown dwarfs per core. From the ERF simulations, the star formation efficiency remains at 71% and each core produces on average 3.1 stars and 1.5 brown dwarfs. The CRF simulations have a lower star formation efficiency of 59% and only produce 1.6 stars and 0.1 brown dwarfs per core.

Figure 8.1 shows the YSO mass functions produced from the simulations. Both the NRF and ERF simulations give a range of YSO masses from a few Jupiter masses to between one and two solar masses. The CRF simulations produce YSOs with roughly the same upper mass limit, however there are very few YSOs with masses less than $M \approx 0.05{\rm M}_\odot$.

Andersen et al. (2008) performed a survey of star forming regions and found that low mass stars outnumber brown dwarfs by a factor of

$$\mathcal{A} = \frac{N(0.08\,{\rm M}_\odot < M \leq 1.0\,{\rm M}_\odot)}{N(0.03\,{\rm M}_\odot < M \leq 0.08\,{\rm M}_\odot)} = 4.3 \pm 1.6\,. \tag{8.1}$$

From the simulations presented here, we obtain $\mathcal{A}_{\rm NRF} = 2.2$, $\mathcal{A}_{\rm ERF} = 3.9$ and $\mathcal{A}_{\rm CRF} = 17$ for NRF, ERF and CRF respectively. This demonstrates that simulations with CRF produce too few brown dwarfs to be considered realistic. Conversely, the ERF simulations reproduce the observed ratio to within one sigma of the observations. The NRF simulations give a ratio within two sigma of the observations.

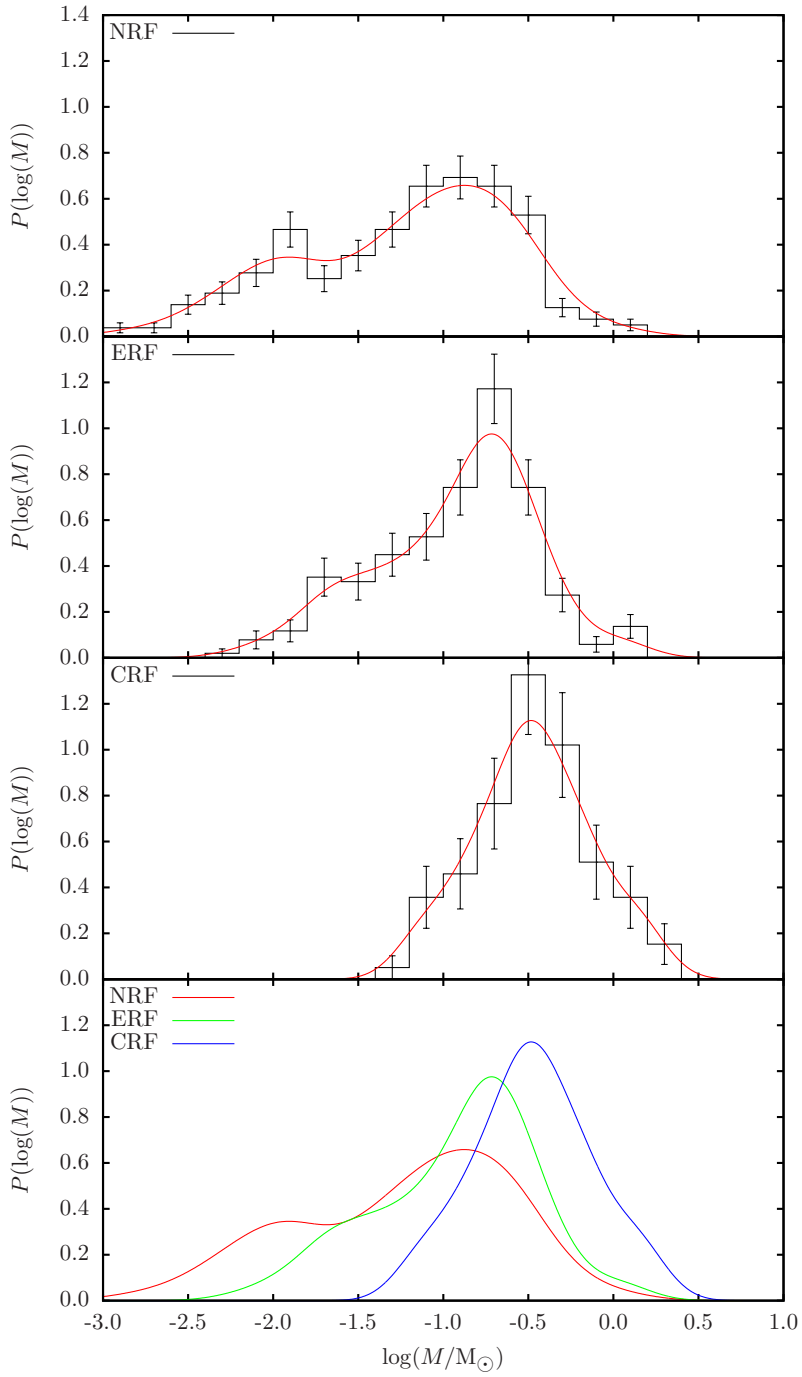

Figure 8.1: The YSO mass functions for simulations with $\Xi = 2$. The top three frames give the mass functions from simulations with NRF, ERF and CRF. The black histograms have bins equally spaced in $\log(M)$ and the red lines are kernel smoothed density functions (see Chapter 2, Section 2.2.5 for definition). The bottom fame shows the NRF, CRF and ERF density profiles on a single plot.

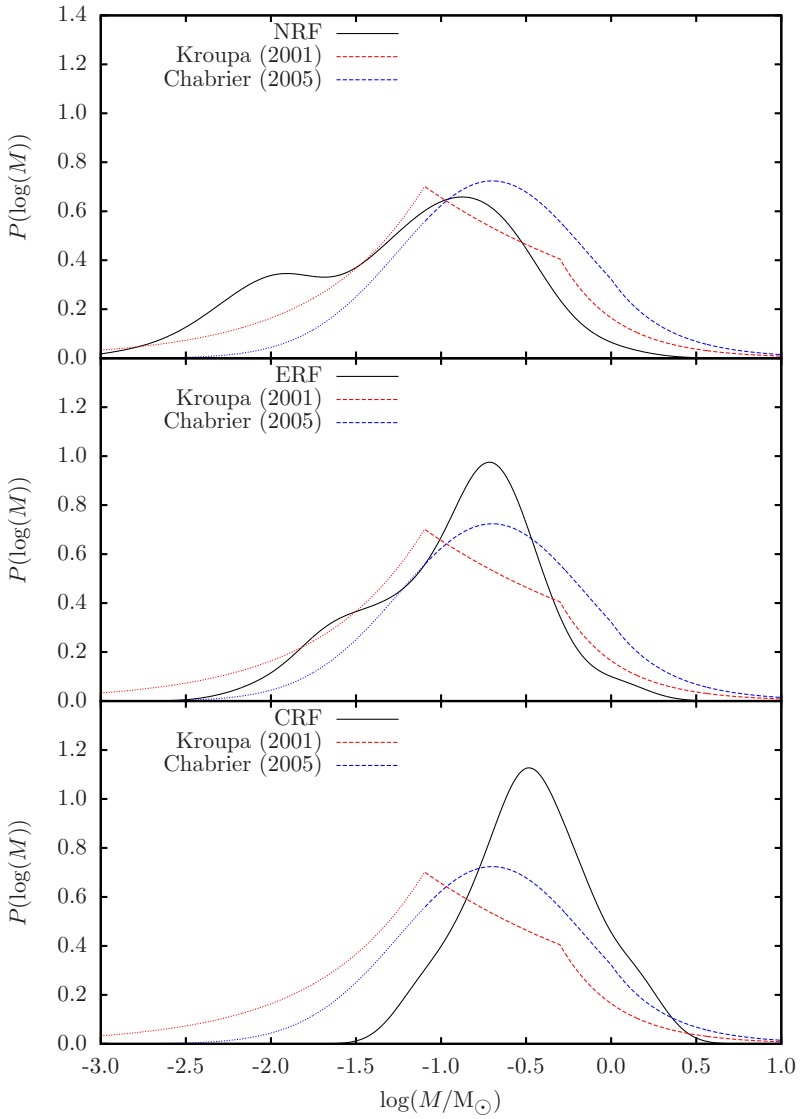

Figure 8.2: As Figure 8.1, but now the YSO mass functions (in black) are compared with the Kroupa (2001) and Chabrier (2005) IMFs (in red and blue respectively). The top frame shows the YSO mass function for NRF simulations, the middle frame for ERF and the bottom frame for CRF. The dashed part of the reference IMFs are in the stellar mass region with $M \geq 0.08\,\mathrm{M}_\odot$ whereas the dotted parts are in the brown dwarf mass region with $M < 0.08\,\mathrm{M}_\odot$. The brown dwarf region is not as well constrained as the stellar region. For all distributions $\int_{-\infty}^{+\infty} P(\log(M))\,\mathrm{d}\log(M) = 1$.

Table 8.1: The number of YSOs formed from each core simulation with $\Xi = 2$. Column 1 gives the core number, column 2 gives the core mass, column 3 gives the core's ratio of thermal to gravitational energy and column 4 gives the core's ratio of turbulent to gravitational energy. Columns 5, 6 and 7 give the total sink mass, the number of stellar-mass YSOs and the number of brown dwarf-mass YSOs formed with no radiative feedback from YSOs. Columns 8, 9 and 10 give the same quantities when there is episodic radiative feedback and columns 11, 12 and 13 give the quantities when there is continuous radiative feedback.

				NRF			ERF			CRF		
Core N	$M_{\rm CORE}$	$\alpha_{\rm THERM}$	$\alpha_{\rm TURB}$	$\sum M_{\rm YSO}$	$N_\star$	$N_{\rm BD}$	$\sum M_{\rm YSO}$	$N_\star$	$N_{\rm BD}$	$\sum M_{\rm YSO}$	$N_\star$	$N_{\rm BD}$
1	0.478	0.452	0.051	0.331	1	2	0.283	1	0	0.285	1	0
2	0.809	0.229	0.136	0.766	3	10	0.597	3	3	0.563	1	0
3	1.881	0.303	0.163	1.709	4	3	1.393	5	3	1.223	1	0
8	2.999	0.401	0.145	1.190	6	4	0.923	5	4	1.015	6	0
9	0.540	0.508	0.304	0.171	1	0	0.174	1	0	0.171	1	0
10	2.358	0.131	0.138	2.142	5	8	2.145	2	1	1.437	1	0
11	1.307	0.231	0.127	1.198	7	3	1.207	8	1	1.156	4	0
14	1.532	0.223	0.667	0.953	4	4	0.871	4	2	0.889	3	1
16	1.606	0.345	0.157	1.074	6	3	1.103	5	2	0.589	1	0
18	0.368	0.593	0.186	0.201	1	0	0.197	1	0	0.194	1	0
19	0.230	0.306	0.068	0.212	1	0	0.211	1	0	0.203	1	0
20	0.889	0.283	0.080	0.789	4	1	0.779	3	0	0.629	1	0
21	3.020	0.083	0.154	2.836	5	4	2.909	9	10	1.947	1	0
22	0.951	0.211	0.107	0.858	4	9	0.849	4	0	0.535	1	0

The number of YSOs formed from each core simulation with thermal turbulence.

Core N	$M_{\rm CORE}$	$\alpha_{\rm THERM}$	$\alpha_{\rm TURB}$	NRF			ERF			CRF		
				$\sum M_{\rm YSO}$	$N_\star$	$N_{\rm BD}$	$\sum M_{\rm YSO}$	$N_\star$	$N_{\rm BD}$	$\sum M_{\rm YSO}$	$N_\star$	$N_{\rm BD}$
23	1.427	0.132	0.016	1.404	1	3	1.321	1	0	1.331	1	0
25	0.104	0.472	0.238	0.068	0	1	0.067	0	1	0.059	0	1
26	2.016	0.232	0.186	1.322	5	5	1.124	4	2	0.649	1	0
27	3.439	0.119	0.102	3.037	7	3	2.858	5	7	2.597	3	0
29	1.763	0.114	0.145	0.000	0	0	1.655	5	0	1.483	3	0
31	0.767	0.450	0.092	0.531	3	0	0.508	3	2	0.389	1	0
34	0.278	0.259	0.025	0.256	1	0	0.254	1	0	0.249	1	0
35	1.772	0.172	0.094	1.688	4	10	1.685	5	2	1.308	1	0
36	1.698	0.208	0.201	1.460	8	10	1.450	7	0	1.277	5	1
38	1.506	0.133	0.049	1.492	3	5	1.366	1	0	1.379	1	0
40	1.240	0.241	0.181	1.120	4	0	1.097	4	1	0.847	2	0
41	0.518	0.454	0.386	0.139	1	0	0.139	1	0	0.129	1	0
43	1.059	0.314	0.021	0.922	4	3	0.792	2	0	0.786	1	0
44	0.287	0.479	0.119	0.191	1	1	0.161	1	0	0.154	1	0
45	0.773	0.536	0.079	0.467	4	1	0.448	3	1	0.330	1	0
47	0.364	0.576	0.208	0.148	1	0	0.147	1	0	0.137	1	0
48	0.138	0.470	0.047	0.108	1	0	0.105	1	0	0.100	1	0

The number of YSOs formed from each core simulation with thermal turbulence.

Core N	$M_{\rm CORE}$	$\alpha_{\rm THERM}$	$\alpha_{\rm TURB}$	NRF			ERF			CRF		
				$\sum M_{\rm YSO}$	$N_\star$	$N_{\rm BD}$	$\sum M_{\rm YSO}$	$N_\star$	$N_{\rm BD}$	$\sum M_{\rm YSO}$	$N_\star$	$N_{\rm BD}$
50	1.365	0.168	0.069	1.274	6	4	1.243	4	4	0.956	1	0
51	2.272	0.238	0.063	2.083	4	2	2.055	4	3	1.606	1	0
52	1.300	0.191	0.402	0.937	5	1	1.014	6	1	0.615	2	0
54	0.546	0.418	0.083	0.405	3	1	0.328	1	0	0.342	1	0
56	0.455	0.537	0.091	0.277	1	0	0.276	1	0	0.268	1	0
58	0.784	0.186	0.226	0.699	1	0	0.695	1	0	0.693	1	0
62	1.279	0.597	0.175	0.192	0	4	0.165	1	2	0.096	1	0
63	1.022	0.204	0.203	0.927	6	3	0.913	5	2	0.584	1	0
64	0.815	0.378	0.175	0.653	3	0	0.655	3	0	0.508	1	0
65	1.801	0.209	0.146	1.488	6	6	1.534	5	4	1.282	3	0
66	1.157	0.108	0.101	1.099	4	8	1.054	4	1	0.849	1	0
67	1.807	0.223	0.350	1.209	8	1	1.172	5	1	0.618	1	0
69	4.597	0.319	0.115	0.896	6	7	1.489	7	11	1.467	5	2
71	0.622	0.207	0.798	0.341	1	0	0.337	1	0	0.332	1	0
73	2.173	0.275	0.881	0.868	6	2	0.828	4	1	0.419	1	0
76	0.357	0.456	0.141	0.227	1	1	0.210	1	0	0.211	1	0
77	0.290	0.306	0.035	0.248	1	0	0.234	1	0	0.237	1	0

The number of YSOs formed from each core simulation with thermal turbulence.

				NRF			ERF			CRF		
Core N	$M_{\rm CORE}$	$\alpha_{\rm THERM}$	$\alpha_{\rm TURB}$	$\sum M_{\rm YSO}$	$N_\star$	$N_{\rm BD}$	$\sum M_{\rm YSO}$	$N_\star$	$N_{\rm BD}$	$\sum M_{\rm YSO}$	$N_\star$	$N_{\rm BD}$
79	0.461	0.234	0.554	0.246	0	5	0.228	2	0	0.179	1	0
80	0.847	0.512	0.060	0.439	1	0	0.450	1	0	0.451	1	0
81	1.815	0.297	0.126	1.509	5	3	1.266	5	3	1.309	5	0
82	0.664	0.135	0.031	0.634	1	0	0.633	1	0	0.629	1	0
83	1.332	0.603	0.146	0.296	1	4	0.312	2	3	0.145	1	0
86	0.410	0.395	0.113	0.322	1	4	0.284	2	0	0.260	1	0
90	1.273	0.210	0.054	1.059	5	2	1.188	5	2	0.825	1	0
93	2.737	0.274	0.047	2.427	6	6	2.402	4	6	1.662	1	0
95	0.365	0.291	0.104	0.329	1	4	0.274	1	0	0.282	1	0
96	0.644	0.478	0.118	0.466	1	5	0.363	1	0	0.378	1	0
97	1.055	0.563	0.100	0.521	3	3	0.540	3	0	0.449	1	0
98	3.319	0.129	0.074	2.596	8	34	3.142	8	2	2.977	5	0
Total	75.685			53.451	195	203	54.105	186	88	44.668	93	5

8.1.2 Comparison with the IMF

In Figure 8.2, we have plotted the YSO mass distributions from Figure 8.1 with the Kroupa (2001) (K01) and Chabrier (2005) (C05) parametrisations of the IMF. We shall focus the analysis on the C05 IMF, as the measurements are more recent than K01. The C05 IMF peaks at $M^{\rm C05}_{\rm PEAK} = 0.2\,{\rm M}_{\odot}$. We find that with NRF, ERF and CRF, the YSO mass distributions peak at $M^{\rm NRF}_{\rm PEAK} \approx 0.1\,{\rm M}_{\odot}$, $M^{\rm ERF}_{\rm PEAK} \approx 0.2\,{\rm M}_{\odot}$ and $M^{\rm CRF}_{\rm PEAK} \approx 0.4\,{\rm M}_{\odot}$ respectively. This suggests that the ERF simulations reproduce the most realistic distribution of masses, although it does not immediately rule out the other two.

We can provide a quantitative statement on the goodness of fit by calculating the likelihood of masses from C05 IMF being drawn from the simulated distributions of YSO masses. We assign the kernel smoothed density profiles shown in Figures 8.1 and 8.2 to model distributions $\mathbf{M}_{\rm NRF}$, $\mathbf{M}_{\rm ERF}$ and $\mathbf{M}_{\rm CRF}$. Each model has probability density function $P(\mathbf{D}|\mathbf{M})$. The likelihood of a star of mass D_i being drawn from model $\mathbf{M}$ is proportional to the probability density of $\mathbf{M}$ at mass D_i, i.e. $P(D_i|\mathbf{M})$. If we have a set of N stellar masses, $\mathbf{D}$, the likelihood of $\mathbf{D}$ being drawn from $\mathbf{M}$ is

$$P(\mathbf{D}|\mathbf{M}) \propto \prod_{i=1}^{N} P(D_i|\mathbf{M})\,. \tag{8.2}$$

The constants of proportionality are eliminated if we consider ratios

$$K_{j,k} = \frac{P(\mathbf{D}|\mathbf{M_j})}{P(\mathbf{D}|\mathbf{M_k})} = \prod_{i=1}^{N} \frac{P(D_i|\mathbf{M_j})}{P(D_i|\mathbf{M_k})}\,. \tag{8.3}$$

We draw observational data points D_i from the C05 IMF (defined Chapter 1, Section 1.1.5). These are used to look up the corresponding likelihoods $P(D_i|\mathbf{M})$[1]. We note that the value of $K_{j,k}$ in equation 8.3 will diverge with increasing N. As we can draw an arbitrarily large number of masses D_i from the C05 IMF, we present $K_{j,k}^{\frac{1}{N}}$ as a figure of merit for the performance of $\mathbf{M_j}$ over $\mathbf{M_k}$. This value has to two appealing features: firstly, the value of $K_{j,k}^{\frac{1}{N}}$ will converge with increasing N and secondly, if N is sufficiently large, we can estimate the ratio of likelihoods of $\mathbf{M_j}$ and $\mathbf{M_k}$ when n masses are drawn from the C05 IMF. This is equal to $K_{j,k}^{\frac{n}{N}}$. We calculate values of $K_{j,k}^{\frac{n}{N}}$ for $\mathbf{M}_{\rm NRF}$, $\mathbf{M}_{\rm ERF}$ and $\mathbf{M}_{\rm CRF}$ by drawing $N = 10^5$ stellar masses from the C05 IMF and calculating their likelihoods. Results are shown in Table 8.2 for $n = 1$, 10

$n = 1$			
	$\mathbf{M}_{\mathrm{NRF}}$	$\mathbf{M}_{\mathrm{ERF}}$	$\mathbf{M}_{\mathrm{CRF}}$
$\mathbf{M}_{\mathrm{NRF}}$	1	1.21	0.77
$\mathbf{M}_{\mathrm{ERF}}$	0.82	1	0.64
$\mathbf{M}_{\mathrm{CRF}}$	1.29	1.57	1
$n = 10$			
	$\mathbf{M}_{\mathrm{NRF}}$	$\mathbf{M}_{\mathrm{ERF}}$	$\mathbf{M}_{\mathrm{CRF}}$
$\mathbf{M}_{\mathrm{NRF}}$	1	6.85	0.08
$\mathbf{M}_{\mathrm{ERF}}$	0.15	1	0.01
$\mathbf{M}_{\mathrm{CRF}}$	13.2	90.0	1
$n = 20$			
	$\mathbf{M}_{\mathrm{NRF}}$	$\mathbf{M}_{\mathrm{ERF}}$	$\mathbf{M}_{\mathrm{CRF}}$
$\mathbf{M}_{\mathrm{NRF}}$	1	46.9	5.8×10^{-3}
$\mathbf{M}_{\mathrm{ERF}}$	0.02	1	1.2×10^{-4}
$\mathbf{M}_{\mathrm{CRF}}$	1.7×10^{2}	8.1×10^{3}	1

Table 8.2: Likelihoods of stars from Chabrier (2005) IMF fitting the NRF, ERF and CRF simulation results. Each value gives $K^{\frac{n}{N}} = (P(\mathbf{D}|\mathbf{M}_{\mathrm{COLUMN}})/P(\boldsymbol{D}|\mathbf{M}_{\mathrm{ROW}}))^{\frac{n}{N}}$, where $N = 10^5$.

and 20 .

We find in that the C05 IMF is most likely to fit $\mathbf{M}_{\mathrm{ERF}}$. Conversely, the C05 IMF is least likely to fit $\mathbf{M}_{\mathrm{CRF}}$. Therefore, $\mathbf{M}_{\mathrm{ERF}}$ is stronger than $\mathbf{M}_{\mathrm{NRF}}$, which is stronger than $\mathbf{M}_{\mathrm{CRF}}$. However, we must highlight two important assumptions with the model comparison. i) We are using random variates from the C05 IMF, not actual observations. The brown dwarf region of the C05 IMF is not as well constrained as the stellar region and this could bias the result. ii) The kernel smoothed PDFs are *estimates* and may not capture every detail of the true PDF. This aside, this method should at least be sensitive to the basic features of the distribution, such as position of the peak and width.

8.1.3 Evolutionary stages

The simulations were evolved for 2×10^5 yrs. This chronologically places the YSOs formed in these simulations somewhere between the class 0 and class I evolutionary stages (see Section 1.1.4 for class definitions). However, by the end of the simulations most of the gas has accreted on to the YSOs and they more closely resemble objects between the class I and class II stages. This suggests that the simulated cores are

[1]It may seem more intuative to calculate likelihoods by drawing the likelihood of the simulation YSO masses from the C05 IMF, however this would be incorrect. Using this method, we would infer a twenty identical $0.2\,\mathrm{M}_{\odot}$ YSOs are a better fit to the C05 IMF than twenty YSOs randomly drawn from the C05 IMF.

collapsing and fragmenting faster than they would in nature.

These simulations assume a model where the combined mass of the YSO and gas envelope is constant. In nature, this is not the case as material from the parent molecular cloud can, and does, accrete on to the core while it collapses. Therefore as envelope mass transferred to the YSO, the envelope gains some mass from the molecular cloud. This may explain why such a high proportion of the gas in these simulations has accreted onto the YSOs. Magnetic fields may also affect the rates at which material accretes on to a YSO. A poloidal magnetic field (e.g. Mouschovias, 1976) in the envelope may reduce the accretion rate. However, magneto-rotational instabilities (e.g. Zhu et al., 2007) can enhance accretion rates. Examining the effects of these phenomena may be necessary in future work.

8.1.4 Fragmentation

Mechanisms

In most of the simulations, the core collapses to produce a central protostar around which a disc can form. If the disc can cool quickly enough, and has a Toomre criterion of $Q < 1$, it can fragment to form additional YSOs. These typically have masses smaller than the central protostar. An example of this is shown in Figure 8.3. We see that the time scale of disc fragmentation is of order 10^3 yrs.

In some of the simulations, filaments that feed material into the centre of the core can fragment before a central protostar forms. Like disc fragmentation, this also occurs on time scales of order 10^3 yrs. An example of this is shown in Figure 8.4. This core has a relatively high mass of $M = 3.3\,\mathrm{M}_\odot$ and a low ratio of turbulent to gravitational energy with $\alpha_{\mathrm{TURB}} = 0.07$. The core collapses into a filament because it is particularly elongated, with its longest axis over twice the length of the other two. The filament then fragments into ten YSOs. This is in agreement with work by Goodwin et al. (2004), where low levels of turbulence such as this are capable of fragmenting sperical cores. An analysis on whether or not the degree of core elongation enhances this level of fragmentation will be an interesting topic of future work.

Feedback effects

There are two main differences between YSO mass distributions from the NRF and ERF simulations. The first is that in the NRF simulations, the mass peaks at $0.1\mathrm{M}_\odot$. In the ERF simulations, the mass peaks at $0.2\mathrm{M}_\odot$. The second difference is the presence of a small, low mass peak at $M \sim 0.01\mathrm{M}_\odot$ in the NRF simulations.

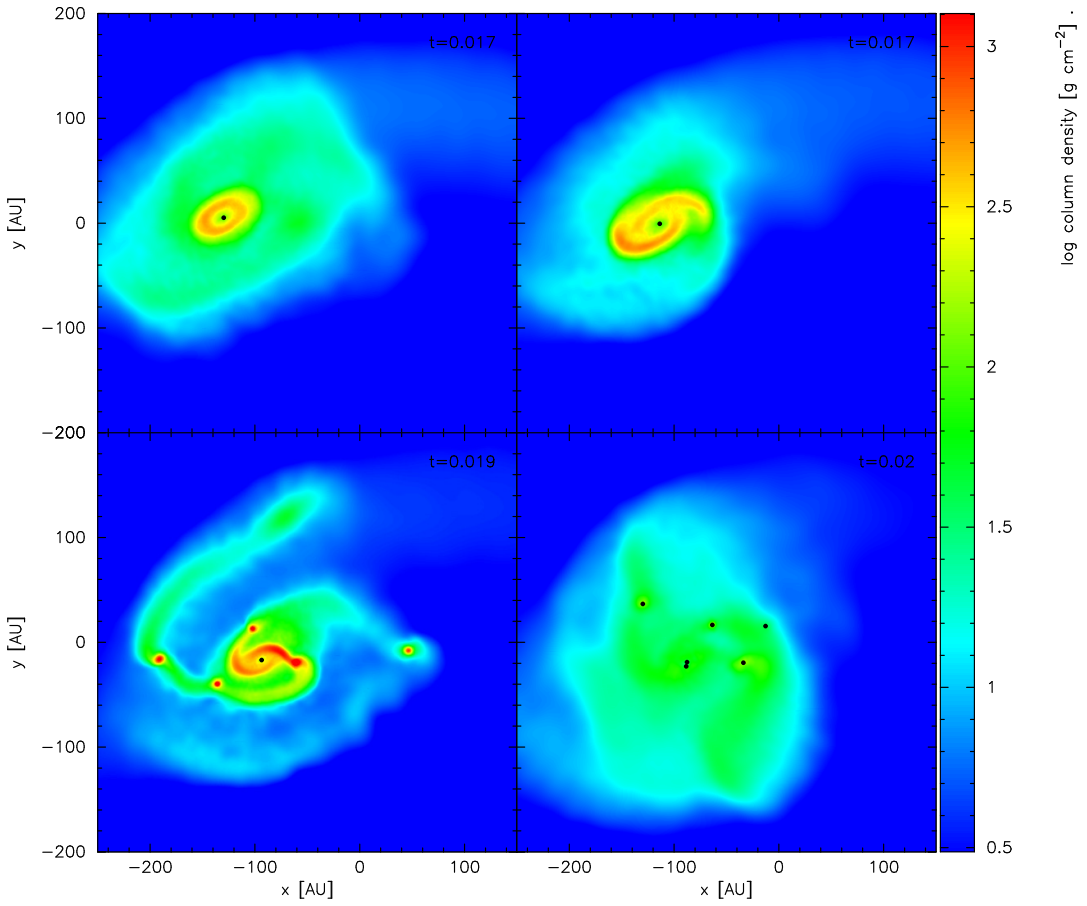

Figure 8.3: Column density plots taken from simulation `002_ERF_THR` showing disc fragmentation. Moving across, then down, snapshots taken at $t = 1.7 \times 10^{-2}$ Myr, $t = 1.8 \times 10^{-2}$ Myr, $t = 1.9 \times 10^{-2}$ Myr and $t = 2.0 \times 10^{-2}$ Myr. This prestellar core fragments into three stars and three brown dwarfs.

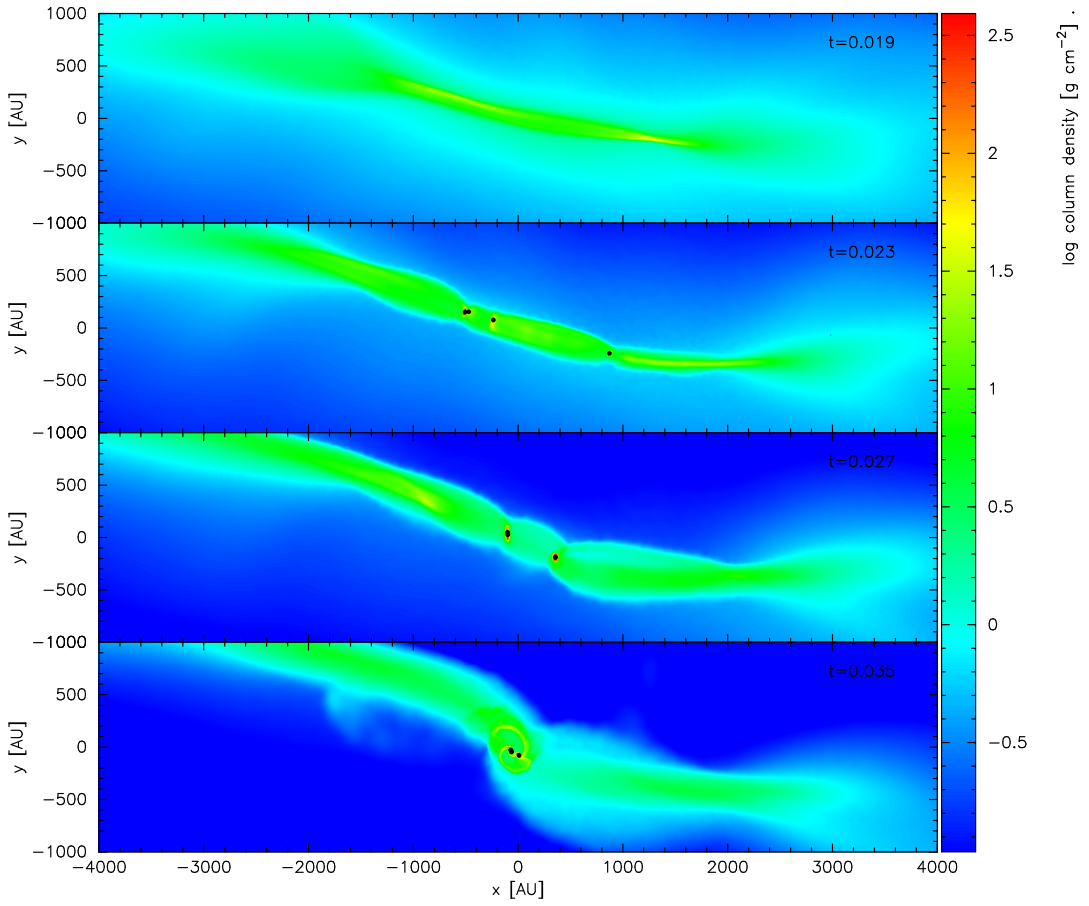

Figure 8.4: Column density plots taken from `098_ERF_THR` showing the fragmentation of a filament. From top to bottom, snapshots taken at $t = 1.9 \times 10^{-2}$ Myr, $t = 2.3 \times 10^{-2}$ Myr, $t = 2.7 \times 10^{-2}$ Myr and $t = 3.5 \times 10^{-2}$ Myr. This prestellar core fragments into eight stars and two brown dwarfs.

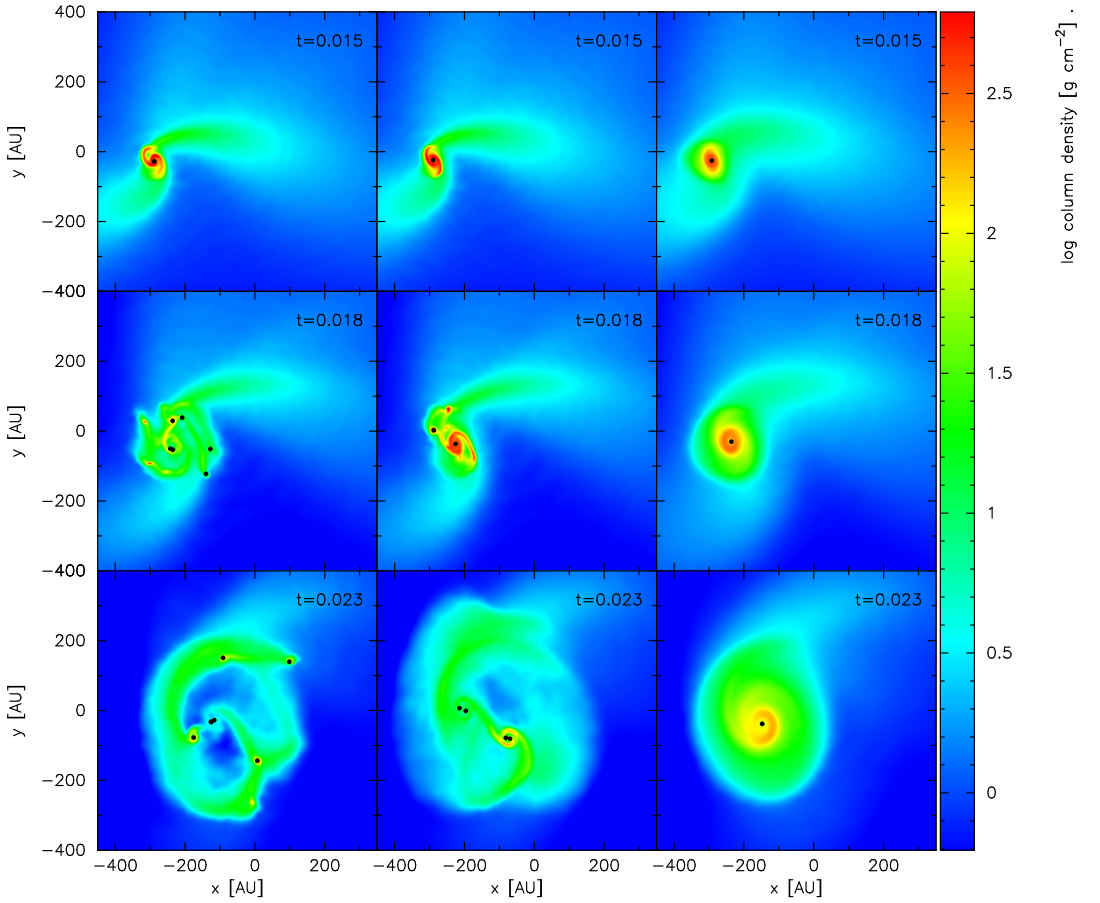

Figure 8.5: Column density plots from the `022_XXX_THR` simulations. The left-hand column gives snapshots from `022_NRF_THR`, the middle column gives snapshots from `022_ERF_THR` and the right-hand column gives snapshots from `022_CRF_THR`. The top row gives snapshots at $t = 1.5 \times 10^{-2}$ Myr, the middle row gives snapshots at $t = 1.8 \times 10^{-2}$ Myr and the bottom row gives snapshots at $t = 2.3 \times 10^{-2}$ Myr. `022_NRF_THR` fragments into four stars and nine brown dwarfs, `022_ERF_THR` fragments into four stars and `022_CRF_THR` collapses to form a single star.

The main peaks are populated by YSOs that form from core collapse. The secondary peak in the NRF simulations arises from the fragmentation of discs and filaments. These produce low mass objects which are preferentially ejected from the core (e.g. Bate et al., 2002). Once ejected, accretion ceases and their masses are frozen. They then contribute to the low mass peak the NRF mass distribution.

In the ERF simulations, high-luminosity outbursts periodically raise the temperature of the gas surrounding a sink from $\sim 10\,\mathrm{K}$ to $\sim 100\,\mathrm{K}$. These outbursts occur at intervals of $\Delta t_{\mathrm{OB}} \sim 10^4\,\mathrm{yrs}$, whereas gravitational instabilities form on times scales of $\Delta t_{\mathrm{GI}} \sim 10^3\,\mathrm{yrs}$. Therefore disc and filament fragmentation can still occur. However, as further protostars form, the global interval between outbursts decreases until eventually $\Delta t_{\mathrm{OB}} \sim \Delta t_{\mathrm{GI}}$. At this point, further star formation is inhibited by

regular luminosity outbursts. ERF therefore allows fragmentation to occur, but then regulates the process after a few YSOs have formed. This reduces the size of the secondary peak in the YSO mass distribution, as fewer BD mass YSOs are formed. Consequently, because fewer YSOs form, more gas can be deposited onto the central protostar (e.g. Girichidis et al., 2012b). This pushes the main YSO peak mass upwards.

In the CRF simulations, discs and filaments are continuously heated by accreting YSOs. Because of this, very little core fragmentation occurs and they mostly form single YSOs.

Figure 8.5 shows an example of a core evolving with NRF, ERF and CRF. We note that the usual trend is that the most YSOs are formed with NRF, followed by ERF then CRF. This is not always the case, however. If a core collapses very rapidly (i.e. on time scales less than 10^4 yrs), the fragmentation process can become chaotic and it is difficult to qualatatively predict the outcome.

Number of objects formed

In Figure 8.6, we see that the number of protostellar objects generated per core is correlated with the core mass. For the NRF and ERF simulations, cores with masses between $0.1\,\mathrm{M}_\odot$ and $0.3\,\mathrm{M}_\odot$ typically produce single YSOs whereas cores with masses between $3\,\mathrm{M}_\odot$ and $10\,\mathrm{M}_\odot$ produce tens of YSOs. As a broad generalisation, we will refer to cores with $M_{\mathrm{CORE}} \leq 1\,\mathrm{M}_\odot$ as low mass cores and cores with $M_{\mathrm{CORE}} > 1\,\mathrm{M}_\odot$ as high mass cores.

Figure 8.7 shows the distribution of YSO masses as a function of core mass. From the NRF and ERF simulations, we see that the arithmetic mean YSO mass is roughly constant over the entire range of core masses. With NRF we have $\bar{M}_\star^{\mathrm{NRF}} = 0.12\,\mathrm{M}_\odot$ and with ERF we have $\bar{M}_\star^{\mathrm{ERF}} = 0.19\,\mathrm{M}_\odot$. For comparison, the Jeans mass of the prestellar cores is roughly given by $M_{\mathrm{JEANS}} \approx 0.2\,^{+0.2}_{-0.1}\,\mathrm{M}_\odot$.

Also plotted in Figure 8.7 is the geometric mean of the YSO mass and its standard deviation. From this we see that high mass cores produce a wider range of YSOs than low mass cores. In low mass cores, there is little spread in the YSO mass because most of the available gas is deposited onto the central YSO. A disc will form, but it is often not massive enough to fragment. High mass cores have enough gas to form more massive YSOs and there is often enough gas remaining to build a massive disc. This can then fragment into low mass YSOs.

In the CRF simulations, we would expect each core to collapse into a single YSO with a final mass similar to the original core mass. This is true for low mass cores, however, high mass cores tend to also fragment into multiple objects, albeit to a

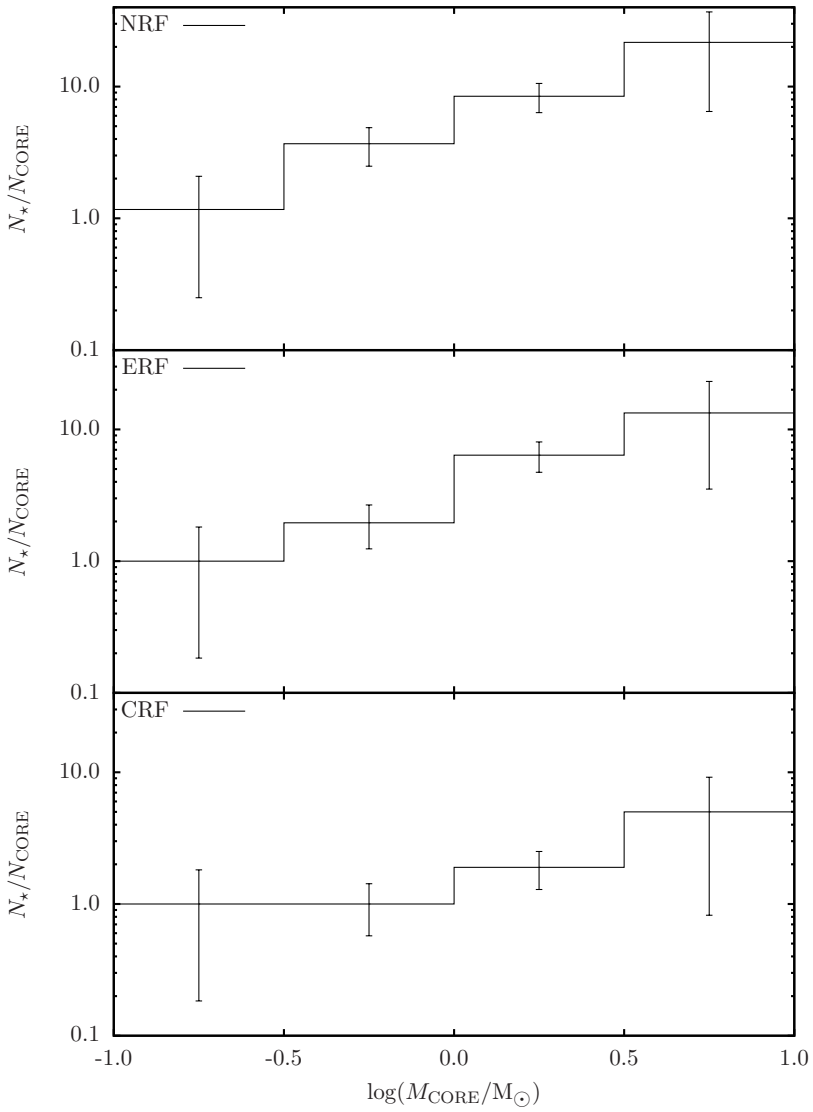

Figure 8.6: The number of YSOs produced per core as a function of core mass. Error bars reflect the Poisson uncertainty in both the number of core and number of sinks per bin. The top frame shows results for NRF simulations, the middle for ERF and the bottom for CRF.

lesser extent than in the other simulations.

From the simulations, we draw the following conclusions on the fragmentation of prestellar cores:

- YSO mass is *not* correlated to the mass of the core from which it forms. High mass cores produce on average the same mass YSOs as low mass cores. The difference is that high mass cores produce a *greater number* of YSOs than low mass cores.
- The average YSO mass appears to be of the same order as the Jeans mass of star forming environment.
- While the average YSO mass is not a function of core mass, the range of YSO masses is. High mass cores can produce higher mass YSOs than low mass cores due to the increased availability of gas. However, high mass cores also produce low mass YSOs through disc and filament fragmentation. This fragmentation does not often occur in low mass cores.

8.1.5 Multiplicity statistics

Most observational binary statistics are obtained from field stars (e.g. Janson et al., 2012; Raghavan et al., 2010; Reggiani and Meyer, 2011; Reipurth and Zinnecker, 1993; Tokovinin, 2008). These are Main Sequence stars which are found outside of clustered environments. Short and long period systems are well observed with radial velocity and astrometric measurements respectivly. In contrast, there are some observational difficulties in obtaining binary statistics from young stars, which the YSOs from these simulations mostly represent. Complete multiplicity statistics are difficult to measure as the emission lines from the gas envelope interfere with radial velocity measurements. Duchêne and Kraus (2013) provide a useful review of stellar multiplicity which covers most of the current observations.

Observations of pre-Main Sequence (PMS) visual-binaries in regions such as Taurus and Ophiuchus suggest that a higher proportion of stars are in multiple systems that those in the field (e.g. Kraus et al., 2011; Leinert et al., 1993; Ratzka et al., 2005). As PMS stars usually form in clusters, they undergo dynamical interactions that that bring their multiplicity statistics closer in line with those of field stars(e.g. Kouwenhoven et al., 2010; Parker and Goodwin, 2011, 2012; Parker et al., 2009; Parker and Reggiani, 2013). PMS binaries with semimajor axes $a \lesssim 10^2$ AU tend to survive cluster evolution whereas those with $a \gtrsim 10^4$ AU are always destroyed. Binaries with separations between these limits are partially destroyed, with preference to those of greater separation.

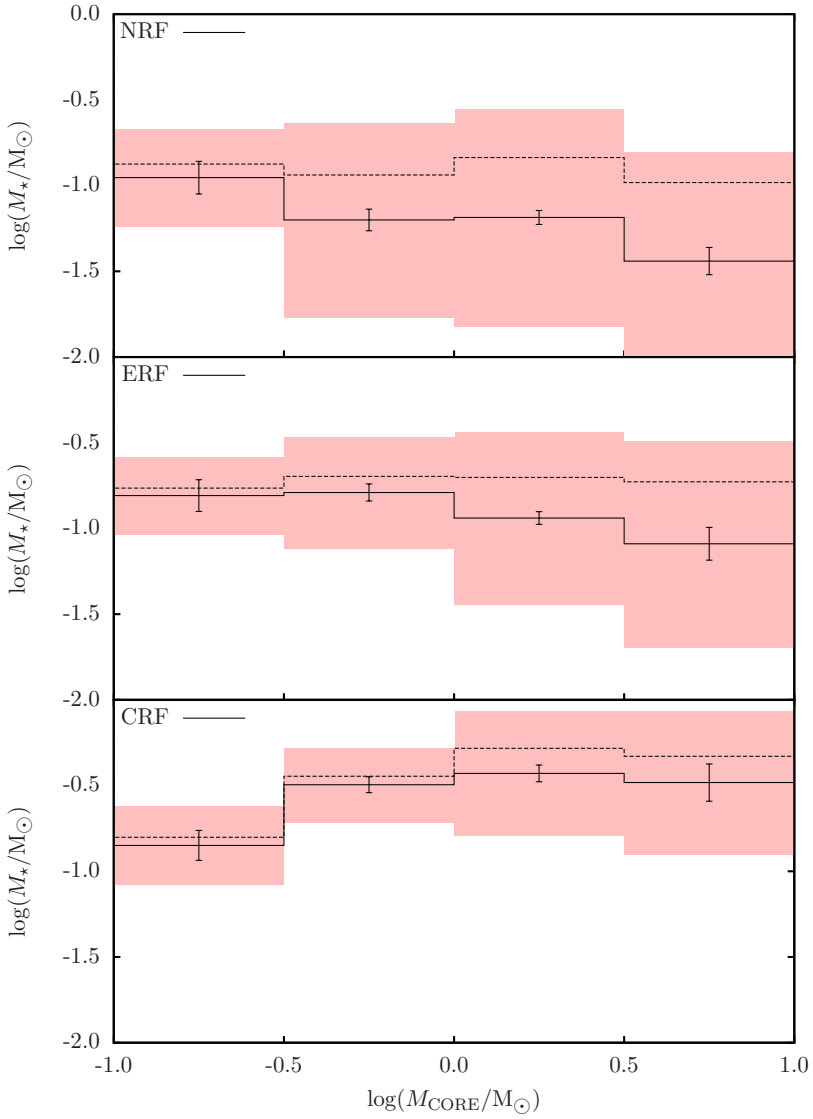

Figure 8.7: The distribution YSO masses as a function of core mass. The solid line gives the geometric mean mass and standard error. The shaded area shows the geometric standard deviation. The dashed line gives the arithmetic mean YSO mass. The top frame shows results for NRF simulations, the middle for ERF and the bottom for CRF.

We present the results from these simulations in comparison with multiplicity statistics from field stars and PMS stars. Observations of PMS stars provide information such estimated multiplicity fractions and distributions of separations. Observations of field stars provide useful information on how these measurements correlate with stellar mass.

Multiple systems

We isolate multiple YSO systems from the final state of each simulation by examining every possible YSO-YSO pair. These are deemed to be a binary pair if the following criteria are met: i) the gravitational perturbation on the pair of YSOs from all other YSOs is no greater than a factor of $\alpha_{\rm P} = 0.1$ times the acceleration between the pair. ii) Over at least one Keplerian period, the kinetic energy plus the gravitational potential energy of the YSO pair is negative. If these conditions are satisfied, the YSOs are considered to be a binary pair and their binary quantities (such as period, mass ratio etc.) are recorded. The two YSOs are then merged to form a single virtual YSO with mass equal to the sum of its two components, and position and velocity taken to be the mass-weighted average. The analysis is then repeated to allow for the detection of hierarchical multiple systems, i.e. we look for binary systems where one or more components are themselves binary systems. Due to the decreased stability of multiple systems with more than two components, we perform an additional check: iii) if one of the binary components is a sub-binary system, the tidal acceleration on the sub-binary from the other YSO must be no greater than $\alpha_{\rm P}$ times the mutual acceleration of the sub-binary, i.e.

$$\frac{2M_1 r}{R^3} < \alpha_{\rm P} \frac{M_2}{r^2}\,, \tag{8.4}$$

where a binary system masses M_1 and M_2 separated by distance R. In this case, the primary component is a star and the secondary component is binary system with total mass M_2 and separation r. As with criterion ii), criterion iii) must be true for at least one Keplerian period in order for it to be considered a stable multiple system. We do not impose a limit on how many levels of hierarchy each multiple system has, only that it is stable on all levels. We set $\alpha_{\rm P} = 0.1$ as we find that the change to the number of systems extracted is only minor with the stricter value of $\alpha_{\rm P} = 0.01$.

Figure 8.8 shows the number of systems produced with different orders of multiplicity. We find that in the NRF and ERF simulations, almost half the YSOs are in some kind of multiple system. Of these systems, roughly half again are binaries

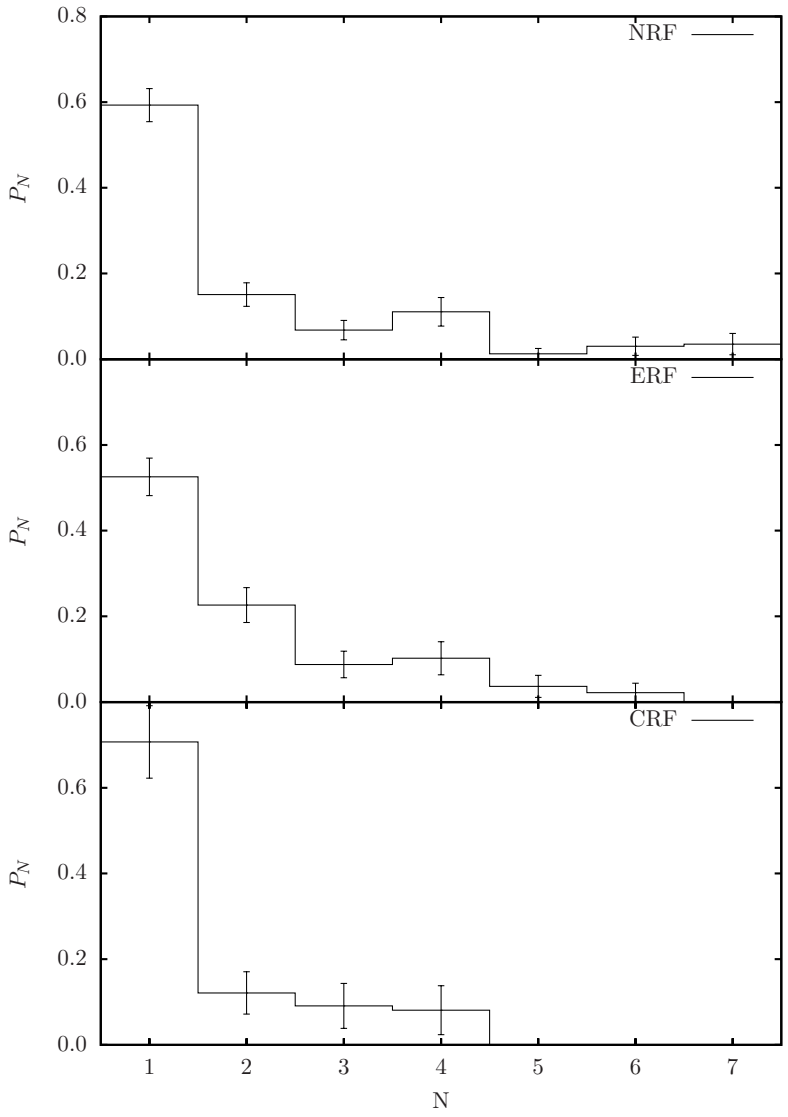

Figure 8.8: The distribution of YSOs in multiple systems of different order. The individual frames give distributions from simulations with NRF, ERF and CRF.

and the rest are higher order systems, i.e. triples, quadruples, etc.. Some cores even produce sextuple and septuple systems. Unlike N-body systems, the core gas provides a shallow gravitational potential. This makes it easier for stars to gradually adopt quasi-stable configurations instead of being violently ejected. Figure 8.9 shows a sextuple formed in simulation `052_ERF_THR`. This system was stable at the end of the simulation and had been so for $t = 1.5 \times 10^5$ yrs. Sextuple systems have been observed in the field (e.g. Tokovinin, 2008) and their formation in these simulations may explain their origin.

Comparison with observations

We will adopt the nomenclature defined by Reipurth and Zinnecker (1993). The fraction of *systems* which are multiple is measured by the multiplicity frequency:

$$F_{\rm M} = \frac{B + T + Q + \ldots}{S + B + T + Q + \ldots}, \tag{8.5}$$

where S is the number of single stars, B is the number of binaries, T is the number of triples, Q is the number of quadruples, etc.. The fraction of *stars* in multiple systems is measured by the companion probability:

$$P_{\rm C} = \frac{2B + 3T + 4Q + \ldots}{S + 2B + 3T + 4Q + \ldots}, \tag{8.6}$$

and the number of orbits per multiple system is given by the pairng factor

$$F_{\rm P} = \frac{B + 2T + 3Q + \ldots}{S + B + T + Q + \ldots}. \tag{8.7}$$

Goodwin et al. (2004) introduce the companion frequency where

$$F_{\rm C} = \frac{2B + 6T + 12Q + \ldots}{S + 2B + 3T + 4Q + \ldots}, \tag{8.8}$$

gives the mean number of companions per star. If $F_{\rm c} > P_{\rm C}$ or $F_{\rm p} > F_{\rm M}$, then some of multiple systems must be hierarchical.

From the simulations, it is generally easier to record the number of stars in different multiple systems, i.e. $N_{\rm X}$ is the number of stars in a system of order X. The multiplicity frequency can then be calculated

$$F_{\rm M} = \frac{\frac{N_{\rm B}}{2} + \frac{N_{\rm T}}{3} + \frac{N_{\rm Q}}{4} + \ldots}{N_{\rm S} + \frac{N_{\rm B}}{2} + \frac{N_{\rm T}}{3} + \frac{N_{\rm Q}}{4} + \ldots}. \tag{8.9}$$

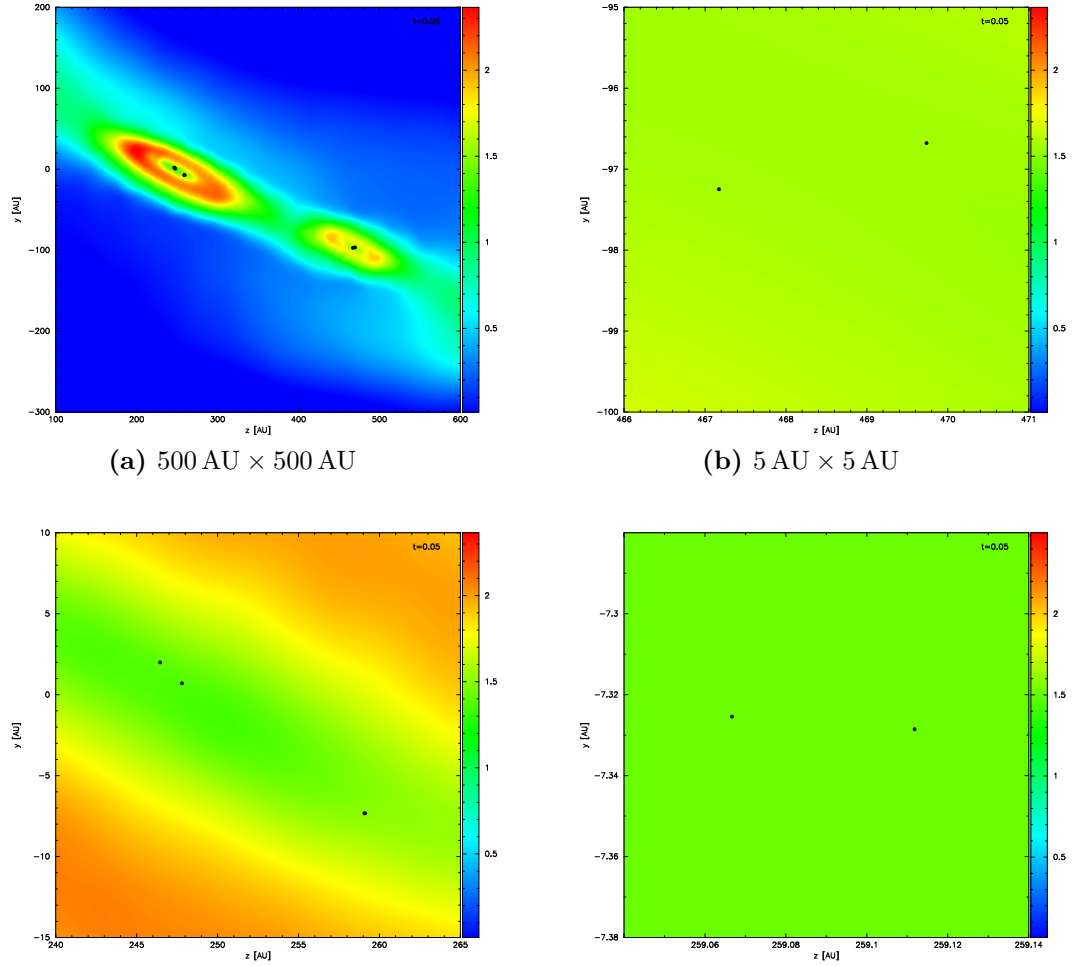

(a) 500 AU × 500 AU

(b) 5 AU × 5 AU

(c) 25 AU × 25 AU

(d) 0.1 AU × 0.1 AU

Figure 8.9: A sextuple system formed in the `052_ERF_THR` simulation. Figure (a) shows a binary system (right) orbiting a quadruple system (left). The total system has mass $0.64\,\mathrm{M}_\odot$. Figure (b) is an expanded view of the binary in Figure (a). The binary has mass $0.22\,\mathrm{M}_\odot$. Figure (c) is an expanded view of the quadruple system in Figure (a); here there are two binary systems orbiting one another. The binary of the left has mass $0.24\,\mathrm{M}_\odot$ and the binary on the right has mass $0.19\,\mathrm{M}_\odot$. Figure (d) is an expanded view of the binary system on the right-hand side of Figure (c). The colour scale gives the column density in units of $\log(\Sigma/\mathrm{g\,cm^{-2}})$ and the captions give the size of the plotting area.

Feedback	$N_\star$	$N_{\rm ORB}$	$N_{\rm SYS}$	$F_{\rm M}$	$P_{\rm C}$	$F_{\rm C}$
NRF	398	116	59	0.20 ± 0.01	0.42 ± 0.02	1.05 ± 0.06
ERF	274	79	48	0.25 ± 0.02	0.46 ± 0.03	0.94 ± 0.06
CRF	98	18	11	0.14 ± 0.02	0.29 ± 0.05	0.54 ± 0.09

Table 8.3: Binary statistics from the NRF, ERF and CRF simulations. Column 1 gives the feedback type. Column 2 gives the total number of YSOs. Column 3 gives the number of binary orbits. Column 4 gives the number of multiple systems. Column 5 gives the the multiplicity frequency. Column 6 gives the companion probability. Column 7 gives the companion frequency.

$M_\star$ ($\rm M_\odot$)	Field	NRF	ERF	CRF
$0.06 \leq M_\star < 0.1$	$F_{\rm M} = 0.22 \pm 0.05$	0.26 ± 0.03	0.22 ± 0.05	0.12 ± 0.07
	$F_{\rm P} = 0.22 \pm 0.05$	0.48 ± 0.06	0.31 ± 0.07	0.17 ± 0.10
$0.1 \leq M_\star < 0.5$	$F_{\rm M} = 0.26 \pm 0.03$	0.41 ± 0.02	0.36 ± 0.02	0.19 ± 0.03
	$F_{\rm P} = 0.33 \pm 0.05$	0.83 ± 0.04	0.64 ± 0.04	0.30 ± 0.05
$0.7 \leq M_\star < 1.3$	$F_{\rm M} = 0.44 \pm 0.02$	0.44 ± 0.13	0.54 ± 0.11	0.06 ± 0.04
	$F_{\rm P} = 0.62 \pm 0.03$	0.69 ± 0.19	0.85 ± 0.17	0.18 ± 0.11

Table 8.4: A comparison of the binary statistics from the NRF, ERF and CRF simulations with hose of field obsevations. Column 1 gives the mass range. Column 2 gives the multiplicity frequency and pairing factors from field observations. Columns 3, 4 and five give the same statistics from the NRF, ERF and CRF simulations respectively.

This makes it easy to bin results by mass, as individual stars, rather than entire systems, can make contributions to the calculation. Similarly, the companion probability is given by

$$P_{\rm C} = \frac{N_{\rm B} + N_{\rm T} + N_{\rm Q} + \ldots}{N_{\rm S} + N_{\rm B} + N_{\rm T} + N_{\rm Q} + \ldots}\,, \tag{8.10}$$

the pairing factor is given by

$$F_{\rm P} = \frac{\frac{N_{\rm B}}{2} + \frac{2N_{\rm T}}{3} + \frac{3N_{\rm Q}}{4} + \ldots}{N_{\rm S} + \frac{N_{\rm B}}{2} + \frac{N_{\rm T}}{3} + \frac{N_{\rm Q}}{4} + \ldots}\,, \tag{8.11}$$

and the companion frequency is given by

$$F_{\rm C} = \frac{N_{\rm B} + 2N_{\rm T} + 3N_{\rm Q} + \ldots}{N_{\rm S} + N_{\rm B} + N_{\rm T} + N_{\rm Q} + \ldots}\,. \tag{8.12}$$

Comparison with observations: Multiplicity

Observations of field stars suggests that stellar multiplicity increases with primary mass. This typically ranges from $F_{\rm M} = 0.26 \pm 0.03$ for stars with $0.1\,{\rm M}_\odot \lesssim M_\star \lesssim 0.5\,{\rm M}_\odot$ to $F_{\rm M} \geq 0.5$ for stars with $M_\star \gtrsim 5\,{\rm M}_\odot$ (reviewed in Duchêne and Kraus, 2013). By comparison, in low to medium density star forming regions like Ophiuchus and Taurus, stellar multiplicity frequencies are usually between one and two times greater than those of field stars (e.g. Kraus et al., 2011; Leinert et al., 1993; Ratzka et al., 2005).

Figure 8.10 shows how the YSO multiplicity statistics from the simulations vary with stellar mass. For the NRF and ERF simulations, we find results are consistent with the observation that multiplicity frequency increases with stellar mass. This is not the case with the CRF simulations. Here the multiplicty frequency drops from $F_{\rm M} = 0.15 \pm 0.2$ when $0.1\,{\rm M}_\odot \leq M_\star < 1.0\,{\rm M}_\odot$ to $F_{\rm M} = 0.03 \pm 0.02$ when $1.0\,{\rm M}_\odot \leq M_\star < 10\,{\rm M}_\odot$.

In table 8.4 we compare the simulation multiplicity frequencies and pairing factors with those of field stars, taken from Duchêne and Kraus (2013). We see that over all mass ranges, the multiplicity frequencies from the ERF and NRF simulations are equal to or higher than those of field stars. Of the three mass ranges, $0.1\,{\rm M}_\odot \leq M_\star < 0.5\,{\rm M}_\odot$ has the least uncertainty from counting statisitics. Here we find that the NRF and ERF multiplicity frequencies are respectively about 1.6 and 1.4 times greater than those of field stars. In the same mass range we find that the ERF and NRF pairing factors are respectively 2.5 and 1.9 times greater than those of field stars. This shows that the multiple systems formed in these simulations are both more abundent than those found in the field and also have a greater level of hierarchy. This agrees well with observations of young star forming regions. In contrast to this, the binary frequencies and pairing factors from the CRF simulations are lower than those of field stars.

The multiplicty statistics from the NRF and ERF simulations agree well with observations. In both cases, the multiplicity frequency increases with stellar mass and the degree of multiplicity exceeds that field stars. Neither of these two statements are true for the CRF simulations. Because of this, we believe that it is very unlikely that continuous feedback from accretion is a dominant mechanism in nature.

Comparison with observations: a and T

Figure 8.11 shows the distribution of orbital periods of binary systems from the NRF, ERF and CRF simulations. The red histograms show the distribution of all orbital periods, the green histrograms show the distribution of orbital periods from binaries

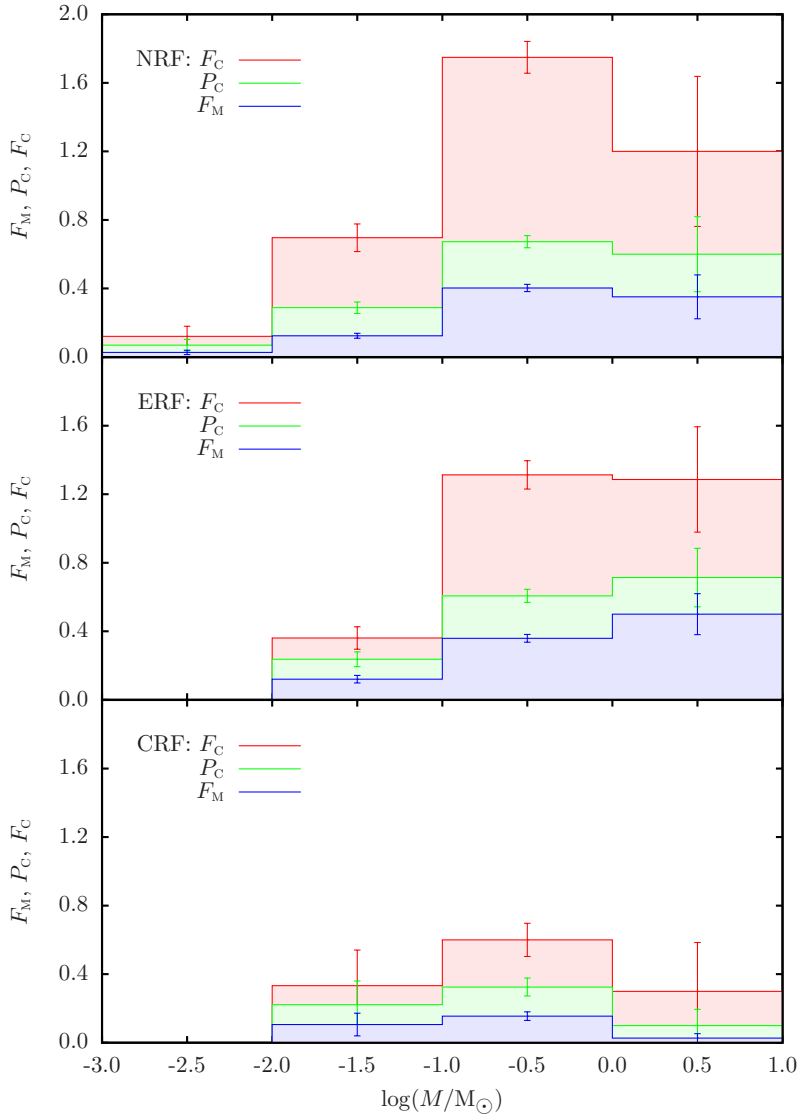

Figure 8.10: The fraction of YSOs in multiple systems as a function of YSO mass. The red lines show the companion frequency, the green lines show the companion probability and the blue lines show the multiplicity frequency. The individual frames give distributions from simulations with NRF, ERF and CRF.

with primary masses $> 0.2\,M_{\odot}$ and the blue histrograms show the distribution of orbital periods from binaries with primary masses $> 0.4\,M_{\odot}$. We see from the histrograms and cumulative distributions that the NRF and ERF distributions are very similar.

The NRF and ERF simulations produce a wide range of orbital periods with $10^{-2}\,\mathrm{yrs} < T < 10^{5}\,\mathrm{yrs}$. This corresponds to a range of semimajor axes $10^{-1}\,\mathrm{AU} \lesssim a \lesssim 10^{3}\,\mathrm{AU}$. We also see that distribution of periods is shifted upwards with increasing primary mass. This result is in general agreement with field observations (reviewed in Duchêne and Kraus, 2013). Observations of pre-Main sequence binary sytems show that the number of orbital separations decreases significantly for distances greater than $\sim 100\,\mathrm{AU}$ (e.g. King et al., 2012a,b). We see rough agreement with this in Figure 8.11 where there are few semimajor axes greater than $\sim 300\,\mathrm{AU}$.

Comparison with observations: e and q

Figure 8.12 shows the distributions of binary eccentricities. For both the NRF and ERF simulations, we see that the distribution of eccentricities decreases almost monotonically from zero to one. This result is difficult to interpret as binary orbits tend to circularise over time due to tidal forces. The physics required to capture this is not included in the simulations.

Figure 8.13 shows the distribution of binary mass ratios. In the NRF and ERF simulations, the distiribution of mass ratios is rougly flat between $0.2 < q < 1$ for systems with primary masses $> 0.2\,\mathrm{AU}$. Observations also suggest that distribution of mass ratios is roughly flat between $0.2 < q < 1$ for systems with primary masses $> 0.3\,\mathrm{AU}$(e.g. Reggiani and Meyer, 2011). This is promising as Parker and Reggiani (2013) show that the distribution of mass ratios is not strongly affected by dynamical interactions within clusters.

Summary of binary statistics

We find that the NRF and ERF simulations reproduce many observed multiplicity statistics. In notable agreement, with observations we see that:

- We produce high order multiple systems with $N \geq 3$. These are observed in the field, but are difficult to produce using N-body interactions alone.

- We produce a large range of semimajor axes with $10^{-1}\,\mathrm{AU} \lesssim a \lesssim 10^{3}\,\mathrm{AU}$. There are few semimajor axes greater than $\sim 300\,\mathrm{AU}$, agreeing reasonably well with observations of young stars.

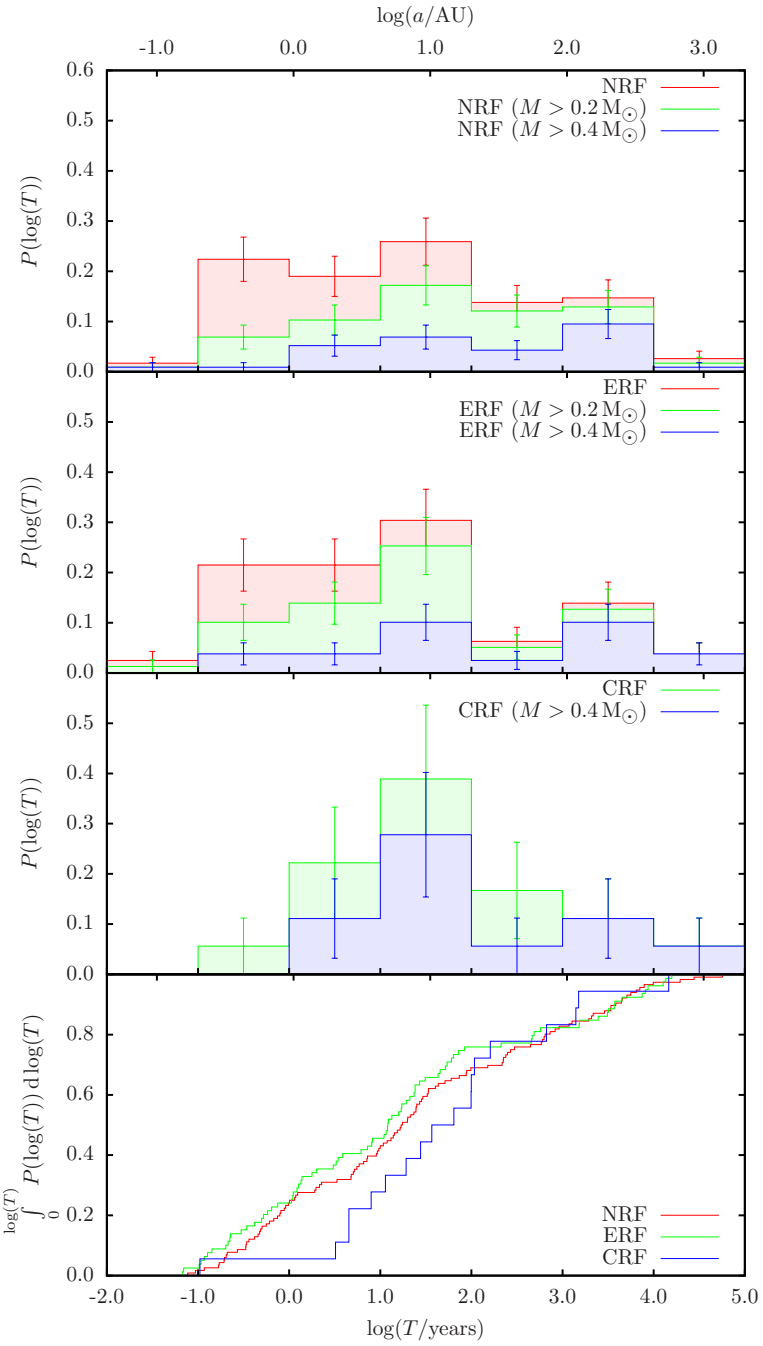

Figure 8.11: The distribution of orbital periods of binary systems. The top three frames give distributions from simulations with NRF, ERF and CRF. The histograms have bins equally spaced in $\log(T)$. The red histrograms show the distributions of from all the YSOs, the green from YSOs with masses greater than $0.2\,\mathrm{M}_\odot$ and the blue from YSOs with masses greater than $0.4\,\mathrm{M}_\odot$. The cumulative distributions of all three are compared in the bottom frame. Along the top of the Figure is the approximate semimajor axis a for given T. Here $a = [(T^2 G M_{\mathrm{SYS}})/(2\pi^2)]^{(1/3)}$ where $M_{\mathrm{SYS}} = 0.4\,\mathrm{M}_\odot$ is the typical system mass.

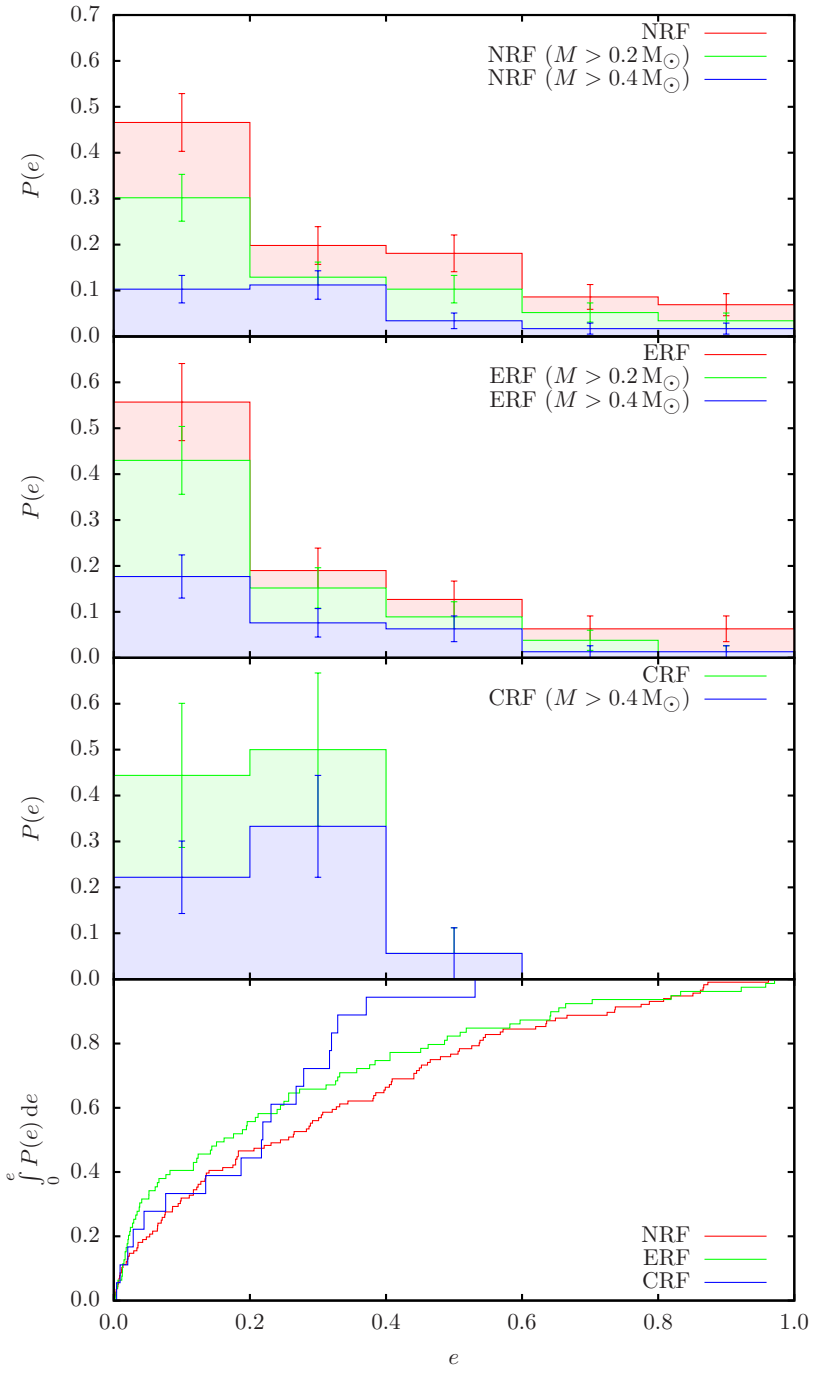

Figure 8.12: The distribution of orbital eccentricities of binary systems. The top three frames give distributions from simulations with NRF, ERF and CRF. The histograms have bins equally spaced in e. The red histrograms show the distributions of from all the YSOs, the green from YSOs with masses greater than $0.2\,M_\odot$ and the blue from YSOs with masses greater than $0.4\,M_\odot$. The cumulative distributions of all three are compared in the bottom frame.

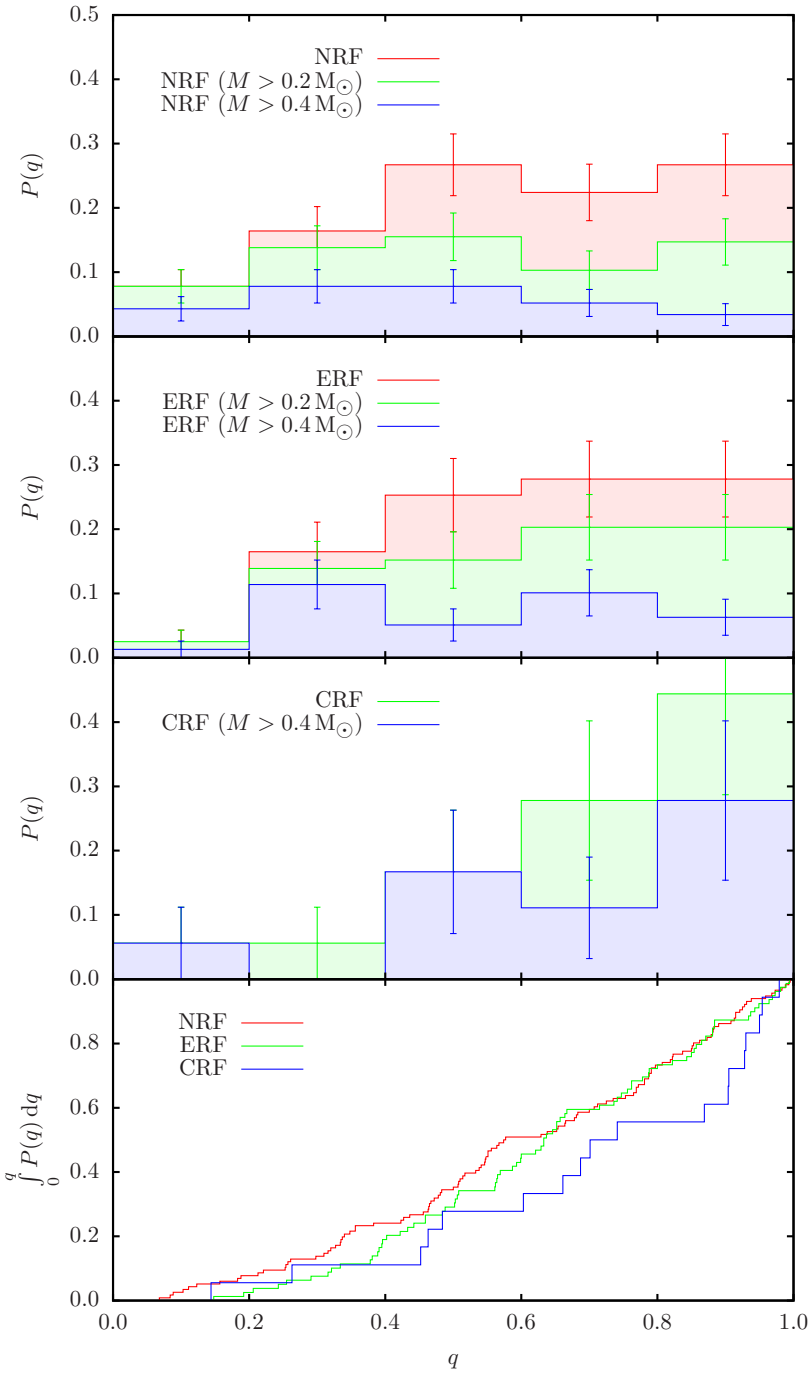

Figure 8.13: The distribution of orbital mass ratios of binary systems. The individual frames give distributions from simulations with NRF, ERF and CRF. The histograms have bins equally spaced in q. The red histrograms show the distributions of from all the YSOs, the green from YSOs with masses greater than $0.2\,M_\odot$ and the blue from YSOs with masses greater than $0.4\,M_\odot$. The cumulative distributions of all three are compared in the bottom frame.

- We reproduce the observed mass ratio distribution of binary systems. This is particularly promising as it been shown that the field distribution *should* be similar to the primordial distribution.

We must note that as these stars form in small N clusters in isolated cores, it is unclear how these binary statistics will evolve with time. We plan to follow up these simulations by using the small N clusters from each core as building blocks for an ensemble of larger N-body cluster simulations.

8.2 Simulations with compressive and solenoidal turbulence

In this section we present preliminary work on prestellar cores with purely compressive and purely solenoidal velocity fields. A prestellar core that is shocked by external sources (e.g. feedback from a neighbouring OB star) might have a velocity field which is dominated by compressive modes. As interstellar gas is a compressible fluid, it is difficult to imagine why a core would have a purely solenoidal field. However, we include the results to see if there is a noticeable change in YSO formation when there are no compressive velocity modes in the initial conditions.

As defined in Chapter 4, Section 4.2.3, a compressive field has $\Xi = 0$, a solenoidal field has $\Xi = \infty$ and field with 2:1 compressive to solenoidal modes has $\Xi = 2$. Tables 8.6 and 8.5 list the results from the simulations with $\Xi = 0$ and $\Xi = \infty$ respectively. These simulations have the same initial conditions as the $\Xi = 2$ simulations, modulo that the all the solenoidal modes are removed from the velocity fields when $\Xi = 0$ and all the compressive modes are removed when $\Xi = \infty$. They are evolved for 2×10^5 yrs.

8.2.1 Compressive turbulence: $\Xi = 0$

Thirty-one of the fifty simulations with $\Xi = 0$ are prestellar. With NRF, the prestellar cores produce on average 2.6 stars and 3.1 brown dwarfs per core with an SFE of 78%. With ERF, the cores produce 2.5 stars and 1.4 brown dwarfs per core with an SFE of 85%. With CRF, the cores produce 1.5 stars and 0.1 brown dwarfs per core with an SFE of 77%.

We see from Figure 8.15 that the prestellar cores with $\Xi = 0$ produce bimodal YSO mass distributions in both the NRF and ERF simulations. They produce roughly the same number of brown dwarfs per core as those with $\Xi = 2$, but fewer stars.

8.2.2 Solenoidal turbulence: $\Xi = \infty$

Twenty-eight of the fifty $\Xi = \infty$ simulations run are prestellar. With NRF, the prestellar cores produce on average 4.2 stars and 4.6 brown dwarfs per core with an SFE of 77%. With ERF, the cores produce 3.4 stars and 1.5 brown dwarfs per core with an SFE of 76%. With CRF, the cores produce 1.6 stars and 0.1 brown dwarfs per core with an SFE of 77%.

We see from Figure 8.15 that prestellar cores with solenoidal velocity fields produce unimodal YSO mass distributions in both the NRF and ERF simulations. They produce roughly the same number of brown dwarfs and stars per core as the simulations with $\Xi = 2$.

8.2.3 Comparison of velocity fields

The number statistics of the $\Xi = 0$ and $\Xi = \infty$ simulations are not as robust as those from the $\Xi = 2$ simulations. This makes it difficult to give quantitative statements on these results. However, we can note some qualitative trends between the simulations.

In Figure 8.14 we compare three simulations which have the same mass, shape and size, but different values of Ξ. We see that when $\Xi = 2$ and $\Xi = \infty$, filaments feed gas into the centre of the core. This is followed by the formation of a central protostar and an accretion disc. The disc then fragments into multiple objects. This produces a central YSO with relatively high mass and multiple low mass YSOs. In contrast, when $\Xi = 0$, the core has little angular momentum and the filaments fragment before they can deposit material onto the protostar. This results in several YSOs with an initially more even distribution of masses. This seems to be fairly typical of the ensemble of simulations. We see more filamentary structure and fewer discs when $\Xi = 0$ than we do when $\Xi = 2$ and $\Xi = \infty$.

We see in Figure 8.17 that when $\Xi = 0$, the YSO mass distribution has a broader high mass peak than when $\Xi = 2$ and $\Xi = \infty$. We speculate that this may be because compressive shocks help different regions of the core fragment independently. The masses of YSOs formed from these local shocks are likely to be correlated to the shock strengths, which are randomly distributed. At present, more analysis is required to verify or reject this hypothesis.

The secondary low mass peaks in the YSO mass distributions when $\Xi = 0$ are also more pronounced than those when $\Xi = 2$ and $\Xi = \infty$. As all three velocity fields produce roughly the same number of brown dwarfs per core, we believe that this is just because of the reduced height of the main peak. Again, more work is

Table 8.5: The number of YSOs formed from each core simulation with $\Xi = \infty$. Column 1 gives the core number, column 2 gives the core mass, column 3 gives the core's ratio of thermal to gravitational energy and column 4 gives the core's ratio of turbulent to gravitational energy. Columns 5, 6 and 7 give the total sink mass, the number of stellar-mass YSOs and the number of brown dwarf-mass YSOs formed with no radiative feedback from YSOs. Columns 8, 9 and 10 give the same quantities when there is episodic radiative feedback and columns 11, 12 and 13 give the quantities when there is continuous radiative feedback.

				NRF			ERF			CRF		
Core N	$M_{\rm CORE}$	$\alpha_{\rm THERM}$	$\alpha_{\rm TURB}$	$\sum M_{\rm YSO}$	$N_\star$	$N_{\rm BD}$	$\sum M_{\rm YSO}$	$N_\star$	$N_{\rm BD}$	$\sum M_{\rm YSO}$	$N_\star$	$N_{\rm BD}$
1	0.478	0.452	0.051	0.327	3	1	0.282	2	0	0.245	1	0
2	0.809	0.229	0.136	0.705	4	7	0.725	3	0	0.581	1	0
3	1.881	0.303	0.163	1.437	6	2	1.544	4	1	1.008	1	0
8	2.999	0.401	0.145	0.445	0	9	0.465	1	6	0.162	1	1
9	0.540	0.508	0.304	0.140	1	0	0.142	1	0	0.112	1	0
10	2.358	0.131	0.138	2.167	7	2	2.203	4	2	2.214	4	0
11	1.307	0.231	0.127	1.150	6	3	1.046	6	0	1.093	6	1
14	1.532	0.223	0.667	0.899	5	2	0.860	2	0	0.547	1	0
16	1.606	0.345	0.157	1.005	6	3	0.956	6	1	0.353	1	0
19	0.230	0.306	0.068	0.205	1	0	0.202	1	0	0.197	1	0
20	0.889	0.283	0.080	0.748	4	6	0.786	5	1	0.616	1	0
21	3.020	0.083	0.154	2.618	9	11	2.851	7	3	1.825	1	0
22	0.951	0.211	0.107	0.805	5	4	0.793	5	0	0.527	1	0
23	1.427	0.132	0.016	1.413	3	2	1.318	1	0	0.747	1	0

The number of YSOs formed from each core simulation with solenoidal turbulence.

				NRF			ERF			CRF		
Core N	$M_{\rm CORE}$	$\alpha_{\rm THERM}$	$\alpha_{\rm TURB}$	$\sum M_{\rm YSO}$	$N_\star$	$N_{\rm BD}$	$\sum M_{\rm YSO}$	$N_\star$	$N_{\rm BD}$	$\sum M_{\rm YSO}$	$N_\star$	$N_{\rm BD}$
26	2.016	0.232	0.186	1.356	7	4	1.264	6	4	0.608	1	0
27	3.439	0.119	0.102	2.840	9	15	2.811	6	1	2.157	3	0
29	1.763	0.114	0.145	1.668	5	13	1.636	3	1	1.590	3	0
31	0.767	0.450	0.092	0.474	2	5	0.480	2	3	0.353	1	0
34	0.278	0.259	0.025	0.253	1	0	0.252	1	0	0.247	1	0
35	1.772	0.172	0.094	1.711	7	5	1.654	5	5	0.958	1	0
36	1.698	0.208	0.201	1.388	5	6	1.285	6	1	1.287	6	1
38	1.506	0.133	0.049	1.482	3	7	1.333	1	0	1.334	1	0
40	1.240	0.241	0.181	1.073	5	5	1.072	4	1	0.679	2	0
43	1.059	0.314	0.021	0.947	3	8	0.925	3	5	0.716	1	0
44	0.287	0.479	0.119	0.195	2	0	0.161	1	0	0.128	1	0
45	0.773	0.536	0.079	0.495	2	4	0.395	3	0	0.299	1	0
48	0.138	0.470	0.047	0.102	1	0	0.105	1	0	0.094	1	0
50	1.365	0.168	0.069	1.284	6	6	1.276	4	8	0.879	1	0
Total	38.131			29.334	118	130	28.820	94	43	21.556	46	3

Table 8.6: The number of YSOs formed from each core simulation with $\Xi = 0$. Column 1 gives the core number, column 2 gives the core mass, column 3 gives the core's ratio of thermal to gravitational energy and column 4 gives the core's ratio of turbulent to gravitational energy. Columns 5, 6 and 7 give the total sink mass, the number of stellar-mass YSOs and the number of brown dwarf-mass YSOs formed with no radiative feedback from YSOs. Columns 8, 9 and 10 give the same quantities when there is episodic radiative feedback and columns 11, 12 and 13 give the quantities when there is continuous radiative feedback.

				NRF			ERF			CRF		
Core N	$M_{\rm CORE}$	$\alpha_{\rm THERM}$	$\alpha_{\rm TURB}$	$\sum M_{\rm YSO}$	$N_\star$	$N_{\rm BD}$	$\sum M_{\rm YSO}$	$N_\star$	$N_{\rm BD}$	$\sum M_{\rm YSO}$	$N_\star$	$N_{\rm BD}$
1	0.478	0.452	0.051	0.346	1	0	0.344	1	0	0.311	1	0
2	0.809	0.229	0.136	0.738	4	4	0.693	3	8	0.591	1	0
3	1.881	0.303	0.163	1.656	4	3	1.789	4	0	1.539	2	0
8	2.999	0.401	0.145	1.392	6	1	1.389	5	0	0.825	2	0
10	2.358	0.131	0.138	2.189	1	0	2.208	1	0	2.240	1	0
11	1.307	0.231	0.127	1.091	1	0	1.111	1	0	1.089	1	0
14	1.532	0.223	0.667	1.383	7	3	1.338	6	2	1.423	3	0
16	1.606	0.345	0.157	1.279	5	0	1.285	4	3	0.823	1	0
18	0.368	0.593	0.186	0.254	2	0	0.235	2	0	0.214	1	0
19	0.230	0.306	0.068	0.204	1	0	0.201	1	0	0.194	1	0
20	0.889	0.283	0.080	0.674	1	0	0.679	1	0	0.669	1	0
21	3.020	0.083	0.154	2.610	5	5	2.998	5	0	2.977	3	0
22	0.951	0.211	0.107	0.892	3	4	0.904	3	1	0.801	1	0
23	1.427	0.132	0.016	1.380	1	0	1.384	1	0	1.349	1	0

Table 8.6: The number of YSOs formed from each core simulation with compressive turbulence.

				NRF			ERF			CRF		
Core N	$M_{\rm CORE}$	$\alpha_{\rm THERM}$	$\alpha_{\rm TURB}$	$\sum M_{\rm YSO}$	$N_\star$	$N_{\rm BD}$	$\sum M_{\rm YSO}$	$N_\star$	$N_{\rm BD}$	$\sum M_{\rm YSO}$	$N_\star$	$N_{\rm BD}$
25	0.104	0.472	0.238	0.063	0	1	0.062	0	1	0.034	0	1
26	2.016	0.232	0.186	1.606	5	10	1.831	4	2	1.592	1	0
27	3.439	0.119	0.102	1.230	5	25	3.265	7	8	3.316	6	3
29	1.763	0.114	0.145	1.416	5	24	1.510	8	13	2.597	3	0
31	0.767	0.450	0.092	0.448	1	0	0.452	1	0	0.424	1	0
34	0.278	0.259	0.025	0.261	1	0	0.260	1	0	0.252	1	0
35	1.772	0.172	0.094	1.710	4	6	1.595	1	0	1.537	1	0
36	1.698	0.208	0.201	1.557	5	3	1.610	4	1	1.180	1	0
38	1.506	0.133	0.049	1.386	1	0	1.401	1	0	1.385	1	0
40	1.240	0.241	0.181	1.048	3	1	1.054	4	2	0.800	2	0
41	0.518	0.454	0.386	0.222	2	1	0.215	1	2	0.303	1	0
43	1.059	0.314	0.021	0.917	1	0	0.915	1	0	0.886	1	0
44	0.287	0.479	0.119	0.246	1	0	0.245	1	0	0.234	1	0
45	0.773	0.536	0.079	0.533	1	0	0.533	1	0	0.526	1	0
47	0.364	0.576	0.208	0.201	1	0	0.199	1	0	0.206	1	0
48	0.138	0.470	0.047	0.108	1	0	0.107	1	0	0.094	1	0
50	1.365	0.168	0.069	1.350	3	5	1.272	2	0	1.274	2	0

Table 8.6: The number of YSOs formed from each core simulation with compressive turbulence.

				NRF			ERF			CRF		
Core N	$M_{\rm CORE}$	$\alpha_{\rm THERM}$	$\alpha_{\rm TURB}$	$\sum M_{\rm YSO}$	$N_\star$	$N_{\rm BD}$	$\sum M_{\rm YSO}$	$N_\star$	$N_{\rm BD}$	$\sum M_{\rm YSO}$	$N_\star$	$N_{\rm BD}$
Total	38.944			30.390	82	96	33.085	77	43	31.684	45	4

required to verify this.

Finally, from Figure 8.17, we see that the distribution of YSOs when $\Xi = \infty$ does not appear to be significantly different to that when $\Xi = 2$. There is a hint that the secondary low mass peak may be absent when $\Xi = \infty$, but this may just be a consequence of the low number statistics.

8.3 Summary and conclusions

We have performed an extensive ensemble of simulations of prestellar cores in Ophiuchus. These simulations take into account the observed masses, shapes, sizes and velocity dispersions of cores. The resolution of these simulations is high enough to resolve the opacity limit, $M_{\rm o} \sim 3 \times 10^{-3}\,{\rm M}_{\odot}$, and permit the formation of binaries with separations as close as $a \sim 10^{-1}\,{\rm AU}$.

We summarise the key results from this chapter. We highlight the main findings from the simulations and, where possible, comment on the implications for star formation and evolution.

Protostellar masses

- Simulations with NRF and ERF reproduce observed ratios of low mass stars to brown dwarfs. Simulations with CRF do not. The YSO mass distribution from the ERF simulations provides the best likeness to the CO5 IMF. CRF makes it difficult for brown dwarf-mass YSOs to form and it is unlikely that accretion would not heat the surrounding gas at all. We therefore propose that ERF is an important, if not well understood, mechanism in star formation and have presented numerical work to support this assertion.

- We find that the mapping of the CMF onto the IMF is not statistically self-similar. The cores in this thesis *do not* fragment into a fixed number of YSOs, each with mass proportional to the parent core. Instead, the average mass of YSOs is fixed as a function of parent core mass, where higher mass cores produce proportionally more YSOs. The range of YSO mass increases as a function of core mass. This is because i) there is more gas available to produce higher mass YSOs and ii) because higher mass cores are more likely to form unstable accretion discs which fragment into low mass YSOs.

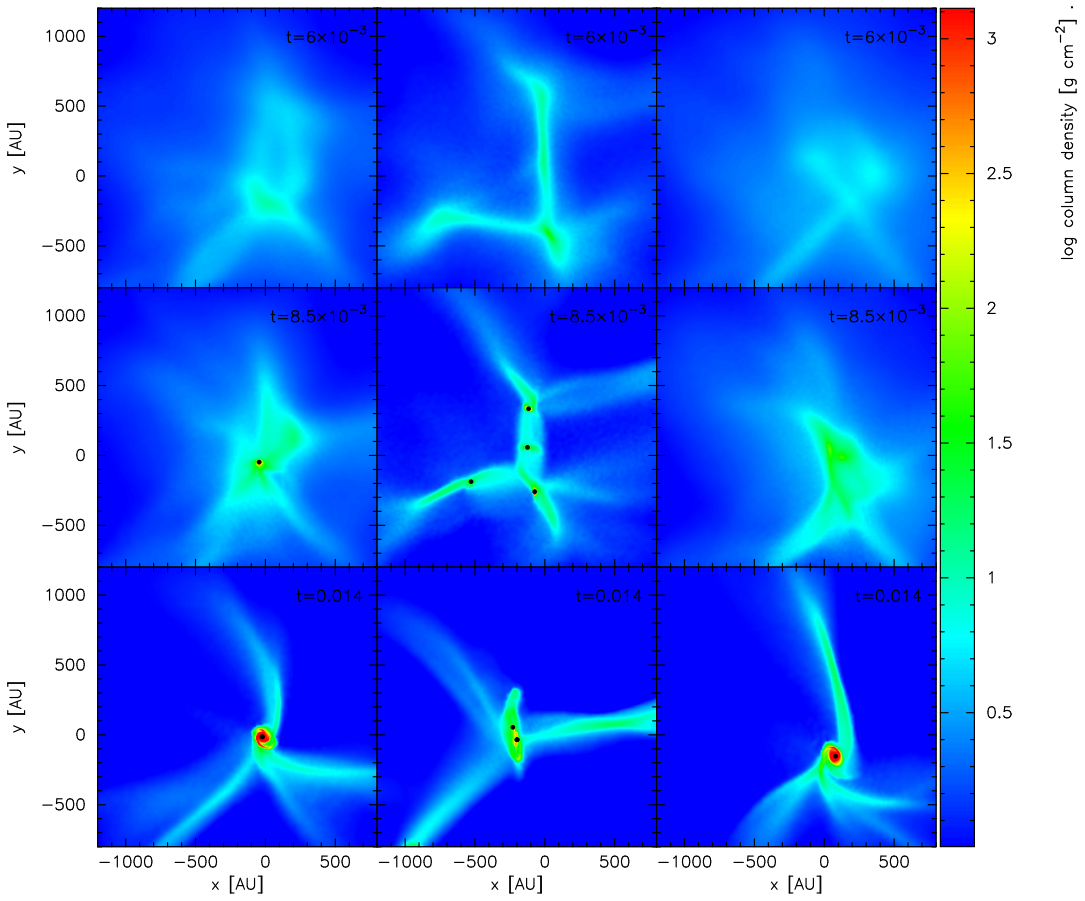

Figure 8.14: Column density plots take from the `021_ERF_XXX` simulations. The left-hand column gives snapshots from `021_ERF_THR`, the middle column gives snapshots from `021_ERF_COM` and the right-hand column gives snapshots from `021_ERF_SOL`. The top row gives snapshots at $t = 6.0 \times 10^{-3}$ Myr, the middle row gives snapshots at $t = 8.5 \times 10^{-3}$ Myr and the bottom row gives snapshots at $t = 1.4 \times 10^{-2}$ Myr. `021_ERF_THR` fragments nine stars and ten brown dwarfs, `021_ERF_COM` fragments into five stars and `021_ERF_SOL` fragments into seven stars and three brown dwarfs.

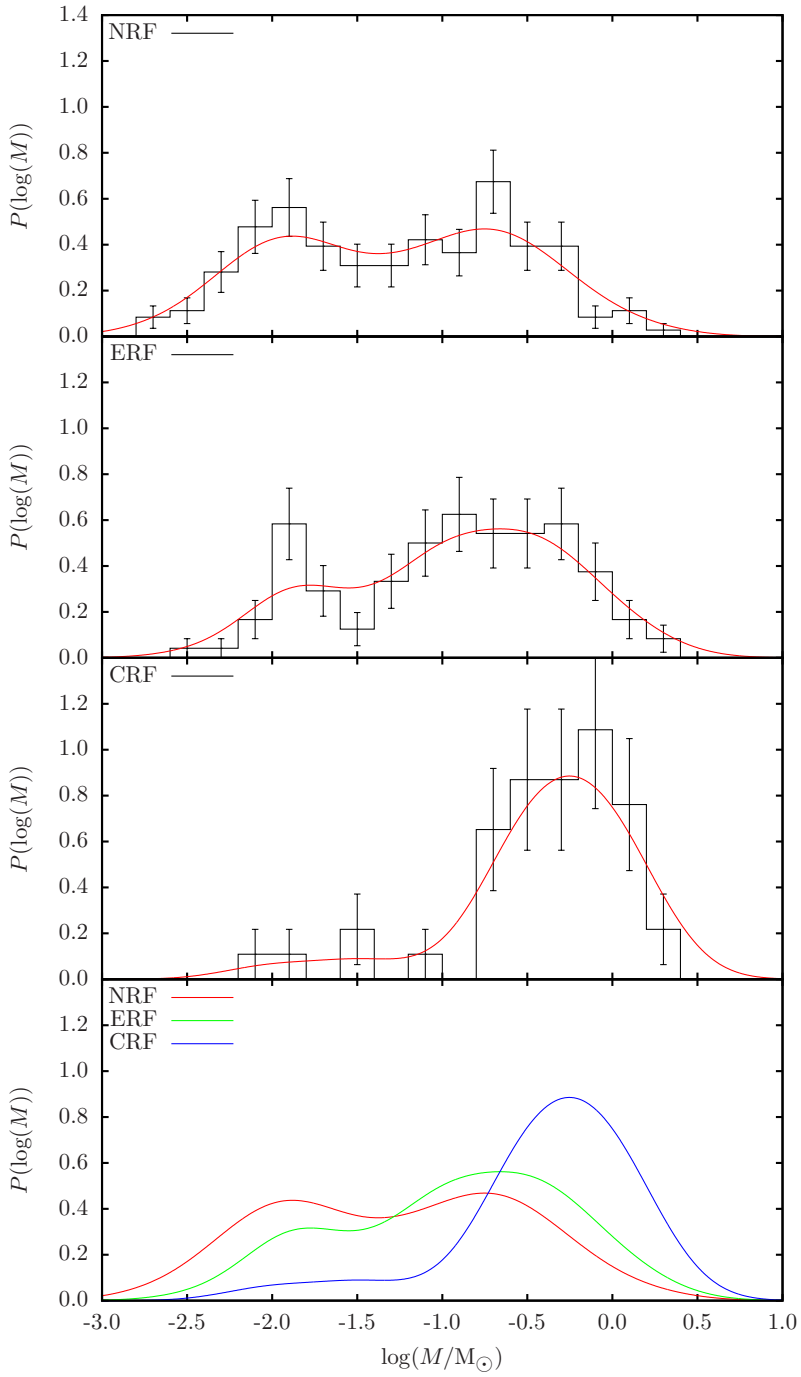

Figure 8.15: The YSO mass functions for simulations with compressive turbulence. The top three frames give the mass functions from simulations with NRF, ERF and CRF. The black histograms have bins equally spaced in $\log(M)$ and the red lines are kernel smoothed density functions. The bottom fame shows the NRF, CRF and ERF density profiles on a single plot.

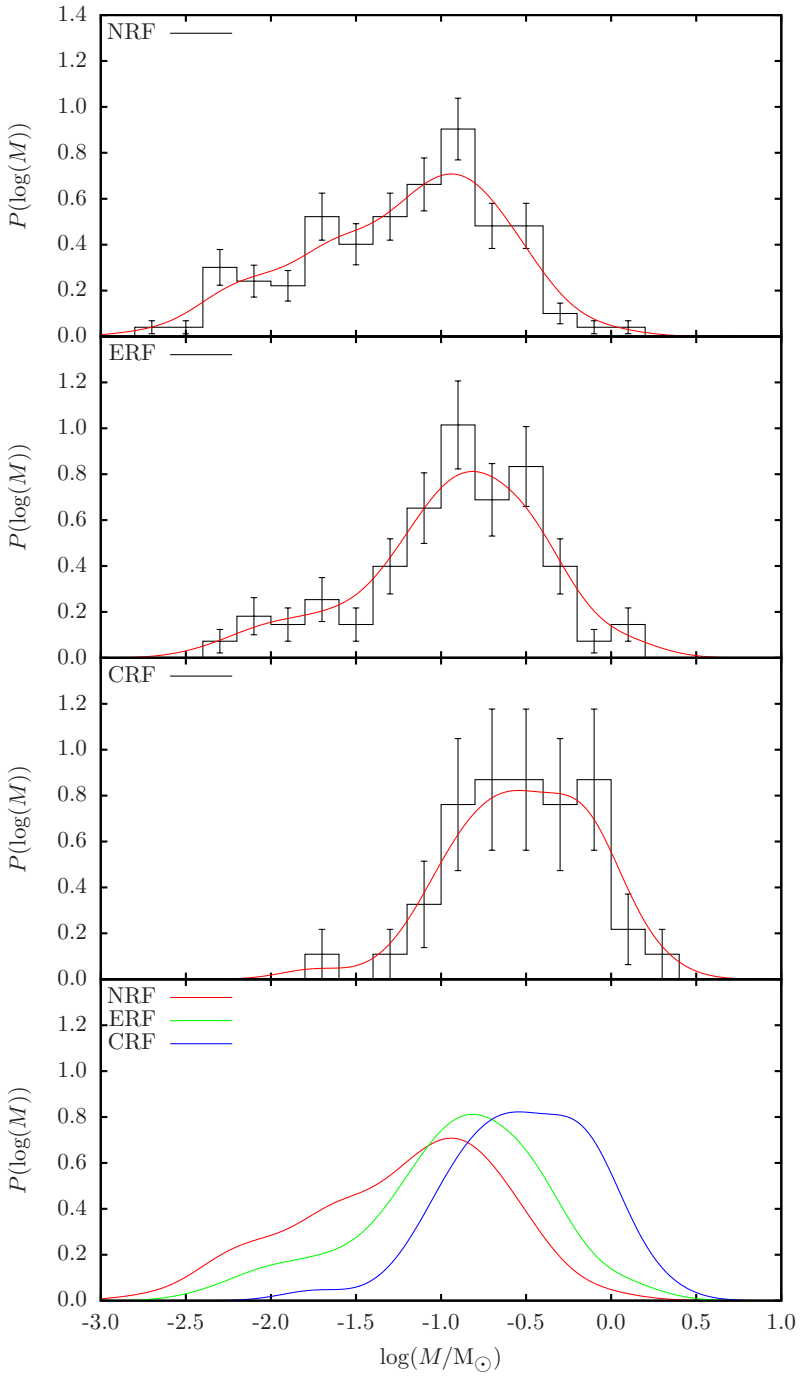

Figure 8.16: The YSO mass functions for simulations with solenoidal turbulence. The top three frames give the mass functions from simulations with NRF, ERF and CRF. The black histograms have bins equally spaced in $\log(M)$ and the red lines are kernel smoothed density functions. The bottom fame shows the NRF, CRF and ERF density profiles on a single plot.

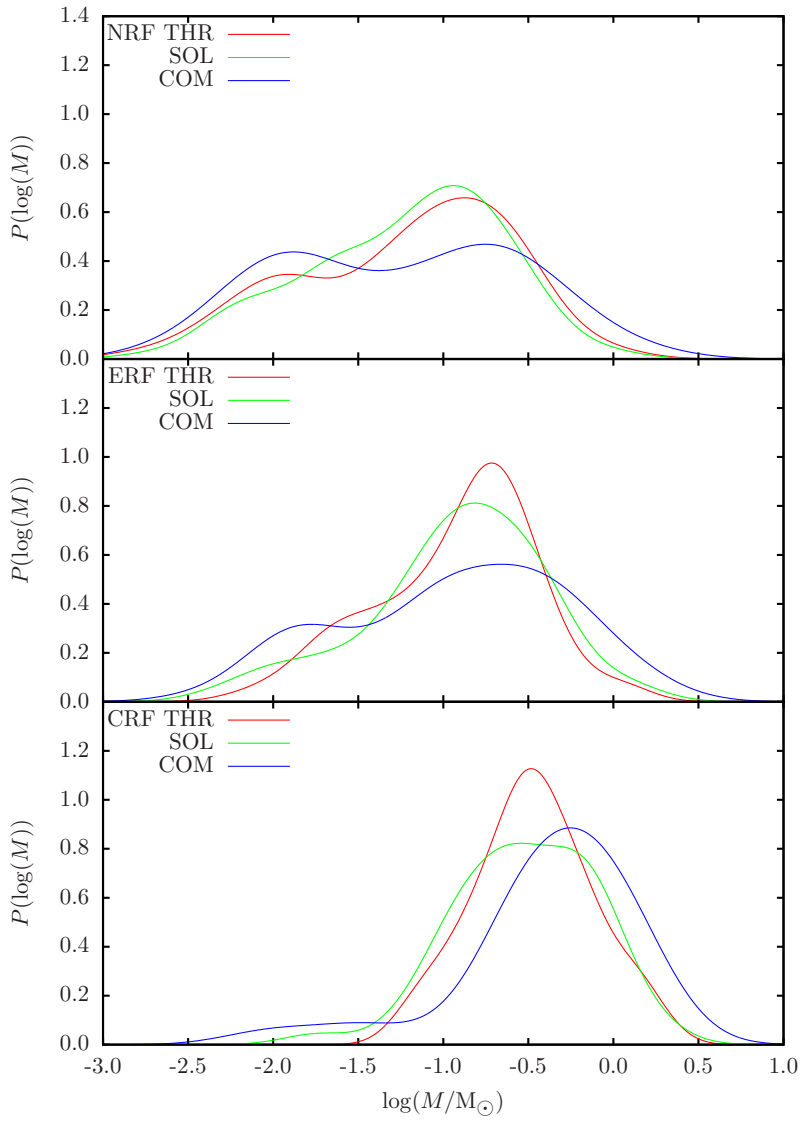

Figure 8.17: A comparison of all YSO mass functions. The top frame shows the YSO mass function for NRF simulations, the middle frame for ERF and the bottom frame for CRF. Mass functions from $\Xi = 2$ simulations are given by the red lines, mass functions from $\Xi = \infty$ simulations are given by the green lines and mass functions from the $\Xi = 0$ simulations are given by the blue lines.

Multiple systems

- Roughly half the YSOs formed in these simulations are in a multiple system. Of these multiples, roughly half are hierarchical with $N \geq 3$. We present an example of a sextuple system which remains stable for *at least* 1.5×10^5 yrs. These systems require the shallow gravitational potential from core gas to form and are difficult to manufacture from N-body interactions. While it is unclear if these systems would survive in clustered environment, they are observed in the field. We therefore propose that high order multiples regularly form during star formation and a reduced, but significant, fraction of these survive dynamical interactions in clusters.

- The binary statistics from these simulations compare well with observations. We produce a wide range of semimajor axes with $10^{-1}\,\mathrm{AU} \lesssim a \lesssim 10^3\,\mathrm{AU}$. We do not produce any very wide binaries (i.e. $a \gtrsim 10^4\,\mathrm{AU}$), however it is possible that these systems are formed through ejection from clusters. We also roughly reproduce the observed distribution of binary mass ratios. This is promising as it has been suggested that it is not strongly affected by dynamical interactions in clusters.

Velocity field

- We have presented some preliminary results on the effects of purely solenoidal and purely compressive velocity fields. Purely compressive fields appear to produce more filamentary structure as they evolve, compared with the other velocity fields. We find that compressive fields also widen the main peak of the YSO mass distribution. Purely solenoidal fields do not seem to produce particularly different results to fields with a 2:1 mix of solenoidal to compressive modes. Further investigation is required to fully characterise the behaviour of these cores and draw firm conclusions.

Chapter 9

Summary of this thesis

9.1 Ophiuchus

In Chapter 2 we compared dust emission observations of cores in Ophiuchus by Motte et al. (1998), Stanke et al. (2006) and Simpson et al. (2008) and line width observations by André et al. (2007). The dust emission data were used to estimate core masses and the line widths were used to estimate non-thermal velocity dispersions. The estimated core masses are in poor agreement between surveys. For practical purposes we used core measurements by Motte et al. (1998) as these cores have the largest number of measured line widths.

As there are only twenty cores with a measured mass size and velocity dispersion, we used the data to calibrate a multivariate lognormal distribution. From this we drew one hundred correlated masses, sizes and velocity dispersions. We used these as initial conditions for SPH simulations.

9.2 Intrinsic core shapes

In Chapter 3 we addressed the inverse problem of inferring intrinsic core shapes from their projected aspect ratios. We assumes that the intrinsic shape of a prestellar core is approximately ellipsoidal. We proposed four models which define different families of ellipsoidal shapes. These all have free parameters which we fit to observations of core aspect ratios.

The simplest model has a single parameter $\tau_{\rm o}$. For each model core, we fixed one of the ellipsoid's semi-axes to one. The other two semi-axes were drawn from a lognormal distribution centred on one with standard deviation $\tau_{\rm o}$. We introduced more complex models with extra parameters which define preferences towards approximate oblate or prolate shapes and specific triaxial shapes.

We used Markov chain Monte Carlo methods to find the best fitting model parameters and compare model performance using Bayes factors. We found that:

- The single parameter model fits the observations with $\tau_{\rm o} \approx 0.6$.
- Bayes factors suggest that the single parameter model is the best choice. Other models risk over fitting the data with an excessive number of free parameters.

We randomly selected shapes from the single parameter model and scaled them by the sizes sampled in Chapter 2. These provided the intrinsic shapes of the initial conditions.

9.3 Internal structure

In Chapter 4 we discussed and justified our assumptions on the internal structure of prestellar cores. We assumed that the core density profile is that same as that of a critical Bonnor-Ebert sphere. While the cores in this thesis are not in hydrostatic equilibrium, this profile provides a reasonable approximation to core observations.

We gave each core a turbulent velocity field. The largest size velocity modes were modified to reproduce ordered rotation and radial excursions. We adopted the conventional power spectrum of $P \propto k^{-2}$ which left the ratio of compressive to solenoidal modes as the single free parameter. We produced velocity fields with purely compressive modes, purely solenoidal modes and the standard thermal mixture 2:1 solenoidal to compressive modes.

9.4 Results

In Chapter 8 we presented the results of SPH simulations of one hundred cores. Of these, sixty were prestellar. We repeated these simulations with no radiative feedback from protostellar accretion, episodic feedback (see Chapter 6, Section 6.2) and continuous feedback. Our main results are from cores which have 2:1 solenoidal to compressive velocity modes. We found that:

- Simulations with episodic feedback reproduced many features of the IMF, including position of the peak and the ratio of stars to brown dwarfs. In contrast, simulations continuous feedback failed to produce a significant number of brown dwarfs. It is difficult to justify why accretion would not heat the surrounding gas at all, so we conclude that episodic feedback is an important mechanism in star formation.

- While most YSOs formed from core collapse and disc fragmentation, in some cases, filamentary structure could form in elongated cores. These filaments could sometimes then fragment into multiple YSOs.

- The mass of a young stellar object (YSO) is not determined by the mass of the parent core. YSOs have the same average mass as a function of parent core mass. Higher mass cores produce more YSOs with a wider range of masses.

- The simulations reproduced many of the observed binary statistics of field stars. Roughly half the YSOs are were multiple systems and multiplicity frequency increased with YSO mass. The systems also had a wide range of semimajor axes and a distribution of mass ratios very similar to that of observations.

- Half the multiple systems were hierarchical with $N \geq 3$. We presented a case study of a long-lived sextuple system. These systems can form in the gas envelope of a prestellar core, but are difficult to manufacture from N-body interactions. These are observed in the field and we propose that they form in predominantly in prestellar cores.

We presented preliminary results of core simulations with purely compressive and solenoidal velocity fields we ran fifty SPH simulations for each field with different modes of feedback. Of these fifty cores, roughly thirty were prestellar. We found that compressive velocity fields produce more filamentary structures than the other fields. There did not seem to be a strong difference between solenoidal fields and 2:1 fields. More simulations and analysis are required in order to draw quantitative conclusions on this subject.

9.4.1 Future work

There are at least three directions of future work that will improve and expand upon the results in this thesis: further analysis of results, the inclusion of additional physics in the simulations and separate, but related, follow up work. Here we present some ideas of future work which may be interesting.

Further analysis

- In this thesis we have presented the results of roughly four-hundred prestellar core simulations. For the most part, we have focussed on statistically analysing the results as a whole, e.g. mass functions, binary statistics, etc. It will be

interesting to shift focus to individual cores in order to answer the following questions:

  - What environmental conditions are required for filaments to form instead of discs?
  - How strongly correlated is the mass of a YSO with the jeans mass of its parent core?
  - How do the binary statistics of multiple systems vary with time?

- The investigation into the effects of different velocity fields needs the same level of analysis given to the main set of results before we can draw any firm conclusions. This will also require running more simulations to improve the number statistics of the results.

Additional numerics and physics

- A new formulation of SPH sink particles, NewSinks, has been proposed by Hubber et al. (2013). Whilst accreting, these sinks leech mass off of SPH particles at rate governed by analytic models. Compared to standard sinks, this has been shown to provide a greater level of convergence between different SPH resolutions and sink density criteria.

- The inclusion of magneto-hydrodyamics MHD into Seren has been proposed (Hubber et al., 2011) but is not yet complete. There are at present two flavours of MHD: ideal (e.g. Price and Monaghan, 2004), where magnetic field lines are strongly coupled to the gas and non-ideal (e.g. Hosking and Whitworth, 2004) where the field lines are weakly coupled to the gas. The inclusion of MHD is expected to decrease the degree of core fragmentation, however the initial configuration of the magnetic fields are very difficult to infer from observations.

- Most observations show that YSOs have bipolar jets, however these are not included in the simulations. Jets can be modelled by ejecting high velocity, low mass SPH particles out from the poles of the sink particle (e.g. Stamatellos et al., 2005). This should not affect the formation of a single YSO, as gas typically accretes onto the equator of the sink. However, it is unclear how this would affect the formation of multiple YSOs which potentially have misaligned axes of rotation.

Follow-up work

- The simulations presented produce very few YSOs with masses greater than $1\,M_\odot$ and none greater than $2\,M_\odot$. This is because the cores have relatively low masses; the most massive core is 4.5 M. As a follow-up to these simulations, We plan to study the evolution of prestellar cores which are not isolated, but embedded in a gas reservoir. This will partially model the molecular cloud environment of the core. The simplest approach to this will be to embed the core in an ellipsoidal envelope. This will have uniform density equal to that of the core boundary and a total mass equal to two or three core masses. The prediction is that more massive cores will accrete the envelope whereas it will disperse away from less massive cores.

- Inclusion of a surrounding gas reservoir and MHD may also reduce the rate at which core envelopes are depleted. In these simulations, most core envelopes are accreted on to YSOs within 2×10^5 yrs. According to observations, this process should be slower.

- Finally, it will be interesting to use the small N clusters produced in these simulations as building blocks for larger N-body cluster simulations. By randomly arranging these sub-clusters (modulo some assumptions on inter-core spacing), we should be able to observe how many multiples survive and how the binary statistics are altered.

References

Alves, J., Lombardi, M., and Lada, C. J.: 2007, *A&A* **462**, L17

Alves, J. F., Lada, C. J., and Lada, E. A.: 2001, *Nature* **409**, 159

Andersen, M., Meyer, M. R., Greissl, J., and Aversa, A.: 2008, *ApJ* **683**, L183

André, P., Belloche, A., Motte, F., and Peretto, N.: 2007, *A&A* **472**, 519

Andre, P., Ward-Thompson, D., and Barsony, M.: 1993, *ApJ* **406**, 122

Andre, P., Ward-Thompson, D., and Barsony, M.: 2000, *Protostars and Planets IV* p. 59

André, P., Ward-Thompson, D., and Greaves, J.: 2012, *Science* **337**, 69

Attwood, R.: 2008, *Ph.D. thesis*, University of Wales School of Physics and Astronomy

Balbus, S. A. and Hawley, J. F.: 1998, *Reviews of Modern Physics* **70**, 1

Ballesteros-Paredes, J., Klessen, R. S., Mac Low, M.-M., and Vazquez-Semadeni, E.: 2007, *Protostars and Planets V* pp 63–80

Bate, M. R.: 2009a, *MNRAS* **392**, 590

Bate, M. R.: 2009b, *MNRAS* **397**, 232

Bate, M. R.: 2009c, *MNRAS* **392**, 1363

Bate, M. R. and Bonnell, I. A.: 2005, *MNRAS* **356**, 1201

Bate, M. R., Bonnell, I. A., and Bromm, V.: 2002, *MNRAS* **332**, L65

Bate, M. R., Bonnell, I. A., and Price, N. M.: 1995, *MNRAS* **277**, 362

Bell, K. R. and Lin, D. N. C.: 1994, *ApJ* **427**, 987

Binney, J.: 1985, *MNRAS* **212**, 767

Bonnell, I. and Bastien, P.: 1992, *ApJ* **401**, L31

Bonnell, I. A. and Bate, M. R.: 2006, *MNRAS* **370**, 488

Bonnell, I. A., Bate, M. R., and Vine, S. G.: 2003, *MNRAS* **343**, 413

Bonnell, I. A., Vine, S. G., and Bate, M. R.: 2004, *MNRAS* **349**, 735

Bonnor, W. B.: 1956, *MNRAS* **116**, 351

Boss, A. P. and Bodenheimer, P.: 1979, *ApJ* **234**, 289

Burkert, A. and Bodenheimer, P.: 2000, *ApJ* **543**, 822

Calvet, N., Muzerolle, J., Briceño, C., Hernández, J., Hartmann, L., Saucedo, J. L., and Gordon, K. D.: 2004, *ApJ* **128**, 1294

Chabrier, G.: 2003, *ApJ* **586**, L133

Chabrier, G.: 2005, in E. Corbelli, F. Palla, and H. Zinnecker (eds.), *The Initial Mass Function 50 Years Later*, Vol. 327 of *Astrophysics and Space Science Library*, p. 41

Chandrasekhar, S.: 1939, *An introduction to the study of stellar structure*, The University of Chicago Press

Clark, P. C., Bonnell, I. A., and Klessen, R. S.: 2008, *MNRAS* **386**, 3

Dopita, A.: 1978, *ApJ* **63**, 237

Dubinski, J., Narayan, R., and Phillips, T. G.: 1995, *ApJ* **448**, 226

Duchêne, G. and Kraus, A.: 2013, *ArXiv e-prints*

Elmegreen, B. G.: 2000, *ApJ* **530**, 277

Enoch, M. L., Evans, II, N. J., Sargent, A. I., Glenn, J., Rosolowsky, E., and Myers, P.: 2008, *ApJ* **684**, 1240

Enoch, M. L., Young, K. E., Glenn, J., Evans, II, N. J., Golwala, S., Sargent, A. I., Harvey, P., Aguirre, J., Goldin, A., Haig, D., Huard, T. L., Lange, A., Laurent, G., Maloney, P., Mauskopf, P., Rossinot, P., and Sayers, J.: 2006, *ApJ* **638**, 293

Evans, II, N. J., Dunham, M. M., Jørgensen, J. K., Enoch, M. L., Merín, B., van Dishoeck, E. F., Alcalá, J. M., Myers, P. C., Stapelfeldt, K. R., Huard, T. L., Allen, L. E., Harvey, P. M., van Kempen, T., Blake, G. A., Koerner, D. W., Mundy, L. G., Padgett, D. L., and Sargent, A. I.: 2009, *A* **181**, 321

Fiege, J. D. and Pudritz, R. E.: 2000, *MNRAS* **311**, 85

Forgan, D. and Rice, K.: 2010, *MNRAS* **402**, 1349

Frigo, M. and Johnson, S. G.: 2005, *Proceedings of the IEEE* **93(2)**, 216, Special issue on "Program Generation, Optimization, and Platform Adaptation"

Gingold, R. A. and Monaghan, J. J.: 1977, *MNRAS* **181**, 375

Girichidis, P., Federrath, C., Allison, R., Banerjee, R., and Klessen, R. S.: 2012a, *MNRAS* **420**, 3264

Girichidis, P., Federrath, C., Banerjee, R., and Klessen, R. S.: 2012b, *MNRAS* **420**, 613

Goodman, A. A., Benson, P. J., Fuller, G. A., and Myers, P. C.: 1993, *ApJ* **406**, 528

Goodwin, S. P., Kroupa, P., Goodman, A., and Burkert, A.: 2007, *Protostars and Planets V* pp 133–147

Goodwin, S. P., Ward-Thompson, D., and Whitworth, A. P.: 2002, *MNRAS* **330**, 769

Goodwin, S. P. and Whitworth, A. P.: 2004, *A&A* **413**, 929

Goodwin, S. P., Whitworth, A. P., and Ward-Thompson, D.: 2004, *A&A* **423**, 169

Goodwin, S. P., Whitworth, A. P., and Ward-Thompson, D.: 2006, *A&A* **452**, 487

Green, J. D., Evans, II, N. J., Kóspál, Á., van Kempen, T. A., Herczeg, G., Quanz, S. P., Henning, T., Lee, J.-E., Dunham, M. M., Meeus, G., Bouwman, J., van Dishoeck, E., Chen, J.-H., Güdel, M., Skinner, S. L., Merello, M., Pooley, D., Rebull, L. M., and Guieu, S.: 2011, *ApJ* **731**, L25

Greene, T. P., Aspin, C., and Reipurth, B.: 2008, *ApJ* **135**, 1421

Hachisu, I., Tohline, J. E., and Eriguchi, Y.: 1987, *ApJ* **323**, 592

Hartmann, L. and Kenyon, S. J.: 1985, *ApJ* **299**, 462

Hartmann, L. and Kenyon, S. J.: 1996, *ARA&A* **34**, 207

Harvey, D. W. A., Wilner, D. J., Lada, C. J., Myers, P. C., Alves, J. F., and Chen, H.: 2001, *ApJ* **563**, 903

Herbig, G. H.: 1977, *ApJ* **217**, 693

Hildebrand, R. H.: 1983, *JQRAS* **24**, 267

Hosking, J. G. and Whitworth, A. P.: 2004, *MNRAS* **347**, 994

Hubber, D. A., Batty, C. P., McLeod, A., and Whitworth, A. P.: 2011, *A&A* **529**, A27

Hubber, D. A., Walch, S., and Whitworth, A. P.: 2013, *MNRAS* **430**, 3261

Isella, A., Carpenter, J. M., and Sargent, A. I.: 2009, *ApJ* **701**, 260

Janson, M., Hormuth, F., Bergfors, C., Brandner, W., Hippler, S., Daemgen, S., Kudryavtseva, N., Schmalzl, E., Schnupp, C., and Henning, T.: 2012, *ApJ* **754**, 44

Jeffreys, H.: 1961, *The Theory of Probability*, p. 432, Clarendon Press, Oxford, third edition

Johnstone, D. and Bally, J.: 2006, *ApJ* **653**, 383

Johnstone, D., Fich, M., Mitchell, G. F., and Moriarty-Schieven, G.: 2001, *ApJ* **559**, 307

Johnstone, D., Wilson, C. D., Moriarty-Schieven, G., Joncas, G., Smith, G., Gregersen, E., and Fich, M.: 2000, *ApJ* **545**, 327

Jones, C. E. and Basu, S.: 2002, *ApJ* **569**, 280

Jones, C. E., Basu, S., and Dubinski, J.: 2001, *ApJ* **551**, 387

Joos, M., Hennebelle, P., and Ciardi, A.: 2012, *A&A* **543**, A128

Kenyon, S. J. and Hartmann, L.: 1995, *ApJ* **101**, 117

Keto, E., Broderick, A. E., Lada, C. J., and Narayan, R.: 2006, *ApJ* **652**, 1366

Kiguchi, M., Narita, S., Miyama, S. M., and Hayashi, C.: 1987, *ApJ* **317**, 830

King, A. R., Pringle, J. E., and Livio, M.: 2007, *MNRAS* **376**, 1740

King, R. R., Goodwin, S. P., Parker, R. J., and Patience, J.: 2012a, *MNRAS* **427**, 2636

King, R. R., Parker, R. J., Patience, J., and Goodwin, S. P.: 2012b, *MNRAS* **421**, 2025

Kirk, J. M., Ward-Thompson, D., Palmeirim, P., André, P., Griffin, M. J., Hargrave, P. J., Könyves, V., Bernard, J.-P., Nutter, D. J., Sibthorpe, B., Di Francesco, J., Abergel, A., Arzoumanian, D., Benedettini, M., Bontemps, S., Elia, D., Hennemann, M., Hill, T., Men'shchikov, A., Motte, F., Nguyen-Luong, Q., Peretto, N., Pezzuto, S., Rygl, K. L. J., Sadavoy, S. I., Schisano, E., Schneider, N., Testi, L., and White, G.: 2013, *MNRAS* **432**, 1424

Könyves, V., André, P., Men'shchikov, A., Schneider, N., Arzoumanian, D., Bontemps, S., Attard, M., Motte, F., Didelon, P., Maury, A., Abergel, A., Ali, B., Baluteau, J.-P., Bernard, J.-P., Cambrésy, L., Cox, P., di Francesco, J., di Giorgio, A. M., Griffin, M. J., Hargrave, P., Huang, M., Kirk, J., Li, J. Z., Martin, P., Minier, V., Molinari, S., Olofsson, G., Pezzuto, S., Russeil, D., Roussel, H., Saraceno, P., Sauvage, M., Sibthorpe, B., Spinoglio, L., Testi, L., Ward-Thompson, D., White, G., Wilson, C. D., Woodcraft, A., and Zavagno, A.: 2010, *A&A* **518**, L106

Kouwenhoven, M. B. N., Goodwin, S. P., Parker, R. J., Davies, M. B., Malmberg, D., and Kroupa, P.: 2010, *MNRAS* **404**, 1835

Kraus, A. L., Ireland, M. J., Martinache, F., and Hillenbrand, L. A.: 2011, *ApJ* **731**, 8

Kroupa, P.: 1995a, *MNRAS* **277**, 1491

Kroupa, P.: 1995b, *MNRAS* **277**, 1507

Kroupa, P.: 2001, *MNRAS* **322**, 231

Krumholz, M. R.: 2006, *ApJ* **641**, L45

Krumholz, M. R., Cunningham, A. J., Klein, R. I., and McKee, C. F.: 2010, *ApJ* **713**, 1120

Lada, C. J.: 1987, in M. Peimbert and J. Jugaku (eds.), *Star Forming Regions*, Vol. 115 of *IAU Symposium*, pp 1–17

Lada, C. J.: 1999, in C. J. Lada and N. D. Kylafis (eds.), *NATO ASIC Proc. 540: The Origin of Stars and Planetary Systems*, p. 143

Lada, C. J., Muench, A. A., Rathborne, J., Alves, J. F., and Lombardi, M.: 2008, *ApJ* **672**, 410

Larson, R. B.: 1969, *MNRAS* **145**, 271

Larson, R. B.: 1981, *MNRAS* **194**, 809

Leinert, C., Zinnecker, H., Weitzel, N., Christou, J., Ridgway, S. T., Jameson, R., Haas, M., and Lenzen, R.: 1993, *A&A* **278**, 129

Lin, C. C., Mestel, L., and Shu, F. H.: 1965, *ApJ* **142**, 1431

Lucy, L. B.: 1977, *ApJ* **82**, 1013

Machida, M. N., Inutsuka, S.-i., and Matsumoto, T.: 2011, *ApJ* **729**, 42

Machida, M. N., Matsumoto, T., Hanawa, T., and Tomisaka, K.: 2005, *MNRAS* **362**, 382

Mamajek, E. E.: 2008, *Astronomische Nachrichten* **329**, 10

Martin, R. G. and Lubow, S. H.: 2011, *ApJ* **740**, L6

Martin, R. G., Lubow, S. H., Livio, M., and Pringle, J. E.: 2012a, *MNRAS* **420**, 3139

Martin, R. G., Lubow, S. H., Livio, M., and Pringle, J. E.: 2012b, *MNRAS* **423**, 2718

Masunaga, H. and Inutsuka, S.-i.: 2000, *ApJ* **531**, 350

Mohanty, S., Jayawardhana, R., and Basri, G.: 2005, *ApJ* **626**, 498

Monaghan, J. J.: 1997, *Journal of Computational Physics* **136**, 298

Monaghan, J. J.: 2002, *MNRAS* **335**, 843

Monaghan, J. J. and Lattanzio, J. C.: 1985, *A&A* **149**, 135

Morris, J. P. and Monaghan, J. J.: 1997, *Journal of Computational Physics* **136**, 41

Motte, F., Andre, P., and Neri, R.: 1998, *A&A* **336**, 150

Motte, F., André, P., Ward-Thompson, D., and Bontemps, S.: 2001, *A&A* **372**, L41

Mouschovias, T. C.: 1976, *ApJ* **207**, 141

Muzerolle, J., Luhman, K. L., Briceño, C., Hartmann, L., and Calvet, N.: 2005, *ApJ* **625**, 906

Myers, P. C., Fuller, G. A., Goodman, A. A., and Benson, P. J.: 1991, *ApJ* **376**, 561

Natta, A., Testi, L., Muzerolle, J., Randich, S., Comerón, F., and Persi, P.: 2004, *A&A* **424**, 603

Nelson, R. P. and Papaloizou, J. C. B.: 1994, *MNRAS* **270**, 1

Nutter, D. and Ward-Thompson, D.: 2007, *MNRAS* **374**, 1413

Offner, S. S. R., Klein, R. I., McKee, C. F., and Krumholz, M. R.: 2009, *ApJ* **703**, 131

Offner, S. S. R., Kratter, K. M., Matzner, C. D., Krumholz, M. R., and Klein, R. I.: 2010, *ApJ* **725**, 1485

Padgett, D. L., Brandner, W., Stapelfeldt, K. R., Strom, S. E., Terebey, S., and Koerner, D.: 1999, *ApJ* **117**, 1490

Palla, F. and Stahler, S. W.: 1993, *ApJ* **418**, 414

Parker, R. J. and Goodwin, S. P.: 2011, *MNRAS* **411**, 891

Parker, R. J. and Goodwin, S. P.: 2012, *MNRAS* **424**, 272

Parker, R. J., Goodwin, S. P., Kroupa, P., and Kouwenhoven, M. B. N.: 2009, *MNRAS* **397**, 1577

Parker, R. J. and Reggiani, M. M.: 2013, *ArXiv e-prints*

Peneva, S. P., Semkov, E. H., Munari, U., and Birkle, K.: 2010, *A&A* **515**, A24

Price, D. J.: 2007, *PASA* **24**, 159

Price, D. J. and Monaghan, J. J.: 2004, *MNRAS* **348**, 139

Price, D. J. and Monaghan, J. J.: 2007, *MNRAS* **374**, 1347

Raghavan, D., McAlister, H. A., Henry, T. J., Latham, D. W., Marcy, G. W., Mason, B. D., Gies, D. R., White, R. J., and ten Brummelaar, T. A.: 2010, *ApJ* **190**, 1

Rathborne, J. M., Lada, C. J., Muench, A. A., Alves, J. F., Kainulainen, J., and Lombardi, M.: 2009, *ApJ* **699**, 742

Ratzka, T., Köhler, R., and Leinert, C.: 2005, *A&A* **437**, 611

Reggiani, M. M. and Meyer, M. R.: 2011, *ApJ* **738**, 60

Reipurth, B.: 1989, *Nature* **340**, 42

Reipurth, B. and Clarke, C.: 2001, *ApJ* **122**, 432

Reipurth, B. and Zinnecker, H.: 1993, *A&A* **278**, 81

Rosswog, S., Davies, M. B., Thielemann, F.-K., and Piran, T.: 2000, *A&A* **360**, 171

Ryden, B. S.: 1996, *ApJ* **471**, 822

Salpeter, E. E.: 1955, *ApJ* **121**, 161

Scholz, A., Froebrich, D., and Wood, K.: 2013, *MNRAS* **430**, 2910

Silverman, B.: 1998, *Density Estimation for Statistics and Data Analysis*, p. 48, London: Chapman & Hall/CRC.

Simpson, R. J., Johnstone, D., Nutter, D., Ward-Thompson, D., and Whitworth, A. P.: 2011, *MNRAS* **417**, 216

Simpson, R. J., Nutter, D., and Ward-Thompson, D.: 2008, *MNRAS* **391**, 205

Springel, V., Yoshida, N., and White, S. D. M.: 2001, *NewA* **6**, 79

Stamatellos, D. and Whitworth, A. P.: 2008, *A&A* **480**, 879

Stamatellos, D., Whitworth, A. P., Bisbas, T., and Goodwin, S.: 2007a, *A&A* **475**, 37

Stamatellos, D., Whitworth, A. P., Boyd, D. F. A., and Goodwin, S. P.: 2005, *A&A* **439**, 159

Stamatellos, D., Whitworth, A. P., and Hubber, D. A.: 2011, *ApJ* **730**, 32

Stamatellos, D., Whitworth, A. P., and Hubber, D. A.: 2012, *MNRAS* **427**, 1182

Stamatellos, D., Whitworth, A. P., and Ward-Thompson, D.: 2007b, *MNRAS* **379**, 1390

Stamatellos, D., Whitworth, A. P., and Ward-Thompson, D.: 2007c, *MNRAS* **379**, 1390

Stanke, T., Smith, M. D., Gredel, R., and Khanzadyan, T.: 2006, *A&A* **447**, 609

Stutzki, J. and Guesten, R.: 1990, *ApJ* **356**, 513

Tassis, K.: 2007, *MNRAS* **379**, L50

Testi, L. and Sargent, A. I.: 1998, *ApJ* **508**, L91

Tilanus, R. P. J., Jenness, T., Economou, F., and Cockayne, S.: 1997, in G. Hunt and H. Payne (eds.), *Astronomical Data Analysis Software and Systems VI*, Vol. 125 of *Astronomical Society of the Pacific Conference Series*, p. 397

Tokovinin, A.: 2008, *MNRAS* **389**, 925

Tomisaka, K.: 1991, *ApJ* **376**, 190

Toomre, A.: 1964, *ApJ* **139**, 1217

Urban, A., Martel, H., and Evans, II, N. J.: 2010, *ApJ* **710**, 1343

Vorobyov, E. I. and Basu, S.: 2005, *ApJ* **633**, L137

Walch, S., Burkert, A., Whitworth, A., Naab, T., and Gritschneder, M.: 2009, *MNRAS* **400**, 13

Walch, S., Whitworth, A. P., and Girichidis, P.: 2012, *MNRAS* **419**, 760

Weinberg, M. D.: 2009, *Computing the Bayesian Factor from a Markov chain Monte Carlo Simulation of the Posterior Distribution, arXiv:0911.1777*

Whitworth, A. P. and Stamatellos, D.: 2006, *A&A* **458**, 817

Wilking, B. A. and Lada, C. J.: 1983, *ApJ* **274**, 698

Wilkins, D. R. and Clarke, C. J.: 2012, *MNRAS* **419**, 3368

Williams, J. P., de Geus, E. J., and Blitz, L.: 1994, *ApJ* **428**, 693

Young, M. D., Bertram, E., Moeckel, N., and Clarke, C. J.: 2012, *MNRAS* **426**, 1061

Zhu, Z., Hartmann, L., Calvet, N., Hernandez, J., Muzerolle, J., and Tannirkulam, A.-K.: 2007, *ApJ* **669**, 483

Zhu, Z., Hartmann, L., and Gammie, C.: 2009a, *ApJ* **694**, 1045

Zhu, Z., Hartmann, L., and Gammie, C.: 2010a, *ApJ* **713**, 1143

Zhu, Z., Hartmann, L., Gammie, C., and McKinney, J. C.: 2009b, *ApJ* **701**, 620

Zhu, Z., Hartmann, L., Gammie, C. F., Book, L. G., Simon, J. B., and Engelhard, E.: 2010b, *ApJ* **713**, 1134

Zinnecker, H., Krabbe, A., McCaughrean, M. J., Stanke, T., Stecklum, B., Brandner, W., Padgett, D. L., Stapelfeldt, K. R., and Yorke, H. W.: 1999, *A&A* **352**, L73